UNIVERSITÀ DELLA CALABRIA

UNIVERSITÀ DELLA CALABRIA
Dipartimento di Fisica

Scuola di Dottorato
Scienza e Tecnica "Bernardino Telesio"

Indirizzo
Fisica dei Sistemi Complessi

XXVI CICLO

Cancellation analysis in turbulent plasmas: from numerical simulations to solar active regions

Settore Scientifico Disciplinare FIS/05

Direttore: Prof. Roberto Bartolino

Supervisore: Dr. Luca Sorriso-Valvo

Dottorando: Dr. Gaetano De Vita
Gaetano De V.

Contents

1 Turbulence and intermittency in plasmas 19
  1.1 Basic description of plasma dynamics 19
    1.1.1 The different descriptions of plasmas 19
    1.1.2 The kinetic description 21
    1.1.3 The magnetohydrodynamic description 22
    1.1.4 The incompressible case, and the Elsässer variables . . 25
  1.2 Scaling laws and turbulence 26
    1.2.1 The Reynolds number 26
    1.2.2 The turbulent cascade 27
  1.3 Phenomenology of turbulence 29
    1.3.1 The Kolmogorov spectrum 29
    1.3.2 The Kraichnan spectrum 30
    1.3.3 Self-similarity 31
  1.4 Intermittency 32

2 Cancellation analysis and structures 35
  2.1 Introduction 35
  2.2 The signed measure and the cancellation exponent 36
  2.3 Cancellation exponents and fractal dimensions 37

3 Hall-magnetohydrodynamic 39
  3.1 Three-dimensional Hall-MHD 39
    3.1.1 Introduction 39
    3.1.2 Reduced MHD and HMHD models 42
    3.1.3 Numerical simulations 44
    3.1.4 Results 50
  3.2 Conclusions 59

4 Vlasov-Maxwell system **61**
- 4.1 Two-dimensional hybrid Vlasov-Maxwell system 61
  - 4.1.1 Equations and numerical simulation 61
  - 4.1.2 Cancellation analysis 62
  - 4.1.3 Conclusions 78

5 Solar observations **81**
- 5.1 Introduction: photospheric active regions 81
- 5.2 Ground based solar observations: NOAA 10019 82
  - 5.2.1 Observation 82
  - 5.2.2 Time evolution and flaring activity 85
- 5.3 Space based solar observations: NOAA 11158 89
  - 5.3.1 Observation 89
  - 5.3.2 Data processing and cancellation analysis 91
  - 5.3.3 Test on the quality of the analysis 101
- 5.4 Conclusions 106

List of Figures

1 Schematic representation of *Two ribbon flare model*. Adapted from [10]. 16

1.1 A schematic picture of the Richardson cascade. The hierarchy of structures represents the non-linear transfer of energy between different scales. [31] 28

3.1 Left panels: slices of the perpendicular current component j_x (in adimensional units) in the perpendicular plane, for the $\varepsilon = 0$ and $\varepsilon = 1/32$ and used in this work (ε increasing from top to bottom). Right panels: the same fields, seen at an arbitrary tilt angle, highlighting the presence of alternate sign structures at all scales. In these panels, the scale of grays is arbitrary. 45

3.2 Left panels: slices of the perpendicular current component j_x (in adimensional units) in the perpendicular plane, for the $\varepsilon = 1/16$ and $\varepsilon = 1/8$ and used in this work (ε increasing from top to bottom). Right panels: the same fields, seen at an arbitrary tilt angle, highlighting the presence of alternate sign structures at all scales. In these panels, the scale of grays is arbitrary. 46

3.3 Left panels: slices of the perpendicular current component j_z (in adimensional units) in the perpendicular plane, for the $\varepsilon = 0$ and $\varepsilon = 1/32$ and used in this work (ε increasing from top to bottom). Right panels: the same fields, seen at an arbitrary tilt angle, highlighting the presence of alternate sign structures at all scales. In these panels, the scale of grays is arbitrary. 47

3.4 Left panels: slices of the perpendicular current component j_z (in adimensional units) in the perpendicular plane, for the $\varepsilon = 1/16$ and $\varepsilon = 1/8$ and used in this work (ε increasing from top to bottom). Right panels: the same fields, seen at an arbitrary tilt angle, highlighting the presence of alternate sign structures at all scales. In these panels, the scale of grays is arbitrary. 48

3.5 The total energy spectra for the four Runs (see legend). The vertical lines represents the values of the inverse ion skin depth for the three Runs with nonvanishing Hall term. Phenomenological predictions for the MHD range and for the Hall range are also indicated. 49

3.6 The signed measure μ as estimated for j_x in the plane y-z, shown for Run 3 ($\varepsilon = 1/16$), for four different partition box sizes (top-left: $l_\perp = 0.12$; top-right:$l_\perp = 0.04$; bottom-left: $l_\perp = 0.016$; bottom-rigth: $l_\perp = 0.002$. 51

3.7 The partition function $\chi(l_\perp)$ versus the scale parameter $l_\perp$. The examples given here refer to the current perpendicular component j_x (left panel) and parallel component j_z (right panel), for $\varepsilon = 1/16$. 52

3.8 The partition function $\chi(l_\perp)$ for the current perpendicular component j_x (left panel) and parallel component j_z (right panel), for the four values of the Hall parameter ε (see legend), at $l_\parallel/2\pi = 0.03$. The curves have been arbitrarily shifted for clarity. 52

3.9 Examples of fit of the partition function, shown here at $\varepsilon = 0$ for j_z (left panel) and at $\varepsilon = 1/8$ for j_x (right panel). The power law fits $\chi(l_\perp) = A(l_\perp/2\pi)^{-\kappa}$ are superimposed (one in the left panel, two in the right panel). The ion skin depth is indicated as dashed line in the right panel. The bottom part of both right plot shows the compensated partition functions $\chi(l_\perp)/A(l_\perp/2\pi)^{-\kappa}$. 53

3.10 The fractal dimension $D_\perp$ estimated through equation 2.4, for the three components of current (a for the MHD range, c for the Hall range) and vorticity (b for the MHD range, d for the Hall range), labeled with different colors and line style (see inset). The indicators $D^\star_\perp$ (see text) are also plotted for the two fields (panels e and f, black lines). 55

3.11 The partition function $\chi(l_\parallel)$, for j_x at $\varepsilon = 1/16$, and for $l_\perp/2\pi = 0.002$. A power law fit is superimposed. The bottom part of the plot shows the compensated partition function $\chi(l_\parallel)/A(l_\parallel/2\pi)^{-\kappa}$. 57
3.12 The fractal dimension D of the parallel partition function, for the three components of current (left panels) and vorticity (right panels). The overall indicators $D^\star_\parallel$ are also plotted for the two fields (bottom panels). 58

4.1 The total energy spectrum of the Vlasov-Maxwell numerical simulation for one snapshot at $t = 50\Omega_{ci}^{-1}$. The Kolmogorov expectation $k^{-5/3}$ (gray dot-dashed) is reported as a reference, while the vertical dashed line represents the ion skin depth wave number. 63
4.2 Left panels: perpendicular current component j_x in the perpendicular plane x-y, for the snapshots and for $\beta = 0.25$ (top), $\beta = 0.50$ (bottom). Right panels: parallel current component j_z in the perpendicular plane x-y. 64
4.3 Left panels: perpendicular current component j_x in the perpendicular plane x-y, for the snapshots and for $\beta = 1.00$ (top), $\beta = 1.50$ (bottom). Right panels: parallel current component j_z in the perpendicular plane x-y. 65
4.4 Left panels: perpendicular current component j_x in the perpendicular plane x-y, for the snapshots and for $\beta = 2.00$ (top), $\beta = 5.00$ (bottom). Right panels: parallel current component j_z in the perpendicular plane x-y. 66
4.5 The signed measure μ as estimated for j_z in the plane x-y, for Run 1 ($\beta = 0.25$ at $t = 10\Omega_{ci}^{-1}$), for four different partition box sizes (from top to bottom, $l/\rho_{ii} = 0.039$, 0.312, 0.820 and 2.461). The color scale is arbitrary. 67
4.6 The signed measure μ as estimated for j_z in the plane x-y, for Run 1 ($\beta = 0.25$ at $t = 50\Omega_{ci}^{-1}$), for four different partition box sizes (from top to bottom, $l/\rho_{ii} = 0.039$, 0.312, 0.820 and 2.461). The color scale is arbitrary. 68
4.7 The signed measure μ as estimated for j_z in the plane x-y, for Run 6 ($\beta = 5.00$ at $t = 10\Omega_{ci}^{-1}$), for four different partition box sizes (from top to bottom, $l/\rho_{ii} = 0.039$, 0.312, 0.820 and 2.461). The color scale is arbitrary. 69

4.8 The signed measure μ as estimated for j_z in the plane x-y, for Run 6 ($\beta = 5.00$ at $t = 50\Omega_{ci}^{-1}$), for four different partition box sizes (from top to bottom, $l/\rho_{ii} = 0.039$, 0.312, 0.820 and 2.461). The color scale is arbitrary. 70

4.9 The partition function $\chi(l)$ vs. l/ρ_{ii} for component j_x of the current density for Run 1 (left panel) Run 5 (right panel), for 3 different time (see each Figure). Power law fits are superimposed. The ion skin depth is indicated (dashed line). The bottom part of each plot shows the compensated partition function $\chi(l)/A(l/\rho_{ii})^{-\kappa}$. 72

4.10 The partition function $\chi(l)$ vs. l/ρ_{ii} for component j_z of the current density for Run 1 (left panel) Run 5 (right panel), for 3 different time (see each Figure). Power law fits are superimposed. The ion skin depth is indicated (dashed line). The bottom part of each plot shows the compensated partition function $\chi(l)/A(l/\rho_{ii})^{-\kappa}$. 73

4.11 Cancellation exponent of component j_x (left panels) and components j_z (right panels) of current density *vs* time for Run 1, 2 and 3 (from top to bottom). The red circles are the cancellation exponents compute for small scales while blue diamonds compute for large scale. In green the level of turbulent activity is represented by the average out-of-plane squared current density $\langle j_z^2 \rangle$. 75

4.12 Cancellation exponent of component j_x (left panels) and components j_z (right panels) of current density *vs* time for Run 4, 5 and 6 (from top to bottom). The red circles are the cancellation exponents compute for small scales while blue diamonds compute for large scale. In green the level of turbulent activity is represented by the average out-of-plane squared current density $\langle j_z^2 \rangle$. 76

4.13 Cancellation exponent of component j_x (left panels) and components j_z (right panels) of current density *vs* beta of plasma for five time. 77

5.1 Maps of vertical magnetic field B_z for the AR 10019 as measured on 3 July (a) 4 July (b), 5 July (c), and 6 July (d) 2002. Time of each snapshot is indicated in the legend. Dot-dashed boxes indicate the box $Q_{max}(L_{max})$ of size L_{max} and the thin-line the box $Q(L)$ of size L (see text for explaination). 83

5.2 Maps of vertical component of the current density J_z for the AR 10019 as measured on 3 July (a) 4 July (b), 5 July (c), and 6 July (d) 2002. Time of each snapshot is indicated in the legend. Dot-dashed boxes indicate the box $Q_{max}(L_{max})$ of size L_{max} and the thin-line the box $Q(L)$ of size L (see text for explaination). 84

5.3 Fractal dimension of the photosperic current density structures D *versus* time. (symbols connected by solid line, left vertical axis). The vertical lines show the X-ray class of flares (right vertical axis). 86

5.4 Left panel: the partition functions $log\ \chi(l)\ vs\ log\ (l/L)$ for the current density j_z calculated for unsmoothed (1×1, circles) and smoothed (3×3, diamonds, and 5×5, triangles). This example refers to the snapshot taken on 3 July 2002 at 17:20 UT. Right panel: cancellation exponents κ for the three cases shown in left panel. 87

5.5 Fractal dimension *versus* time for the three datasets, obtained using the unsmoothed data (1×1) and the two synthetic datasets with smoothing (see legend). The vertical lines show the X-ray class of flares (right vertical axis). 88

5.6 The current helicity hc_z determined for the active region NOAA 11158 on 2011-February-15 01:36 UT. The presence of positive and negative structures on all scales is cleary visible. 90

5.7 Maps of vertical magnetic fields B_z for 3 times (see the panels). Dashed-line boxes indicate the area $Q_{max}(L_{max}) = 150 \times 120$ pixels (corresponding a 75×60 *arcsec* on the solar photosphere) where, for $N = 10$ position of box $Q(L) = 120 \times 120$ (thin-line), the calculations were done. The choice of the area $Q_{max}(L_{max})$ was made according on the location of the flare X-class (small dotted-dashed boxes b). In the panel a the AR is in the phase of birth, while in panels $b - c$ the AR is more structured: panel b is taken at the start time of the flare $X2.2$, and c was taken while the AR was approaching the solar limb. 92

5.8 Left panels show the maps of vertical current density j_z for the AR 11158 for 3 times (see the panels). Right top panels show the averaged partition function and the power law fits $\chi(l) = A(l/L)^{-\kappa}$ are superimposed. Finally, the bottom part of each right plot shows the compensated partition function $\chi(l)/A(l/L)^{-\kappa}$. 93

5.9 Left panels show the maps of vertical current density hc_z for the AR 11158 for 3 times (see the panels). Right top panels show the averaged partition function and the power law fits $\chi(l) = A(l/L)^{-\kappa}$ are superimposed. Finally, the bottom part of each plot right shows the compensated partition function $\chi(l)/A(l/L)^{-\kappa}$. 94

5.10 The Extreme-UV emission (SDO-AIA 131$\mathring{A}$ channel) integrated over AR 11158. 96

5.11 Top and bottom panels show the cancellation exponent for the current densisty and helicity respectively as a function of time exspressed in days (red line). The Extreme-UV emission (blue dashed-line) is superimposed. 97

5.12 Magnetic fluxes computed for the whole active region. The red line is the positive magnetic flux and the black dashed line is the module of negative magnetic flux. 98

5.13 Left paneles: Correlation coefficients ρ_P and ρ_S *vs* time lags using *Pearson* (top) and *Spearman* (bottom) definitions. The right panels show the scatter-plot of cancellation exponents for hc_z shifted by the maximum correlation time-lags *vs* Extreme-UV emission. In each scatter plot, the correlation coefficient is indicated. 100

5.14 The top panel shows the Magnetic field B_z. The boxes labeled with A, B and C delimit the area where the signed measure is computed. The bottom panel shows the cancellation exponentd κ computed for the three boxes *vs* time. The extreme ultra-violet (EUV) radiation is superposed (grey line). The three larger flares are also indicated 102

5.15 Correlation exponent (labeled ρ_S) *vs* time-lags using *Spearman* for the signal $\kappa_A(t)$ left panel and $\kappa_B(t)$ right panel and extreme ultra-violet (EUV) radiation. The cancelaltion exponents refer to for the current helicity. 103

5.16 Spearman correlation between cancellation exponent $\kappa_C(t)$ and EUV emission (see Fig. 5.14) calculated for the whole temporal series shown in the left panel, and for interval between $13 \leq time \leq 17$, shown in the right panel. 104
5.17 Spearman correlation of positive and negative magnetic flux and extreme ultra-violet, left and right panel respectively. . . . 105

Abstract

In questa tesi abbiamo studiato le caratteristiche di singolarità in segno delle strutture magnetiche generate in sistemi turbolenti, tramite l'analisi delle cancellazioni delle fluttuazioni. Tale analisi è stata applicata a dati sintetici ottenuti tramite diverse simulazioni numeriche (Hall MHD e Vlasov-Maxwell), e ad osservazioni di campi magnetici solari in regioni attive, sia da terra (THEMIS telescope) che dallo spazio (HMI-SDO). Oltre a caratterizzare le singolarità in segno, e quindi la topologia delle strutture turbolente, l'analisi delle cancellazioni ha permesso di ottenere importanti informazioni sui processi fisici osservati.

L'analisi di simulazioni numeriche 3d delle equazioni della Reduced Hall-MHD ha mostrato la presenza di due distinti ranges (MHD e Hall MHD), corrispondente ai diversi meccanismi di cascata turbolenta nei due regimi. Inoltre, nel range MHD le strutture di corrente sono poco sensibili all'effetto Hall, mentre le strutture di vorticità mostrano una più evidente frammentazione. Nel range Hall, invece, la corrente e la vorticità manifestano un comportamento simile dovuto alla presenza di strutture più frammentate.

L'applicazione dell'analisi delle cancellazioni ad un set di simulazioni numeriche di un sistema 2d-Vlasov-Maxwell ha sottolineato, di nuovo, la presenza di due differenti regimi (fluido e cinetico). L'evoluzione temporale dell'esponente di cancellazione ha permsso l'osservazione quantitativa della transizione alla turbolenza.

Dopo aver mostrato l'efficacia dell'analisi delle cancellazioni tramite lo studio di simulazioni numeriche, la tecnica è stata applicata a misure sperimentali di regioni attive solari. Il vettore campo magnetico misurato dal telescopio terrestre THEMIS per la regione attiva NOAA 10019 ha mostrato la presenza di filamenti frammentati di corrente. Inoltre, la variazione della dimensione frattale delle strutture di corrente, ed in particolare il loro smussamento, è stato discusso in relazione alla presenza di flares.

Infine, abbiamo applicato la tecnica di analisi a misure di campo magnetico solare dallo spazio (HMI-SDO), per la regione attiva NOAA 11158. La variazione temporale dell'esponente di cancellazione ha mostrato correlazione significativa con l'emissione EUV, legata alla produzione di flares. In particolare, abbiamo osservato che la complessità del campo magnetico subisce variazioni significative con un anticipo di 1 ora rispetto alla produzione di flares.

Introduction

Many of the astrophysical processes observed today are characterized by complex dynamics. In such phenomena non-linearity, turbulence and intermittency dominate the statistical behaviour of the observables. This behavior is generally linked to the presence of coherent structures, which play a relevant role in several astrophysical phenomena [1, 2, 3].

Structures in turbulent gases or plasmas are often present on a wide range of scales, and may be the site of dissipative phenomena, generation of waves or other instabilities. In astrophysical turbulent plasmas such as the solar wind, structures as sheets, spirals and filaments have been observed [38, 39, 40]. Direct numerical simulations [32, 33, 34, 35, 36, 37, 61] have also provided evidence of formation of a hierarchy of structures, whose characteristics depend on the model and regime.

One notable example of evident generation of magnetic structures is the complex dynamics of solar active regions. These are regions of emergence of magnetic flux from the solar interiors to the solar surface. More in particular, the solar dynamo magnetic fields interact with the plasma motions in the convective zone. Here, the magnetic field is accumulated in particular regions of space because of the turbulent convective motions, like passive scalars do in turbulent flows. The field accumulation leads to floating instability, which makes the strong magnetic field flux tubes emerge in the photosphere. The emerging magnetic field is often visible as sunspot on the solar photosphere [4]. These zones are characterized by magnetic field fluctuations on a wide range of time and space scales, and formation of fine, filamentary structures. Active regions hosts the majority of the solar flares.

Solar flares are explosive phenomena that occur suddenly and with a release of huge amounts of energy [107]. Magnetic energy is dissipated at numerous tangential discontinuities which arise spontaneously in the magnetic field within solar active regions. This energy is released in various forms such as thermal and kinetic energy, as well as energetic particles. Solar flares models are mostly based on magnetic reconnection of the dynamic coronal loops emerging in the solar active regions [106, 108]. The way reconnection is related to changes in the magnetic field configuration and fine structure within ARs, is still an open question [105]. Figure 1 shows schematically one of the many flare models, called *Two ribbon flare model* [6, 7, 8, 9]. In this model, the emergence of a new magnetic region comes in contact with opposite polarity magnetic fields. Because of convective motions below the photosphere, where the footpoints of the coronal loops are anchored, or frozen-in, to the photosphere, the coronal loops slide over one another to reconnect [107]. In the region of magnetic reconnection, explosive dissipative phenomena occurs such as beams of accelerated particles. The particles moving along the magnetic field lines on the chromosphere precipitate, giving rise to an increase in brightness which is observed in H_α as tow-ribbon flare.

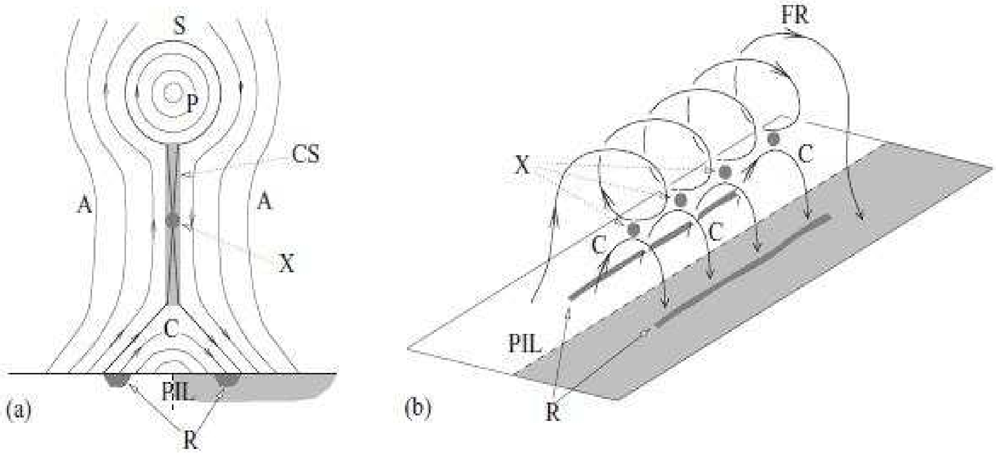

Figure 1: Schematic representation of *Two ribbon flare model.* Adapted from [10].

The detection of magnetic field variations as a signature of flaring activity within solar active regions is one of the main goals in the solar physics studies.

A valid tool to characterize the scaling behavior of these sign-oscillating stuctures is represented by the cancellations analysis. The introduction of the concept of sign-singular measure allows the evaluation of the scale dependent cancellations between fluctuations of opposite sign, which is controled by the presence and characteristics of structures [30, 46, 48, 49]. Application of this technique to two-dimensional, high Reynolds number direct numerical simulations of incompressible MHD equations [44] has shown that turbulent plasmas field fluctuations own scale-dependent cancellations properties, and can thus be studied with such tool.

Cancellation analysis application to the magnetic helicity in solar wind have shown the presence of sign-singular behavior [5], while solar photospheric velocity patterns have been chatacterized as well [11].

Cancellation analysis has also been used to study the complexity of solar magnetic fields inside active regions. The variations of the cancellation exponent (the scaling index used for the characterization) of current helicity and current density, calculated using the photosperic magnetic field vector as measured by ground based telescopes, have been shown to be related to flaring activity of an active region. In several cases, it was observed that enhanced flaring is often accompanied by a drop and subsequential rise of the magnetic complexity, as measured by the cancellation exponent [46, 48, 49].

In this thesis, we propose to study in depth the cancellation analysis in several numerical and experimental systems.

In the first Chapter, after a basic introduction to plasmas dynamics we introduce the main concepts of magnetohydrodynamics (MHD), kinetic description of plasmas, and plasma turbulence, focusing on the statistical properties of the magnetic fields.

In the second Chapter, we describe the cancellation analysis technique, by introducing concepts such as signed measure, partition function and cancellation exponent. Furthermore, we present a model which links the cancellation exponent to the typical fractal dimension of the structures.

In the third Chapter, we present the cancellation analysis of compressible Hall-magnetohydrodynamic turbulent numerical simulations, with an external guide field, to characterize the scaling behavior of the sign-oscillating flow structures and their geometrical properties.

In the fourth Chapter, we apply cancellation analysis to a numerical simulation of hybrid Vlasov-Maxwell system, where fully kinetic proton velocity distribution functions and fluid electrons are included. It accounts for the small scale dynamics up to characteristic lengths of the order of the electron skin depth.

The results obtained through the study of numerical data by means of the cancellation analysis, discussed in chapters 3 and 4, have a twofold relevance.

On one hand, we have been able to describe the formation of structures in numerical plasmas, including time evlolution and transition to turbulence, and parametric dependence of the structures properties. On the other hand, they reveal the capability of the cancellation analysis to capture subtle variations in the dymanical properties of the fields. Numerical simulations allowing the independent evaluation of such properties, this analysis also represents a test for the data analysis technique capability to capture the main properties of plasma turbulent fields.

In the fifth Chapter, the cancellation analysis is finally applied to experimental measurements of solar active regions, using both ground-based and space-based data. First, the magnetic vector as measured by the ground-based THEMIS telescope for the active region NOAA 10019 has been studied, and gave indication of presence of disrupted current filements. The variation of the fractal dimension of the current structures, and in particular their smoothing, is discussed in relationship with occurrence of large flares. Then, in order to improve the quality of the analysis and avoid the typical problems of ground-based observations, (better spatial resolution thanks to the absence of the atmosphere, total temporal coverage thanks to the absence of night eclypse), we applied the cancellation technique to space-based measuraments (HMI-SDO) of AR NOAA 11158. This gave us access to the fine structure of the magnetic fields of the AR, with unprecedented temporal coverage. We will discuss the time variation of the cancellation exponent, and infer important information from its behaviour. The flaring activity for the same AR has been correlated with the cancellation properties of the fields. We will show that significant correlations are present, and that the magnetic complexity unedrgoes significant changes in advance with respect to flaring activity. The statistical significance of the results has finally been tested and discussed.

Chapter 1

Turbulence and intermittency in plasmas

1.1 Basic description of plasma dynamics

1.1.1 The different descriptions of plasmas

Plasmas are ionized gases, often indicated as the "fourth state" of matter. Plasmas are very rare on Earth (for example, produced by electric shock, as lightenings, auroras borealis) but represent about 99% of the known matter in the universe.

The dynamics of a plasma is rather complex, due to the electromagnetic nature of the interactions between the charged particles composing the gas. Its dynamics can be described using sets of differential equations at different approximation levels [12]. The state of plasma is characterized by some quantity and simple assumptions. For the sake of simplicity, it is usually reduced to two kinds of particles, namely electrons (e) and a single kind of positive ions (i, mainly protons). Let $n_{e,i}$ be the density of the particles, $m_{e,i}$ their mass, and e the electron charge. Then:

- The typical particle velocity can be represented by their thermal velocity:

  $$v_{e,i} \simeq \sqrt{\frac{k_B T_{e,i}}{m_{e,i}}} \; ,$$

  where $T_{e,i}$ are the average temperatures of the particles, and k_B is the Boltzmann constant.

- The *electron plasma frequency* is the typical oscillation frequency of a plasma seen as an oscillator, and its reciprocal gives the typical separation time between charges:

  $$\omega_{pe} \simeq \sqrt{\frac{4\pi n_e e^2}{m_e}} \ .$$

  The *ion plasma frequency* can be similarly defined, using the ion mass, density and charge.

- The *Debye lenght* is the ratio between the thermal speed of electrons and their plasma frequency:

  $$\lambda_D \simeq \frac{v_e}{\omega_{pe}} \simeq \sqrt{\frac{k_B T}{4\pi n_e e^2}} \ ,$$

  and is the typical shielding lenght of the charges. In fact, it represents the balance lenght between thermal and electrostatic effects, so that for scales larger than λ_D, the plasma can be seen as electrically neutral.

- The *ion skin depth* inticates the depth in a plasma to which electromagnetic radiation can penetrate and is defined as

  $$\rho_{ii} = \frac{c}{\omega_{pi}} \ ,$$

  where c is the speed of light. This lenght is the typical scale at which the inertia of the ions can not be neglected.

- The *cyclotron frequency* or *Larmor frequency* of electrons and ions is defined if an external magnetic field B is present, which is often the case in plasmas. In that case, the frequency at which electrons and ions turn around the magnetic field lines is

  $$\Omega_{e,i} = \frac{eB}{cm_{e,i}} \ .$$

- The parameter *beta* is defined as

  $$\beta = \frac{8\pi p}{B^2} \ ,$$

p being the kinetic pressure, is the ratio between the kinetic and magnetic pressures. It is useful to describe the state of magnetization of the plasma, and to individuate if magnetic or kinetic effects are predominant in the dynamic.

All these quantities are used to describe the conditions of the plasma, and to use approximations, in order to simplify the equations in the different regimes.

Plasma dynamics can be studied using different descriptions: the full *kinetic* description, necessary when dealing with small scale processes involving the particle interactions; and the *fluid* or *magnetohydrodynamic* approach, an approximation that is useful when only large scales and slow perturbations are involved.

1.1.2 The kinetic description

In kinetic theory the distribution function $f(\boldsymbol{r}, \boldsymbol{v}, t)$ is defined to take into account the probability of finding a particle in the position-velocity phase space $(\boldsymbol{r}, \boldsymbol{v})$,

$$dp_\alpha = f_\alpha(\boldsymbol{r}, \boldsymbol{v}, t) d^3\boldsymbol{r} d^3\boldsymbol{v} \ ,$$

where $\alpha = e, i$ indicates the type of particle. Using this information one can be define the total number of particles as

$$N = \int f_\alpha(\boldsymbol{r}, \boldsymbol{v}, t) d^3\boldsymbol{r} d^3\boldsymbol{v} \ .$$

The distribution function obeys Boltzmann's equation :

$$\frac{\partial f_\alpha}{\partial t} + (\boldsymbol{v} \cdot \boldsymbol{\nabla}) f_\alpha + \frac{\boldsymbol{F}_\alpha}{m_\alpha} \cdot \frac{\partial f_\alpha}{\partial \boldsymbol{v}} = \sum_\beta C_{\alpha\beta} \ , \tag{1.1}$$

where $C_{\alpha\beta}$ is a collision operator that depends on the distribution functions of the relevant species. The force term in this equation is given by external fields, since this equation describes only ordinary gases.

In a collisional (fluid) description of plasmas, regions in between coherent structures are expected to be sites of enhanced dissipation, where processes such as magnetic reconnection and plasma heating may be at work [13]. In many cases the collisional mean free path of particles is much longer than the typical scale lengths involved in these phenomena. For very rarefied plasmas the collision can be neglected. The collision can be neglected also if one is interested in the evolution for times smaller of the collision time, so the equation (1.1) can be rewritten as

$$\frac{\partial f_\alpha}{\partial t} + (\boldsymbol{v} \cdot \boldsymbol{\nabla}) f_\alpha + \frac{\boldsymbol{F}_\alpha}{m_\alpha} \cdot \frac{\partial f_\alpha}{\partial \boldsymbol{v}} = 0 \; . \tag{1.2}$$

The force term in this equation is given by $\boldsymbol{F}_\alpha = \boldsymbol{F}_{ext} + \boldsymbol{F}_{int}$. For plasmas the $\boldsymbol{F}_\alpha$ is often simply the Lorentz forces

$$\boldsymbol{F}_\alpha = q_\alpha \left(\boldsymbol{E} + \frac{\boldsymbol{v} \times \boldsymbol{B}}{c} \right) \; .$$

Equation (1.2) is called *Vlasov equation* and is usually coupled to the Maxwell equations in order to provide closure of the system.

It is worth to emphasize that in the framework of collisionless plasmas, the distribution function can be different from Maxwellian, and this is a manifestations of these complex kinetic processes. The distribution function is modified such as to show increased temperature in the direction parallel to the global mean magnetic field [96]. This can be due to ion-cyclotron resonant interactions [14, 15, 16, 17] or to the generation of field-aligned beams [14].

In order to simplify the physical scenario, a simple model called *hybrid approximation* [18] can be also used. In this context, one considers only large spatial scales and low frequencies, that is to say that the detailed behavior of the electrons is irrelevant because the dynamics of the systems is dominated by ions. In this aproximation the ions are considered as kinetic particles whereas the electrons are represented as massless fluid. In this thesis, we will study the results of a numerical simulation of hybrid Vlasov-Maxwell equations.

1.1.3 The magnetohydrodynamic description

When considering only perturbations occurring on typical time scale larger comparated to the typical termalization time, the distribution function can be assumed to be Maxwellian. This is possible by abandoning the assumption of non-collisionality, by allowing exchanges of energy (termalization) between the various particle species, making the distribution function relax to a Maxwellian.

In this approximation, the particle involved are electrons (of mass m_e) and ions (of mass m_i). Since $m_p \sim 2000 m_e$, it is clear that terms of the dynamics equations containing m_e/m_p can be neglected. This corresponds to ignore the inertia of the electrons in the flow. Since we are only considering time scales larger than the reciprocal of ω_{pe}, the electrons can not be separated by the ions in the MHD approximation, because the plasma adjust as to neutralize possible charge separation within shorter times ($\simeq 1/\omega_{pe}$). In fact, whenever a charge separation is induced in the plasma, an electric field causes the electrons to quickly follow the ions in a time $\simeq 1/\omega_{pe}$: the *quasi-neutrality of charge* $n_i \sim n_e$ is always guaranteed. In this context, plasmas are similar to a fluid whose particles have mass m_i and whose density is then $\rho \simeq m_i n_i$. In the reference system of the ions, one sees a current of electrons (with negligeable mass) that flows obeying the Ohm's.

Finally, when nonrelativistic regime is considered, all the contributions of order $(v/c)^2$ can be neglected in the equations. The conservation laws can then be written for the mass density ρ, flow velocity $\boldsymbol{v}$ and internal energy for mass unit U of the protons [12]:

$$\begin{aligned} \frac{\partial \rho}{\partial t} + \boldsymbol{\nabla} \cdot (\rho \boldsymbol{v}) &= 0 \,, && (1.3) \\ \rho \left[\frac{\partial}{\partial t} + (\boldsymbol{v} \cdot \boldsymbol{\nabla}) \right] \boldsymbol{v} &= \boldsymbol{f} - \boldsymbol{\nabla} p + \boldsymbol{\nabla} \cdot \overline{\overline{\boldsymbol{\sigma}}} \,, && (1.4) \\ \rho \left[\frac{\partial}{\partial t} + (\boldsymbol{v} \cdot \boldsymbol{\nabla}) \right] U &= -p(\boldsymbol{\nabla} \cdot \boldsymbol{v}) - \boldsymbol{\nabla} \cdot \boldsymbol{q} + \sum_{i,j} \sigma_{ij} \frac{\partial v_i}{\partial x_j} + Q \,. && (1.5) \end{aligned}$$

$\boldsymbol{f}$ represents the sum of the external forces acting on the magneto-flow for unit mass. The term $\overline{\overline{\boldsymbol{\sigma}}}$ is the stess tensor excluding the kinetic pressure p contribution, which is treated separately. The term $\boldsymbol{q}$ is the heat flux, and Q is the heat produced inside the system. In many cases, as for the plasmas treated whithin the present work, the only force involved is the Lorentz force, while other kinds of forces, as the gravitational one, are negligible with respect to the electromagnetic interactions. In this case, the force term can be written as:

$$\boldsymbol{f} = \frac{1}{c} \boldsymbol{J} \times \boldsymbol{B} \,, \tag{1.6}$$

where the quasi-neutrality has been used to drop the electric field contribution to the force, that is the Laplace force. The same argument hold for the heat terms, so that the Joule effect is often the only internal source of heat.

It is often possible to use a state equation, so that the number of unknowns is reduced and the system is closed. For example, if the plasma behaves like a perfect gas, the state equation $p = k_B \rho T/m$ can be used to eliminate the kinetic pressure from the equations.

The moments equations must be coupled to the Maxwell equations to include the electromagnetic properties of the plasma. In case of quasi-neutrality of charge, and in non-relativistic regime, the Maxwell equations become:

$$\begin{aligned} \boldsymbol{\nabla} \cdot \boldsymbol{E} &= 0 \,, && (1.7) \\ \boldsymbol{\nabla} \cdot \boldsymbol{B} &= 0 \,, && (1.8) \\ \boldsymbol{\nabla} \times \boldsymbol{E} &= -\frac{1}{c}\frac{\partial \boldsymbol{B}}{\partial t} \,, && (1.9) \\ \boldsymbol{\nabla} \times \boldsymbol{B} &= \frac{1}{c}\frac{\partial \boldsymbol{E}}{\partial t} + \frac{4\pi}{c}\boldsymbol{J} \,, && (1.10) \end{aligned}$$

where $\boldsymbol{E}$ and $\boldsymbol{B}$ are the electric and magnetic fields respectively, ρ_c is the charge density and $\boldsymbol{J}$ the current density. The Ohm's law, in the MHD framework, is rewritten in its generalized form as:

$$\boldsymbol{E} + \frac{1}{c}\boldsymbol{v} \times \boldsymbol{B} = \eta \nabla^2 \boldsymbol{B} \,. \tag{1.11}$$

where η is the resistivity of the plasma.

The Laplace force (1.6), the last Maxwell equation (1.10) and the Ohm's law (1.11) can be now used to rewrite the conservation laws. The mass conservation law (1.3) remains invariate, and so does the energy conservation law (1.5), as far as we do not use any state equation. The impulse conservation law, also called the Newton equation, becomes

$$\rho \left[\frac{\partial}{\partial t} + (\boldsymbol{v} \cdot \boldsymbol{\nabla})\right] \boldsymbol{v} = \frac{1}{4\pi}(\boldsymbol{\nabla} \times \boldsymbol{B}) \times \boldsymbol{B} - \boldsymbol{\nabla} p + \boldsymbol{\nabla} \cdot \overline{\overline{\boldsymbol{\sigma}}} \,, \tag{1.12}$$

The Maxwell equation (1.9) is used to describe the evolution of the magnetic field. In the MHD framework, it can be rewritten as

$$\frac{\partial \boldsymbol{B}}{\partial t} = \boldsymbol{\nabla} \times (\boldsymbol{v} \times \boldsymbol{B}) + \frac{c^2 \eta}{4\pi} \nabla^2 \boldsymbol{B} \,, \tag{1.13}$$

and is called the *induction equation*.

Equations (1.3), (1.12), (1.13) and (1.5) are the full set of the MHD equations, and together with the remaining Maxwell laws, the Ohm's law, and a state equation for the closure, are used to describe the dynamics of a plasma in the MHD approximation. The heat terms q and Q, as well as the stress tensor $\overline{\overline{\sigma}}$, could introduce new variables in the equations, and thus need to be modeled in order to solve the equations.

The MHD equations own a similar structure to the Navier-Stokes equations (NS), which describe the dynamic of a fluid. The main characteristic of both sets of equations is the presence of nonlinear terms $(\boldsymbol{v} \cdot \boldsymbol{\nabla})\boldsymbol{v}$. However, the MHD equations have extra terms describing the coupling between velocity and magnetic field. These nonlinearities lead to scaling of the equations, which is prelude to turbulence.

1.1.4 The incompressible case, and the Elsässer variables

As for the Navier-Stokes equations in the fluid case, the MHD equations are strongly simplified if the flow is incompressible, that is, $\rho = constant$. The mass conservation law simply reduces to the incompressibility condition $\boldsymbol{\nabla} \cdot \boldsymbol{v} = 0$. If the temperature variations are neglected, the energy conservation equation is not needed. Let us introduce the following new variable

$$\boldsymbol{b}(\boldsymbol{r}, t) = \frac{\boldsymbol{B}}{\sqrt{4\pi\rho}} \, ,$$

where $\boldsymbol{b}$ is a rescalded magnetic field which has the dimensions of velocity. Using incompressibility, replacing the magnetic field with the rescalded magnetic field and introducing the kinematic viscosity ν and the magnetic diffusivity $\mu = c^2\eta/4\pi\rho$, the incompressible MHD equations can be written in the simpler form:

$$\begin{aligned} \frac{\partial \boldsymbol{v}}{\partial t} + (\boldsymbol{v} \cdot \boldsymbol{\nabla})\boldsymbol{v} &= (\boldsymbol{\nabla} \times \boldsymbol{b}) \times \boldsymbol{b} - \boldsymbol{\nabla} p + \nu \nabla^2 \boldsymbol{v} \, , && (1.14) \\ \frac{\partial \boldsymbol{b}}{\partial t} &= (\boldsymbol{\nabla} \times \boldsymbol{v}) \times \boldsymbol{b} + \mu \nabla^2 \boldsymbol{b} \, , && (1.15) \\ \boldsymbol{\nabla} \cdot \boldsymbol{b} &= \boldsymbol{\nabla} \cdot \boldsymbol{v} = 0 \, . && (1.16) \end{aligned}$$

In the ideal case ($\nu = 0$ and $\mu = 0$) these equations conserve the total energy (kinetic plus magnetic)

$$E = \frac{1}{2} \int \left(v^2 + b^2 \right) d^3\boldsymbol{r} \, .$$

The previous equations can be compacted (although equivalent) introducing the so called Elsässer variables [19]:

$$\boldsymbol{z}^{\pm} = \boldsymbol{v} \pm \boldsymbol{b} \; .$$

Using these new variables, the MHD equations become

$$\frac{\partial \boldsymbol{z}^{\pm}}{\partial t} + (\boldsymbol{z}^{\mp} \cdot \boldsymbol{\nabla})\boldsymbol{z}^{\pm} = -\frac{1}{\rho}\boldsymbol{\nabla} P_* + \frac{\nu + \mu}{2}\nabla^2 \boldsymbol{z}^{+} + \frac{\nu - \mu}{2}\nabla^2 \boldsymbol{z}^{-} \; , \tag{1.17}$$

$$\boldsymbol{\nabla} \cdot \boldsymbol{z}^{\pm} = 0 \; , \tag{1.18}$$

where $P_* = p + \frac{B^2}{8\pi}$. The conservation of the total energy is equivalent to the conservation of the pseudo-energies

$$E^{\pm} = \frac{1}{4}\int \left(\boldsymbol{z}^{\pm}\right)^2 d^3\boldsymbol{r} \; .$$

It is worth noting that (1.17) and (1.18) admit nonlinear solutions $\boldsymbol{z}^{\mp} = 0$ and $\boldsymbol{z}^{\pm} \neq 0$ with the condition that the total pressure is constant. These solutions corrispond, in the linear case to Alfvén plane waves with arbitrary amplitude $\boldsymbol{v} = \pm\boldsymbol{b}$, where $\boldsymbol{v}$ and $\boldsymbol{b}$ are the transevers components to the propagation direction. These waves propagate with velocity $\boldsymbol{V}_A = \boldsymbol{B}_0/4\pi\rho$ called *Alfvén velocity.* $\boldsymbol{B}_0$ is the component of average magnetic field along the propagation direction. In case of vanishing magnetic field, the two "+" and "–" equations (1.17) become identical, as well as the two equations (1.18), and the NS equations are recovered. The Elsässer formulation highlights a relevant difference in the nonlinear term with respect to ordinary fluids. In fact, the nonlinear interactions occur only between eddies characterized by presence of both $\boldsymbol{z}^{\pm}$ and $\boldsymbol{z}^{\mp}$. It can be shown that different types of fluctuations propagate in opposite direction along $\boldsymbol{B}_0$. Moreover, as we shall see, the *Alfvén effect* can significatly modify the turbulence phenomenology.

1.2 Scaling laws and turbulence

1.2.1 The Reynolds number

The presence and importance of turbulence in a fluid or MHD flow are directly related to the strength of nonlinear effect with respect to dissipation, whose contribution to the dynamics depends on the particular regime. A measure of this comparison is given by *Reynolds number Re*. *Re* is a dimensionless number and provides an estimate of ratio between nonlinear term $(\boldsymbol{v} \cdot \boldsymbol{\nabla})\boldsymbol{v}$ and dissipative term $\nu\nabla^2\boldsymbol{v}$ both contained in the equation (1.14). By dimensional analysis of nonlinear term $(\boldsymbol{v} \cdot \boldsymbol{\nabla})\boldsymbol{v} \sim v_0^2/\ell_0$, and of dissipative term $\nu\nabla^2\boldsymbol{v} \sim \nu v_0/\ell_0^2$, the *Re* turns out to be

$$Re = \frac{\ell_0 v_0}{\nu} \ ,$$

where ℓ_0 and v_0 are the typical length scale and the typical velocity of system. Using the magnetic diffusivity μ instead of kinematic viscosity, the *magnetic Reynolds number* can also be defined as $Re_m = \ell_0 v_0/\mu$. For low Reynolds numbers, the dissipative terms dominate the dynamics of the system, and the fluid motion is quite regular (laminar regime). The nonlinear interactions are small enough for the equations to be linearized, and thus solved. When the *Re* is sufficiently large, the nonlinear effects become dominant and the flow appears to be characterized by a vortical-like structures. In this regime the motion equations cannot be analytically solved (and often not even numerically), and it is useful to approach the problem phenomenologically.

1.2.2 The turbulent cascade

In fluid dynamics, one of the main features of turbulence is the presence of singular structures, as for examples vortices. As the nonlinear terms of MHD equations begin to be relevant, large turbulent structures are formed at some typical scale ℓ_0. The largest eddies in the system are created by some instability occurring in the mean flow, as for example due to an obstacle immersed in the flow. These eddies dacay, giving rise to eddies of smaller size, which in turn will decay into other vortices always smaller, because of the nonlinear interactions (the energy contained in the large eddies is transferred at the smaller eddies). Following this idea it can be argued that turbulent flows at high Reynolds numbers are characterized by presence of eddies that cover a wide range scale. When the Reynolds number is larger than some critical value, the flow is said to be in *fully developed turbulence* regime. In fully developed turbulence it is possible to identify three different ranges of scales. The large scales, at which the energy is injected into the system by some external forcing, are called *integral scales*. The scales at which the dissipation is dominant belong to the *dissipative range*. Between

[hbtp!]

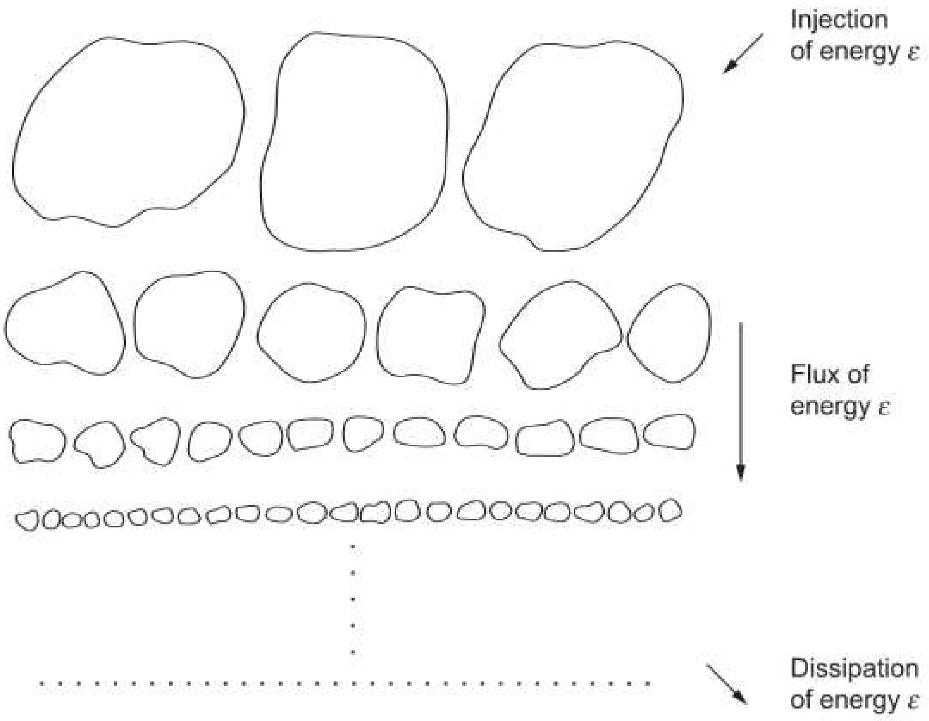

Figure 1.1: A schematic picture of the Richardson cascade. The hierarchy of structures represents the non-linear transfer of energy between different scales. [31]

these two ranges, in which the dynamics is linear, the dominant term in the equations is the non-linear term, so that energy transfers between different wave-vectors are dominating the dynamics. Consequently, the space fills up with fluctuations on a wide range of scales, which also present nontrivial correlations. This range of scales is usually called “inertial range”. This idea has been first visualized in the simple picture of an energy cascade by Richardson (1922).

1.3 Phenomenology of turbulence

1.3.1 The Kolmogorov spectrum

One of the simplest and most valuable tools to study the irregular and multiscale turbulence is by means of energy spectra associated with the field fluctuations. Energy spectra allow, in fact, to capture the main characteristics of the turbulent cascade. It is universally found that the energy spectrum of a turbulent field has power-law behavior (Kolmogorov, 1941, in short K41; see also [31])

$$E(k) \sim k^{-\alpha} \; .$$

Kolmogorov developed a phenomenological interpretation of power-law spectra, originally based on non-magnetized fluids. The main idea is that at large Reynolds numbers, there is a large scale separation between the scale ℓ_0 at which the energy is injected into the system and the scale η at which the energy is dissipated η. In the stationary case, the energy injected at large scale in the system at rate ϵ, must be dissipated at small scale, where dissipative terms of the equations become relevant. Similary, that same amount of energy must be transfered through the intermediate range of scales ℓ, in the inertial range, $\eta \ll \ell \ll \ell_0$. Kolmogorov suggest that in this range the statistical properties depend only on the energy transfer rate and on the scale ℓ, while the dependence on kinematics viscosity only occurs near the boundaries of this in range. The enrgy transfer rate can be dimensionaly estimate as $\epsilon \sim \delta v_\ell^2 / t_\ell$, where δv_ℓ represents the typical velocity fluctuations at the scale ℓ and t_ℓ is the typical time associated to the nonlinear energy transfer process. The latter is called *eddy turnover time*, and can be defined as $t_\ell \sim \ell / \delta v_\ell$. In light of these considerations, the velocity fluctuations can be dimensionally re-written as

$$\delta v_\ell \sim \epsilon^3 \ell^{1/3} \; .$$

Another typical time is $t_\ell^{(\nu)} \sim \ell^2/\nu$, that is the typical time associated with linear dissipative effects. The *Kolmogorov scale*, or dissipative scale, can be found imposing that $t^{(\nu)} = t_\ell$, that is the time when dissipative effects match the nonlinear effects in the dynamics. Then

$$\eta \sim \left(\frac{\nu^3}{\epsilon} \right)^{1/4} \; .$$

The scale dependence of the power spectrum $E(k)$ can now be dimensionally evaluated in the inertial range. In fact, the tipical scale is related to the wave vectors through $\ell \sim 1/k$, so that $E(k) \sim \delta v_\ell^2/k$, thus giving

$$E(k) \sim \epsilon^{2/3} k^{-5/3} \ . \tag{1.19}$$

The power law spectrum (1.19) is whidely observed in experimental data, and is called the *Kolmogorov spectrum*.

1.3.2 The Kraichnan spectrum

Magnetized plasmas turbulent dynamics can be desribed by a similar phenomenology to Kolmogorov, as in the neutral fluids case. Unlike the neutral fluids case, magnetized plasmas are characterized by the presence of Alfvénic fluctuations, namely plasma waves propagating along the magnetic field lines. By sweeping the plasma apart, these can modify the interactions between structures. Such type of phenomenology is well described by the Kraichnan phenomenology. As for the case fluid, whithin the inertial range the statistical properties of turbulent motions depend only on the energy transfer rate and on the scale ℓ. The energy flux accros the scale ℓ cab be written as

$$\Pi_\ell^\pm \sim \frac{(\delta z_\ell^\pm)^2}{t_\ell^\pm} \ , \tag{1.20}$$

where $t_\ell^\pm$ is the typycal duration of the energy transfer at the scale ℓ. Now, as can be seen looking at equations (1.17), the Alfvénic fluctuations propagate in opposite direction along the magnetic field lines, so that the interacting structures are set apart in a time $t_A \sim \ell/V_A$, so modifying the actual interaction time.

In evalutating the time t_ℓ one must take into account that there are two different time scale of interaction. The first is $t_i^\pm \sim \ell/\delta z^\mp$ that corrisponds to the typical time of nonlinear interaction. The second time scale $t_A \sim \ell/V_A$ related at the opposit propagation of Alfvénic fluctuations $\delta z_\ell^\pm$ which move with Alfvénic velocity V_A. For fully developed turbulence Alfvénic time is typically shorter than typical time of nonlinear interaction. The eddy turnover time can then be written as

$$t_\ell^\pm \sim \frac{(t_i^\pm)^2}{t_A^\pm} \sim N^\pm t_A \ ,$$

where $N^{\pm}$ is the number of interactions needed to obtain, for a given vortex, a modification of amplitude $\Delta z^{\pm} \sim \delta z^{\pm}$.

If one consider, for semplicity, the symmetric case $\delta z^{\pm} \sim \delta z$, then Eq.n (1.20) can be rewritten as

$$\Pi_{\ell}^{\pm} \sim \frac{(\delta z)^4}{V_A \ell} \ .$$

Thereby, the MHD power spectrum can be obtained from $E(k) \sim (\delta z)^2/k$ such that

$$E(k) \sim (\Pi V_A)^{1/2} \, k^{-3/2} \ .$$

This power-law spectrum decays (i.e. trasports the energy) with a smaller scaling exponent with respect to the Kolmogorov spectrum, suggesting a less efficent cascade mechanism, as resulting from the Alfvénic sweeping.

1.3.3 Self-similarity

The presence of power-law spectra of the fields fluctuations suggests the existence of self-similarity. This can be easily checked in the MHD equations, in the ideal case. Let $u(x)$ be a scaling variable, and consider a scaling transformation $x \to \lambda x$. Then, the scaling variable is scaling-invariant if there exists a parameter $\mu(\lambda)$ such that

$$u(x) = \mu(\lambda) u(\lambda x) \ .$$

This equation admits a power law solution $u(x) \sim x^h$, where h is the self-similarity parameter defined as $h = -log_{\lambda}\mu$, and is often called *singularity exponent*. The ratio $u(x)/u(\lambda x) \sim \lambda^{-h}$ indicates that the phenomenon is characterized by scaling invariance (absence of characteristic scale).

The cumulative PDF of $u(x)$ is

$$\mathcal{P}\{u(x) \leq \xi\} = \mathcal{P}\{\lambda^{-h} u(\lambda x) \leq \xi\} = \mathcal{P}\{u(\lambda x) \leq \lambda^h \xi\} \ ,$$

that in integral form is

$$\int_{-\infty}^{\xi} P_x(\eta) \, d\eta = \int_{-\infty}^{\lambda^h \xi} .P_{\lambda x}(\beta) \, d\beta$$

From this form the PDFs are easily obtained

$$P_x(\xi) = \lambda^h P_{\lambda x}(\lambda^h \xi) \ . \qquad (1.21)$$

This form suggests the fact that when the scale change by a factor λ the amplitude of observable varying by a factor λ^h for the self-similarity. The PDFs shape to different scales increments don't change if the scaling exponent is constant.

1.4 Intermittency

For more accurate analysis of a turbulent field, the fundamental tool is the statistics of longitudinal field difference accros a separation ℓ, called *field increments*. For a stochastic field $\boldsymbol{\psi}(\boldsymbol{r})$, the field increments can be defined as

$$\delta\psi_\ell(\boldsymbol{r}) = [\boldsymbol{\psi}(\boldsymbol{r}+\ell) - \boldsymbol{\psi}(\boldsymbol{r})] \cdot \boldsymbol{e}(\ell) \; ,$$

where $\boldsymbol{e}(\ell)$ is the unit vector parallel to the space increment. The increments provide informations on the presence of characteristic structure at the given scale ℓ. In order to capture finer details of the scaling properties of the turbulent processes, it is customary to study the statistical properties of the field increments through their *Probability Distribution as Functions PDFs* and the corresponding high order moments, the *Structure Functions*, and their dependence on the scale.

If the PDF $P(x)$ of a stochastic variable x is known, then it is possible to compute the n-th moments defined as:

$$\langle x^n \rangle = \int x^n \, P(x) \, dx \; .$$

The first order ($n = 1$) represents the mean of distribution, while the second order ($n = 2$) is the variance $\sigma^2 = \langle (x - \langle x \rangle)^2 \rangle$. In principle, the knowledge of n-th moment allows to recover the whole $P(x)$.

Gaussian distrubutions are a peculiar case, because they describe the statistical properties for many physical phenomena. Gaussian PDF needs only the first two moments to be completely determined. However, if the PDF is not Gaussian, one needed to analyze also moments higher than the second-order to fully characterize the statistical properties of process.

Another tool to investigate the statistical properties of turbulent flow is represented by *structure functions* defined as:

$$S_p(\ell) = \langle \delta\psi_\ell^p \rangle \; ,$$

where $\delta\psi_\ell$ are the longitudinal increments. Structure functions exhibit most often scaling law in the inertial range

$$S_p(\ell) \sim \ell^{\zeta_p} \, .$$

In the Kolmogorov theory this scaling exponent satisfy the linear relation $\zeta_p = p/m$, where $m = 3$ for the fluid case and $m = 4$ for MHD case.

In system where turbulence is fully developed the PDFs shapes change with the scale ℓ (see for example [31]). At large scales the PDFs are more or less Gaussian, while as the scale decreases the tails become thicker and sharper peaks appear. This evolution indicates that large increments become more and more probable as scale get smaller, indicanding that the flow is characterized by coherent structures localized in space.

Many works have shown that the scaling exponents deviate from Kolmogorov predictions, displaying a nonlinear dependence on p where neither the Kolmogorov nor the Kraichnan have been found. This deviation from Kolmogorov theory are due to the presence of the same strong fluctuation that breakdown *self-similarity*. The breakdown self-similarity produces the scale variation of the PDFs called *intermittency*, and is the signature of the presence of small scale structures in the flow.

Chapter 2

Cancellation analysis and structures

2.1 Introduction

As we have mentioned in previous Chapter, self-similarity is one frequent signature of complex flows characterized by strong nonlinearities. Huge amount of efforts have been deployed in determining scaling laws both in geophysical and astrophysical flows, in the laboratory and using numerical simulations. The nonlinearity of the scaling exponents of the structure functions, typical of intermittent turbulent systems, is due to the presence of strong localized turbulent structures both in space and time. In turbulent flows, sheets, spirals filaments of vorticity have been observed both in incompressible [20, 21, 22, 23] and in the compressible cases [24]. These structures are locally complex and present rapid fluctuations, which can result in field cancellations. In plasmas, current and vorticity filaments have extensively been oberved in two-dimensional MHD [25, 26] corresponding to current and vorticity sheets in the three-dimensional case [27, 28, 29]. Such structures are locally complex in three dimension [29] as well as in two dimension. In turbulent fields, the geometrical properties of such structures can be studied using the cancellation analysis introduced by Ott *et al.* [30].

2.2 The signed measure and the cancellation exponent

As discussed in the introduction, turbulent plasmas are often characterized by scale dependent formation of energetic and localized structures. These represents regions where dissipation of energy is enhanced, and are believed to be responsible for the anomalous scaling of the structure functions. Intermittency and multifractality are strictly related to their presence [31]. Structures such as current sheets and vorticity filaments are continuously observed in numerical simulations [32, 33, 34, 35, 36, 37]. Solare wind measurements have also revealed the presence of structures of different type (current sheets, rotational discontinuities, vortices) [38, 39, 40, 41]. Since structures can be seen as smooth regions embedded in a highly fluctuating field, they can be associated to scale dependent changes of the sign of the fields gradients. The introduction of a sign-singulare measure (as opposed to a positive defined probability measure) allows the characterization of the scaling properties of sign oscillations of the fields [30]. The signed measure of a scalare field $f(\mathbf{r})$ with zero mean, defined on a d-dimensional set $Q(L)$ of size L, can be introduced as follow. Let $\{Q_i(l) \subset Q(L)\}$ be a partition of $Q(L)$ in disjoint subsets of size l. Then, for each scale l and for each set of boxes $Q_i(l)$, the signed measure is defined as

$$\mu_i(l) = \frac{\int_{Q_i(l)} \,\mathrm{d}\mathbf{r}\; \mathbf{f}(\mathbf{r})}{\int_{Q(L)} \,\mathrm{d}\mathbf{r}\; |\mathbf{f}(\mathbf{r})|} \;. \tag{2.1}$$

As the scale of the subset $Q_i(l)$ increases, cancellations between small size structures of opposite sign become more probable within each box. The way this happens can be statistically characterized through the partition function

$$\chi(l) = \sum_{Q_i(l)} |\mu_i(l)| \tag{2.2}$$

where the sum is extended to all disjoint subset $Q_i(l)$. Let A be a subset such that $A \subset Q(L)$ for which the measure $\mu(A) \neq 0$. If for any scale l there exists an additional subset $B \subset A$ such that $\mu(B) = -\mu(A)$, then the measure is called *sign singular*. When the measure is sign singulare the partition function is empirically found to obey a power low scaling $\chi(l) \sim l^{-\kappa}$. The power κ is called *cancellation exponent*, and represents a quantitative measure of the cancellation efficiency. The cancellation exponent is more formally defined through

$$\kappa = \lim_{r \to 0} \frac{\ln \chi(r)}{\ln(1/r)} \ . \tag{2.3}$$

For example, a smooth (continuous) field has constant partition function ($\kappa = 0$), whereas for a fully stochastic process $\kappa = d/2$ ([42]), d being the topological dimension. Values $\kappa < d/2$, indicate the presence of sign-persistent (*i. e.* smooth) structures, which result in less efficient cancellations than for a random field, while $\kappa > d/2$ indicates the presence of sign-antipersistent fluctuations, as for example due to positive and negative contiguous structures, which result in more efficient cancellations than for random fields. More generally, if a field $\mathbf{g}(\mathbf{r})$ is homogeneous with a Hölder scaling exponent h, that is if $\langle \|\Delta \mathbf{g}(\mathbf{l})\| \rangle = \langle \|\mathbf{g}(\mathbf{r}+\mathbf{l}) - \mathbf{g}(\mathbf{r})\| \rangle \sim l^h$ then the cancellation exponent of its derivative $f \equiv \mathrm{d}g/\mathrm{d}r$ is $\kappa = 1 - h$ [42, 43]. Thus, cancellation exponents characterize the field fluctuations properties, and in particulare the topology of structures.

2.3 Cancellation exponents and fractal dimensions of structures

A simple geometrical argument, based on the separation of the field in correlated (the structures) and uncorrelated (the background field) subsets, allows to establish a phenomenological relationship between the cancellation exponent and the fractal dimension D of the typical dissipative structures of the flow.

For turbulent flow, the Taylor micro-scale $\lambda = (\langle v^2 \rangle / \langle \omega^2 \rangle)^{1/2}$ [31], where ω is the vorticity and v the velocity field, gives a mean scale over which a field is correlated. In this case, the decomposition of a scalare field can be made using correlated (of fractal dimension D with cutoff scale λ) and uncorrelated points (of fractal dimension d-D, i.e. the structures codimension). If the field is homogeneous, one can estimate the partition function (2.2) as the number boxes of size l, namely $(L/l)^d$, times the integral over a single generic box $Q_i(l)$

$$\chi(l) \ = \ \sum_{Q_i(l)} \left| \frac{\int_{Q_i(l)} d\boldsymbol{r}\, f(\boldsymbol{r})}{\int_{Q(L)} d\boldsymbol{r} |f(\boldsymbol{r})|} \right| \sim \frac{1}{L^d f_{\mathrm{r.m.s.}}} \left(\frac{L}{l}\right)^d \left| \int_{Q(l)} d\boldsymbol{r}\, f(\boldsymbol{r}) \right| \ .$$

The scaling of the partition function can be estimated by integrating the signed measure over smaller sub-boxes of size λ^d, $Q(\lambda) \subset Q(l)$. Integration of the field over each $Q(\lambda)$ returns the r.m.s value of the field, $f_{r.m.s.} = \langle f^2 \rangle^{1/2}$. Brackets indicate the average over the whole domain $Q(L)$. One can then estimate the number of contributing boxes, by considering separately the correlated dimensions $(l/\lambda)^D$ (which will contribute proportionally to the volume occupied by correlated structures, i.e. the number of sub-boxes covering the structures) and uncorrelated dimension $(l/\lambda)^{(d-D)/2}$ (which will contribute, for statistical reasons, proportionally to the square rooth of the volume occupied by uncorrelated fluctuations, i.e. to the square root of the number of sub-boxes covering the uncorrelated fluctuations), in the sub-box $Q(\lambda)$. Therefore, assuming homogeneity, the partition function can be rewritten as

$$\chi(l) \sim \frac{\lambda^d f_{\mathrm{rms}}}{L^d f_{\mathrm{rms}}} \left(\frac{L}{l}\right)^d \left(\frac{l}{\lambda}\right)^D \left(\frac{l}{\lambda}\right)^{\frac{d-D}{2}} \sim \left(\frac{l}{\lambda}\right)^{-\frac{d-D}{2}} \sim \left(\frac{l}{\lambda}\right)^{-\kappa} .$$

The relationship between the cancellation exponent and the fractal dimension is then simply

$$\kappa = (d - D)/2 . \tag{2.4}$$

It should be kept in mind that, because multifractality is ubiquitous in MHD turbulence, the use of one single fractal dimension cannot capture all the features of the scaling. Nonetheless, D still represents a useful indicator for the topological characteristics of the “mean” intermittent structures of the flow.

Chapter 3

Topological properties in Hall-magnetohydrodynamics with a strong guide field

3.1 Three-dimensional Hall-MHD

3.1.1 Introduction

Magnetohydrodynamics (MHD) is a reasonable theoretical framework to describe the large scale dynamics of a plasma. However, when a more detailed description is needed (for instance, when the physical context favors the development of small scales) it is most appropriate to consider a two fluids models. Two fluids effects can be considered through a generalized Ohm's law which include the Hall current, required for phenomena with characteristic length scales comparable or smaller than the ion skin depth c/ω_{pi} (c is the speed of light, and ω_{pi} is the ion plasma frequency). Among its manifestations, the Hall current causes the magnetic field to freeze in the electron flow instead of being carried along with the bulk velocity field (in an ideal plasma). Another important feature of the ideal Hall-MHD description is the self-consistent presence of electric fields parallel to the mean magnetic field. Hall-MHD has recently been invoked in advancing our understanding of phenomena ranging from dynamo mechanisms [50], magnetic reconnection [51, 52, 53], and accretion disks [54, 55], and to the physics of turbulent regimes [56, 57, 58, 59].

In many cases of interest, such as in fusion devices or geophysical and astrophysical plasmas, a strong externally supported magnetic field is present. In such cases, a new reduced model has been proposed, reduced Hall Magnetohydrodynamics (RHMHD) model [60, 61, 62]. In this approximation, the fast compressive Alfvén mode is eliminated, while the shear Alfvén and the slow magnetosonic modes are retained [63]. This model is an extension of the previously known reduced MHD (RMHD) to include the Hall effect. The RMHD equations have been used to investigate a variety of problems such as current sheet formation [64, 65], non-stationary reconnection [66, 67], the dynamics of coronal loops [68, 69, 70, 71], and the development of turbulence [72]. The self-consistency of the RMHD approximation has been analyzed in ref. [73]. Moreover, numerical simulations have been used to assess the validity of the RMHD equations by directly comparing its predictions with compressible MHD equations in a turbulent regime [74]. The validity of the RHMHD model has also been studied in the same way [61].

The properties of small scale structures in magnetohydrodynamic and Hall-magnetohydrodynamic turbulence have been recently extensively studied. In particular, attention has been paid to the geometrical properties of current sheets in HMHD, as these structures are associated with magnetic flux reconnection and magnetic energy dissipation, processes of uttermost importance in astrophysics and space physics [76, 78, 77, 75].

However, studies have provided conflicting results so far, so that the debate on the effect of the Hall term on the generation of turbulent structures is still open. For example, some recent numerical simulations have indicated that current sheets in presence of Hall effect become wider than in MHD (see, e.g., [79]), while, on the contrary, other studies have shown the presence of thinner structures [37].

Previous studies of turbulent HMHD have shown that a knee in the spectrum of the spectrum of the current density is located at wavenumber corresponding to the inverse of the ion skin depth [80, 81, 82, 83]. Since this knee can be associated with the average thickness of the current sheets, its shift was interpreted as a thickening of the current sheets with increasing Hall effect [84]. This result is in good agreement with experimental observations, which confirm that the current sheets thickness in presence of the Hall effect is indeed given by the ion skin depth [85].

On the other hand, other studies have observed formation of thinner structures when Hall effect increases, suggesting that HMHD is more intermittent than MHD [37]. This was also observed in solar wind turbulence, *e.g.* using the Cluster spacecraft magnetic data [86, 87]. Incidentally, other instances of solar wind observations of high-frequency magnetic field fluctuations from the same spacecraft indicated that while large scales are compatible with multifractal intermittent turbulence, small scales show non-Gaussian self-similarity [88].

Using the set of simulations that will be studied here, in a previous work the effect of the Hall term has been analyzed in terms of global magnitudes (*e.g.*, the mean square current density $\langle j^2 \rangle$ and vorticity $\langle \omega^2 \rangle$), characteristic times of the flow, energy cascade and qualitative features of the flow structures [79]. The Hall term turned out to affect mostly the scales between the Hall scale and the dissipation scale. This produces an enhancement of the energy transfer in such scale range, and therefore the accumulation of energy decreases. This corresponds to an effective shift of the dissipation scale toward smaller scales. This was estimated by observing an increasingly sharp steepening of the energy spectrum in the Hall range, when the separation between the Hall scale and the dissipation scale is larger. This suggests the possible generation of smaller scales when the Hall effect increases. Qualitative observation of current sheets showed that such smaller scale structures become wider as the Hall effect increases.

In another work [89], a detailed and rigorous study of intermittency has been performed. In presence of Hall effect, field fluctuations at scales smaller than the ion skin depth become substantially less intermittent, with scaling properties close to self similarity.

The quantitative measure of the intermittency is crucial to understand the topological distribution of dissipation in magneto-fluids and plasmas, and it can also provide constraints for theoretical study of phenomena such as magnetic energy dissipation and reconnection. Following recent results as briefly summarized above, it is thus not clear whether HMHD small scale structures are thinner than in MHD, making HMHD more intermittent than MHD, or, on the contrary, they are more space filling, causing intermittency to decrease because of the Hall effect. The main purpose of this Chapter is to quantitatively evaluate the characteristics of the small scale structures and their features with respect to the magnitude of the Hall effect.

In order to gain more insight on the actual effect of the Hall term on flow structures, here we study the geometrical properties of the vorticity and current field, using an explicit and quantitative approach. Our study focuses on the estimation of the cancellation exponents, as introduced by Ott et al. [30]. Such exponents provide a simple characterization of the flows, and are phenomenologically related with the fractal dimension of the typical structure [44]. Finally, corroborated by the aforementioned studies, we show that the Hall effect affects current sheets mainly in two ways. On one hand, the current (and vorticity) sheets widen, while on the other hand they unravel, reaching a more complex topology. This fragmentation, which could be seen as formation of "micro-sheets", turns out to be more and more evident as the Hall effect increases.

3.1.2 Reduced MHD and HMHD models

For a compressible flow, the HMHD equations can be written (in dimensionless form) as

$$\frac{\partial \boldsymbol{u}}{\partial t} - \boldsymbol{u} \times \boldsymbol{\omega} = -\boldsymbol{\nabla}\left(\frac{\boldsymbol{u}^2}{2} + \frac{\rho^{\gamma-1}}{M_S^2(\gamma-1)}\right) + \\ + \frac{1}{M_A^2}\frac{\boldsymbol{J}\times\boldsymbol{b}}{\rho} + \nu\frac{\nabla^2\boldsymbol{u}}{\rho} + \left(\delta + \frac{1}{3}\nu\right)\frac{\boldsymbol{\nabla}(\boldsymbol{\nabla}\cdot\boldsymbol{u})}{\rho}, \tag{3.1}$$

$$\frac{\partial \boldsymbol{A}}{\partial t} - \boldsymbol{u}\times\boldsymbol{b} = -\epsilon\frac{\boldsymbol{J}\times\boldsymbol{b}}{\rho} - \boldsymbol{\nabla}\phi + \eta\nabla^2\boldsymbol{A}, \tag{3.2}$$

$$\frac{\partial\rho}{\partial t} + \boldsymbol{\nabla}\cdot(\rho\boldsymbol{u}) = 0, \tag{3.3}$$

$$\boldsymbol{\nabla}\cdot\boldsymbol{A} = 0. \tag{3.4}$$

In these equations, $\boldsymbol{u}$ is the velocity field, $\boldsymbol{\omega}$ is the vorticity field, $\boldsymbol{J}$ is the current, $\boldsymbol{b}$ is the magnetic field, ρ is the density of the plasma, and $\boldsymbol{A}$ and ϕ are respectively the magnetic and electric potentials. A barotropic law is assumed for the plasma, with the pressure given by $p = C\rho^\gamma$, where C is a constant and $\gamma = 5/3$. Equation (3.4) is the Coulomb gauge, which acts as a constraint that fixes the electric potential in Eq. (3.2). Control parameters of the system are the sonic Mach number M_S, the Alfvén Mach number M_A, the viscosities ν and δ (here we consider $\nu = \delta$), and the resistivity η. In our study, the most important control parameter is the Hall coefficient $\epsilon = \rho_{ii}/L$, where ρ_{ii} is the ion skin depth and L is the characteristic scale of turbulence. When $\epsilon = 0$, the equations above result in the well known compressible MHD equations.

In presence of a strong guide field, the equations above can be written using the reduced approximation often used in magnetohydrodynamics (see, e.g., [91, 92]). The approximation assumes that the magnetic field can be written as

$$\boldsymbol{b} = B_0 \hat{\boldsymbol{z}} + \boldsymbol{b}', \tag{3.5}$$

where B_0 is the intensity of the guide magnetic field aligned with the $\hat{\boldsymbol{z}}$ direction, and $\mathbf{b}'$ is such that $|\mathbf{b}'|/B_0 \ll 1$.

For convenience, when writing the dimensionless equations we assume, without loss of generality, that $B_0 = 1$. We then decompose the velocity and magnetic field fluctuations in terms of scalar potentials as

$$\mathbf{u} = \nabla \times (\varphi \hat{\mathbf{z}} + f \hat{\mathbf{x}}) + \nabla \psi, \tag{3.6}$$

and

$$\mathbf{b}' = \nabla \times (a \hat{\mathbf{z}} + g \hat{\mathbf{x}}) \,. \tag{3.7}$$

Equation (3.7) ensures that the magnetic fields remains divergence free, while Eq. (3.6) gives us a compressible flow. The potentials f and g allow for dynamical components of the fields parallel to the guide field, and ψ describes an irrotational component of the velocity field. Then, Eqs. (3.1-3.4) can be written as (for the details see [93] and [62, 94, 79])

$$\frac{\partial u}{\partial t} = \frac{\partial b}{\partial z} + [\varphi, u] - [a, b] + \nu \nabla^2 u, \tag{3.8}$$

$$\frac{\partial \omega}{\partial t} = \frac{\partial j}{\partial z} + [j, a] - [\omega, \varphi] + \nu \nabla^2 \omega, \tag{3.9}$$

$$\frac{\partial a}{\partial t} = \frac{\partial (\varphi - \epsilon b)}{\partial z} + [\varphi, a] - \epsilon [b, a] + \eta \nabla^2 a, \tag{3.10}$$

$$\frac{\partial b}{\partial t} = \beta_p \frac{\partial (u - \epsilon j)}{\partial z} + [\varphi, b] + \beta_p [u, a] - \epsilon \beta_p [j, a] + \eta \beta_p \nabla^2 b, \tag{3.11}$$

where

$$u = -\partial_y f, \tag{3.12}$$

$$\omega = -\nabla_\perp^2 \varphi, \tag{3.13}$$

$$b = -\partial_y g, \tag{3.14}$$

$$j = -\nabla_\perp^2 a, \tag{3.15}$$

and the notation $[A, B] = \partial_x A \partial_y B - \partial_x B \partial_y A$ is employed for the Poisson brackets. The potential ψ was eliminated using the equation for the pressure. Finally, $\beta_p = \beta\gamma/(1 + \beta\gamma)$ is a function of the plasma β. As in the previous set of equations, these equations become the compressible RMHD equations when $\epsilon = 0$.

3.1.3 Numerical simulations

Simulations analyzed in this have been extensively described in Ref. [79]. We use a standard parallel pseudo-spectral code to evaluate the nonlinear terms and solve numerically the equations [95]. A second-order Runge-Kutta time integration scheme is used. The magnetic field fluctuations in all simulations are less than 10% of the external magnetic field value, so we are in the range of validity of the RHMHD model. Periodic boundary conditions are assumed in all directions of a cube of side $2\pi L$ (where $L \sim 1$ is the initial correlation length of the fluctuations, defined as the length unit). The Runs performed throughout this Chapter do not contain any magnetic or velocity external stirring terms, so the RHMHD system is let to evolve freely. To generate the initial conditions, we excite initially Fourier modes (for both magnetic and velocity field fluctuations) in a shell in k-space with wave numbers $1 \leq k \leq 2$, with the same amplitude for all modes and with random phases. Only plane-polarized fluctuations (transverse to the mean magnetic field) are excited, so the initial conditions are Alfvén mode fluctuations with no magnetosonic modes. In the set of simulations, spatial resolution is 512^2 grid points in the plane perpendicular to the external magnetic field and 32 grid points in the parallel direction. In fact, higher resolution is required in the planes perpendicular to B_0, with respect to the parallel direction. This is due to the fact that the dynamics of the system generates structures mostly along the direction perpendicular to B_0. The kinetic and magnetic Reynolds numbers are defined respectively as $R = 1/\nu$, $R_m = 1/\eta$, based on unit initial r.m.s. velocity fluctuation, unit length, and dimensionless values for the viscosity and diffusivity. For all the Runs, we used $R = R_m = 1600$ (i.e., $\nu = 1/1600$, $\eta = 1/1600$). We also considered a Mach number $M_S = 1/4$, and an Alfvén Mach number $M_A = 1$.

Four values of the Hall parameter were considered, namely $\varepsilon = 0$ (MHD case), 1/32, 1/16, and 1/8. Data from simulations with such values of ε will be labeled as Run 1, 2, 3 and 4, respectively. As the numerical domain used has size 2π (see above), these values correspond respectively to ion skin depths with associated wave numbers $k_\varepsilon = \infty$, 32, 16, and 8, and to scales of ρ_{ii} =0, 0.03, 0.06 and 0.125.

Figures 3.1, 3.2, 3.3 and 3.4 show some example of current components.

Left hand panels show, for each Run, two dimensional cuts in the perpendicular plane of one perpendicular component j_x (Figures 3.1 and 3.2) and of the parallel component j_z (Figures 3.3 and 3.3), for one snapshot

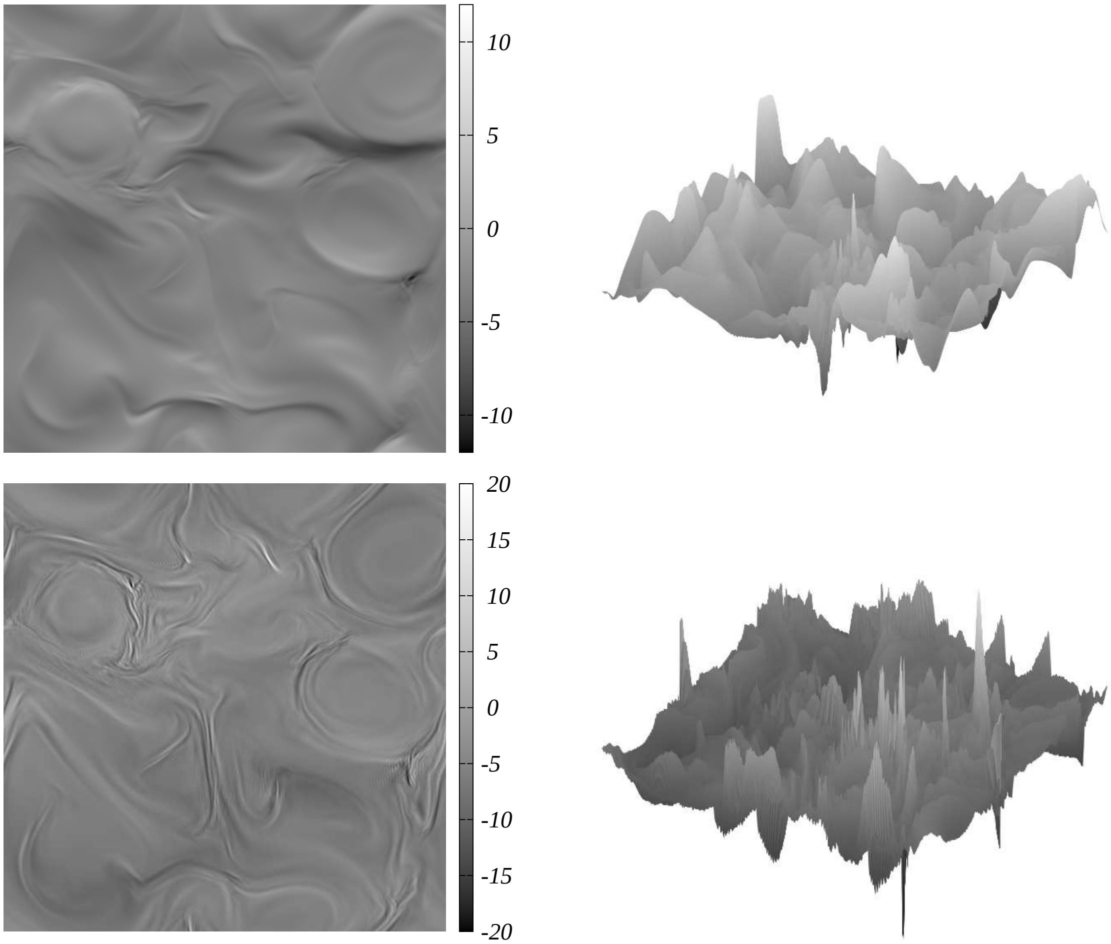

Figure 3.1: Left panels: slices of the perpendicular current component j_x (in adimensional units) in the perpendicular plane, for the $\varepsilon = 0$ and $\varepsilon = 1/32$ and used in this work (ε increasing from top to bottom). Right panels: the same fields, seen at an arbitrary tilt angle, highlighting the presence of alternate sign structures at all scales. In these panels, the scale of grays is arbitrary.

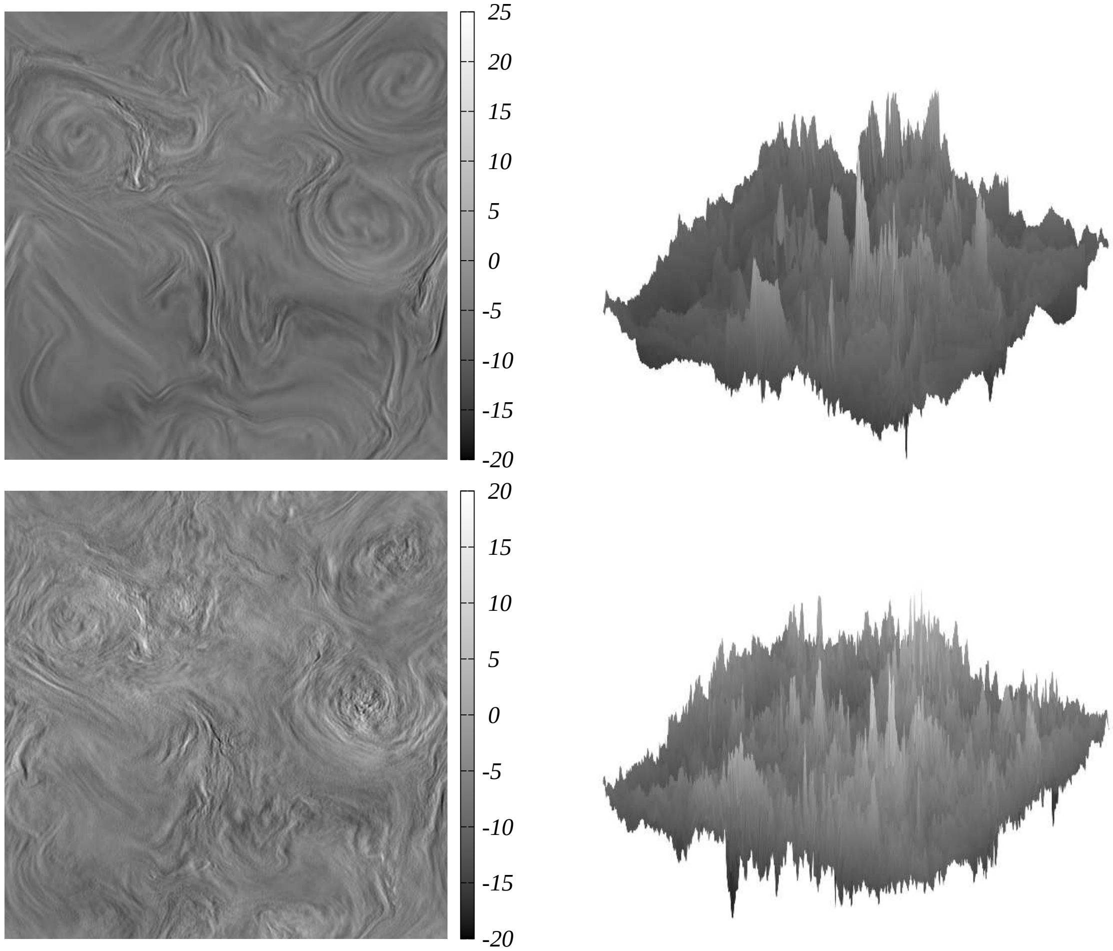

Figure 3.2: Left panels: slices of the perpendicular current component j_x (in adimensional units) in the perpendicular plane, for the $\varepsilon = 1/16$ and $\varepsilon = 1/8$ and used in this work (ε increasing from top to bottom). Right panels: the same fields, seen at an arbitrary tilt angle, highlighting the presence of alternate sign structures at all scales. In these panels, the scale of grays is arbitrary.

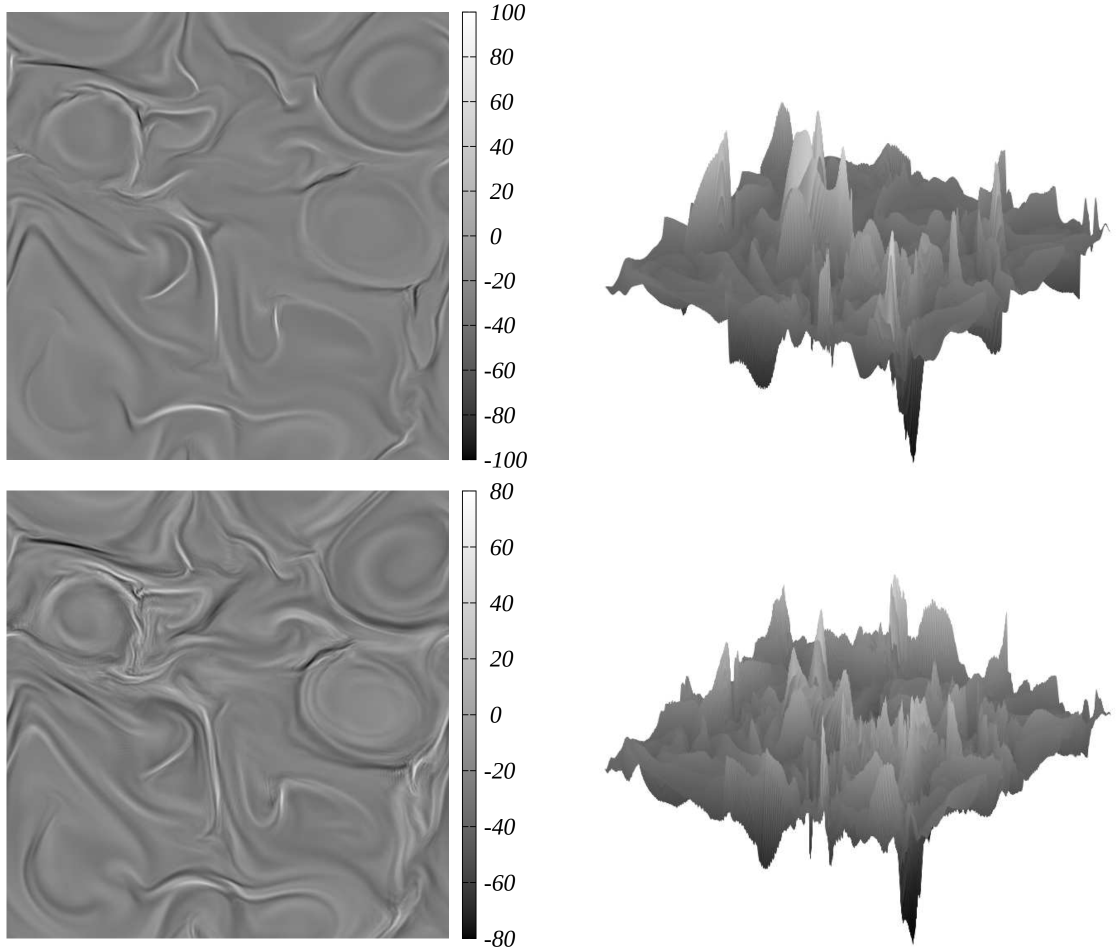

Figure 3.3: Left panels: slices of the perpendicular current component j_z (in adimensional units) in the perpendicular plane, for the $\varepsilon = 0$ and $\varepsilon = 1/32$ and used in this work (ε increasing from top to bottom). Right panels: the same fields, seen at an arbitrary tilt angle, highlighting the presence of alternate sign structures at all scales. In these panels, the scale of grays is arbitrary.

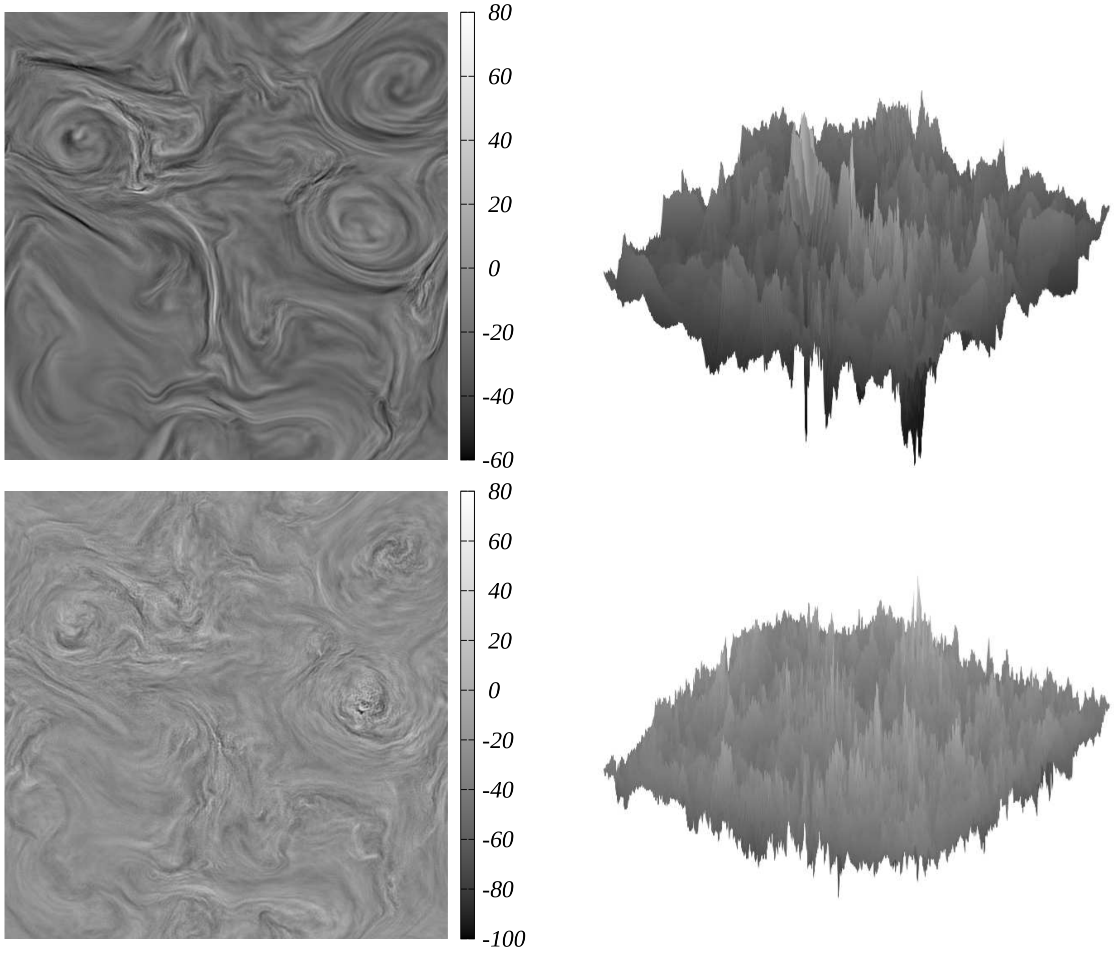

Figure 3.4: Left panels: slices of the perpendicular current component j_z (in adimensional units) in the perpendicular plane, for the $\varepsilon = 1/16$ and $\varepsilon = 1/8$ and used in this work (ε increasing from top to bottom). Right panels: the same fields, seen at an arbitrary tilt angle, highlighting the presence of alternate sign structures at all scales. In these panels, the scale of grays is arbitrary.

of the simulation in the statistically steady state (when $t = 4.5$). On the right panels, the same field is plotted with an arbitrary tilt angle, in order to highlight the chaotic alternation of positive and negative fluctuations of the fields. From visual inspection, it appears evident that structures become more fragmented as ε increases.

Figure 3.5 shows the total energy spectra $E(k)$, integrated on spheres of radius k, for the four Runs. The ion skin depth scale is also indicated. Despite the limited wave vectors range does not allow the observation of power law scaling, the large scale part of the spectra is compatible with the typical Kolmogorov scaling $\alpha = 5/3$. For the largest ε (Run 4), a secondary scaling region emerges at scales smaller than the ion skin depth, compatible with the typical power law spectrum for reduced Hall MHD, $\alpha = 7/3$.

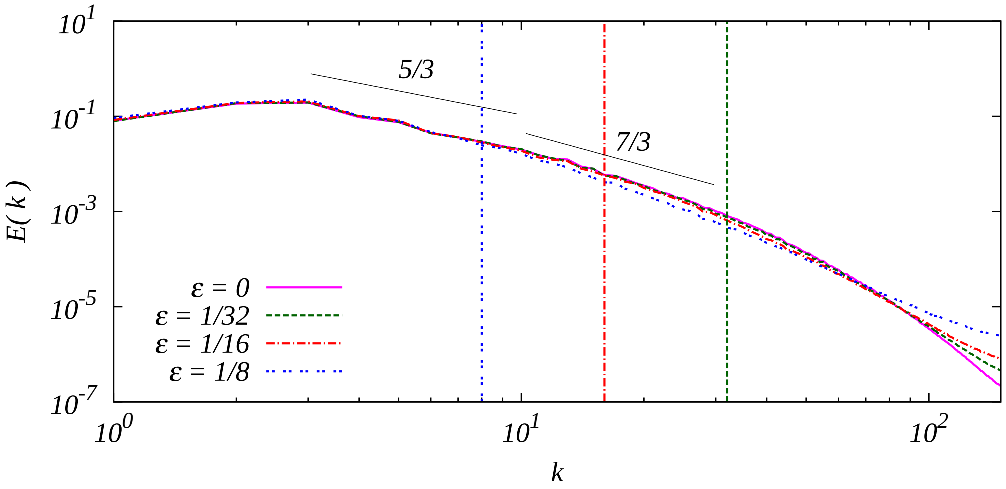

Figure 3.5: The total energy spectra for the four Runs (see legend). The vertical lines represents the values of the inverse ion skin depth for the three Runs with nonvanishing Hall term. Phenomenological predictions for the MHD range and for the Hall range are also indicated.

It was recently stressed that well resolved numerical simulations are necessary in order to accurately quantify high order statistics and intermittency in MHD [90]. In particular, it has been claimed that if the flow is not properly resolved, a partial thermalization of the small scales may result in artificial Gaussian statistics and an artificial decrease of the intermittency. Wan et al. [90] also argued that an MHD simulation can be considered well resolved, if the kurtosis of the current is independent on the spatial resolution. In order to evaluate the sensitivity to the grid resolution of our system, two different realizations have been performed with higher spatial resolution of $768^2 \times 32$ and $512^2 \times 64$ grid points, respectively. Using the same set of parameters, diagnostics such as structure functions, scaling exponents, and PDFs of field fluctuations have been used to show that scaling and intermittency properties are not affected by resolution. In the MHD and HMHD Runs analysed here, the requirement of kurtosis convergence is fulfilled, at least up to the level of expected statistical fluctuations. It is thus possible to conclude that the simulations are well resolved, and satisfies the stringent criteria of Wan et al. [90]. The resolution analysis is shown in detail in the Ref. [89].

3.1.4 Results

For our analysis, we have considered four snapshots of RHMHD simulations, performed using four different values of the Hall parameter ε, as indicated in Section 3.1.3. All the snapshots are taken in a statistically steady state of the system, at $t = 4.5$. The fields anlyzed here are the three components of the current $\mathbf{j}$ and of the vorticity ω, already shown in Figures 3.1, 3.2, 3.3 and 3.4. In order to estimate the partition functions, we divided the simulation domain of size $L^3 = (2\pi)^3$ in subsets of variable size $l_x \times l_y \times l_z$, with $l_x = l_y = l_\perp$ and $l_z = l_\parallel$. Note that, in order to maximize the number of possible integer partitions, about 1% of the $L^3 = (2\pi)^3$ domain has been trimmed. This procedure does not affect the results.

Figure 3.6 shows one examples of two dimensional cuts of the signed measure computed for the parallel component of the current j_z in the plane x-y for $\varepsilon = 1/16$, and for four different partition box sizes. As expected, the coarse graining of the partition leads to cancellations at larger scales, so that small scale structures (the current filaments clearly evident at small scales) gradually disappear. Similar behavior is seen for all fields components, and for any value of the Hall parameter larger than zero. In absence of Hall effect, structures are smoother and well resolved, and the effect of cancellations is less evident.

From the signed measures, partition functions (2.2) have been computed for all components of the current $\mathbf{j}$ and of the vorticity ω as a function of the two scale parameters $l_\perp$ and $l_\parallel$. Figure 3.7 shows two examples, for two different components, j_x (left panel) and j_z (right panel), at $\varepsilon = 1/16$. The different curves of each panel refer to three different values of the parallel scale $l_\parallel$. While scaling properties are present in the perpendicular direction $l_\perp$, the partition functions decrease with the parallel scale $l_\parallel$ is somewhat smoother and less defined, as will be discussed later. This is due to the fact that in RHMHD the turbulent cascade is mainly developed in the planes perpendicular to the mean magnetic field. For this reason, we will mainly concentrate on the scaling properties in the perpendicular planes, by selecting one particular parallel scale ($l_\parallel = 0.03$), and we will leave the discussion of the parallel scale decay to the last Section of this Chapter. However, we have

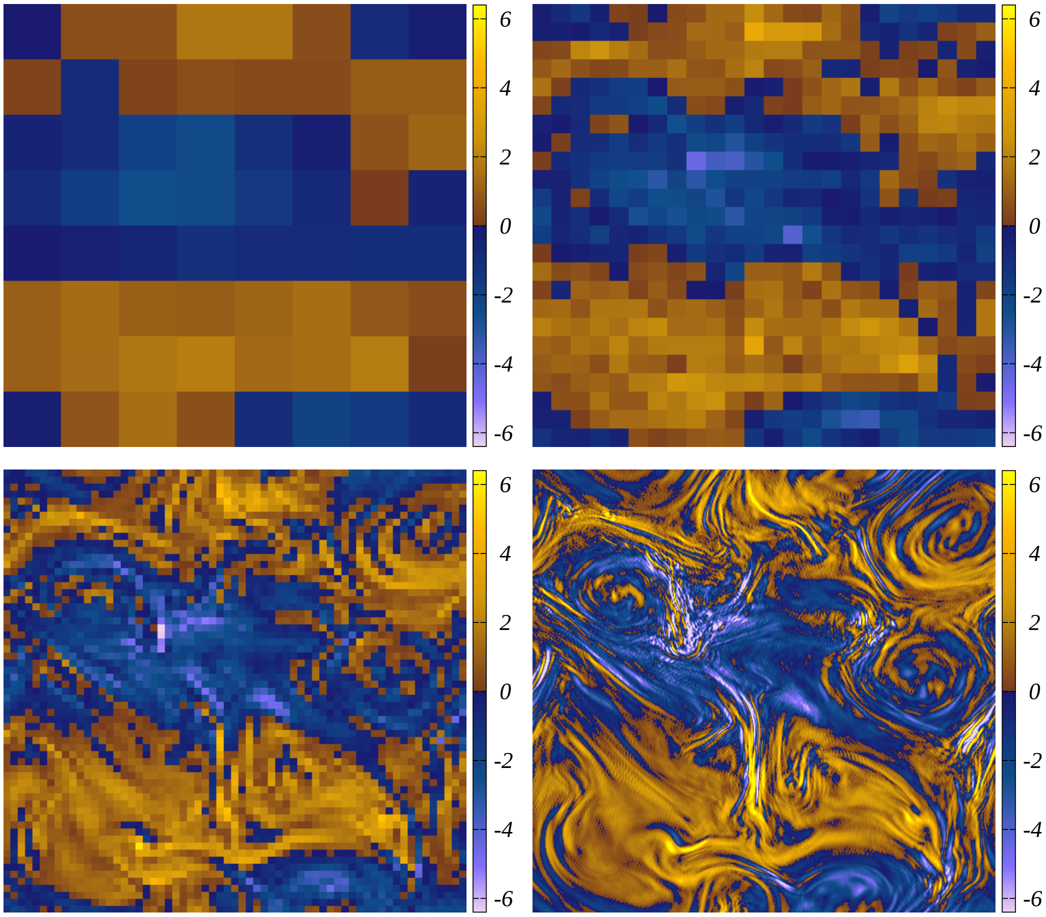

Figure 3.6: The signed measure μ as estimated for j_x in the plane y-z, shown for Run 3 ($\varepsilon = 1/16$), for four different partition box sizes (top-left: $l_\perp = 0.12$; top-right:$l_\perp = 0.04$; bottom-left: $l_\perp = 0.016$; bottom-rigth: $l_\perp = 0.002$.

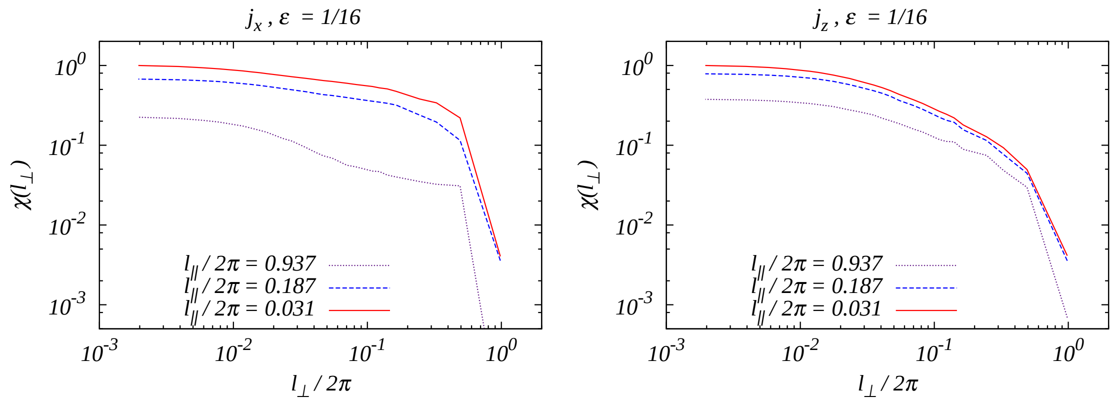

Figure 3.7: The partition function $\chi(l_\perp)$ versus the scale parameter $l_\perp$. The examples given here refer to the current perpendicular component j_x (left panel) and parallel component j_z (right panel), for $\varepsilon = 1/16$.

tested the results for different parallel scales, and no significant difference was observed. Figure 3.8 shows two examples of the variation with ε of

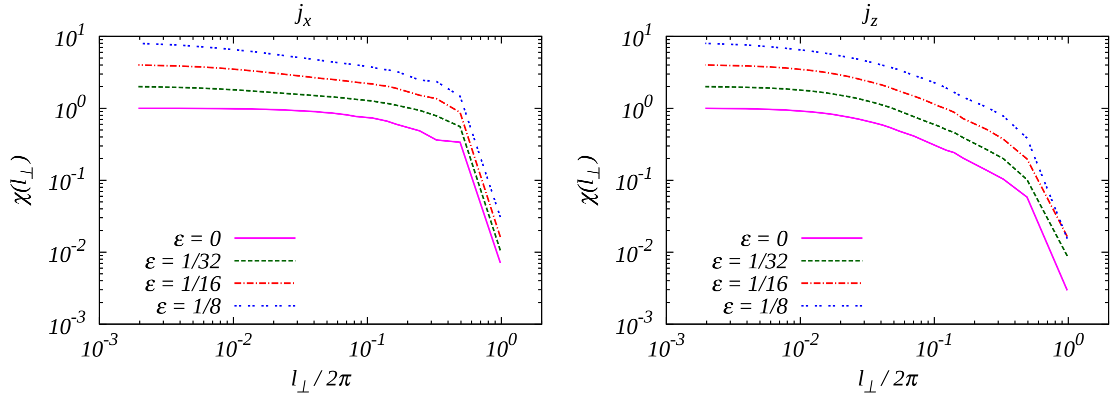

Figure 3.8: The partition function $\chi(l_\perp)$ for the current perpendicular component j_x (left panel) and parallel component j_z (right panel), for the four values of the Hall parameter ε (see legend), at $l_\|/2\pi = 0.03$. The curves have been arbitrarily shifted for clarity.

the partition functions of the current, for a fixed value of $l_\| = 0.03$. For the perpendicular component of the current j_x (left panel), the change of the scaling properties with the Hall parameter is evident. On the other hand, the changes are more subtle for the parallel current j_z. When appropriate, power law fits of the partition functions $\chi(l_\perp) = Al_\perp^{-\kappa}$ have been performed through a least square method. Two examples of fit are displayed in Figure 3.9. For a visual test, the partition functions have been compensated by dividing them by the fitted power law $l_\perp^{-\kappa}$, as plotted in the bottom panels of the Figure. In this representation, power law scaling ranges are seen as flat regions of the compensated plots. Compensated plots and fitting power laws have been represented as full lines for the Hall range, and with double-dahsed lines for the MHD range.

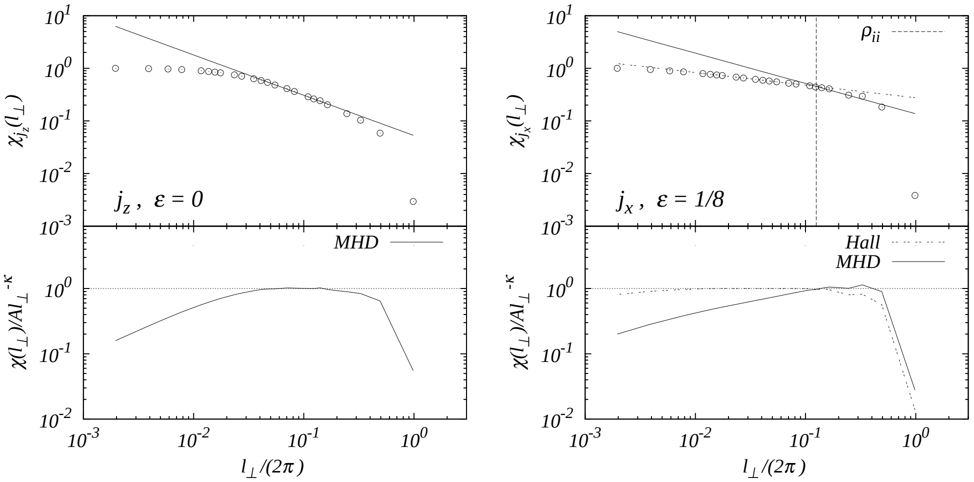

Figure 3.9: Examples of fit of the partition function, shown here at $\varepsilon = 0$ for j_z (left panel) and at $\varepsilon = 1/8$ for j_x (right panel). The power law fits $\chi(l_\perp) = A(l_\perp/2\pi)^{-\kappa}$ are superimposed (one in the left panel, two in the right panel). The ion skin depth is indicated as dashed line in the right panel. The bottom part of both right plot shows the compensated partition functions $\chi(l_\perp)/A(l_\perp/2\pi)^{-\kappa}$.

As mentioned in previous Section, values of the cancellation exponents provide information on the spatial structure of the fields. In order to discuss more easily the analysis results, cancellation exponents have been converted into the typical fractal dimension of the structures, as $D = 3 - 2\kappa$. Values of D are then displayed in Figure 3.10 as a function of ε, for the three components of the current (panels a and c) and of the vorticity (panels b and d), so that the influence of increasing Hall effect on the scaling can be evaluated. In the following, we will use the notation $D_\perp^{(f)}$ for fractal dimension estimated for the perpendicular partition function $\chi(l_\perp)$, and $D_\parallel^{(f)}$ for the parallel partition function $\chi(l_\parallel)$, where $f = j, \omega$ indicates the field under study. When the superscript $^{(f)}$ is omitted, we are indicating both fields. It is also possible to introduce a parameter for estimating the "global" fractal dimension of the fields, by averaging the three values $D_i^{(f)}$ of the fractal dimension obtained for the i-th component of each field f, $D_\perp^{\star(f)} = (D_x^{(f)} + D_y^{(f)} + D_z^{(f)})/3$ (we have temporarily suppressed the subscript $\perp$ in this formula, to semplify the notation). We remind the reader that, in the RHMHD configuration, most of the nonlinear structures are generated in the plane perpendicular to B_0. Therefore, the parallel component of the current j_z and vorticity ω_z, which depend on the perpendicular components of the magnetic and velocity fields, are of particular interest. The perpendicular components j_x, j_y, ω_x, ω_y, on the contrary, include both the perpendicular and parallel components of magnetic and velocity fields. This results in mixing the turbulent perpendicular dynamics with the quasi-linear parallel dynamics, so that results are not easily interpreted.

In the MHD inertial range, marked as "MHD" in the Figures, the estimated fractal dimension for the parallel component of the current is almost constant, showing a weak decrease from $D_\perp^{(j)} = 1.5$ in the MHD regime to $D_\perp^{(j)} = 1.4$ in the Hall regime (red plot in Figure 3.10, panel a). Similar values, but with opposite weak trend, are observed for the vorticity ω_z (panel b). Such values of D are representative of severely disrupted, almost filamented current sheets. The relative independence of $D_\perp^{(j)}$ on the Hall parameter for the parallel components of vorticity and current is consistent with the fact that, in the MHD inertial range, the Hall term is not expected to play a relevant role, since it should only be effective at smaller scales.

For the current perpendicular components (green and blue plots in Figure 3.10, panel a), $D_\perp^{(j)}$ starts around 2 (indicating current sheets) with no Hall effect. As the Hall term is turned on, the dimension first weakly increases to about $D_\perp^{(j)} \simeq 2.2$, and then steadily decreases back to $D_\perp^{(j)} \simeq 2$, showing that structures are restoring their complexity. This suggests that inertial range fields are reacting to the onset of the Hall effect, probably in response to the inertial range modification. For the vorticity components perpendicular to B_0 (green and blue plots in Figure 3.10, panel b), the effect of the Hall term is even more evident, causing a decrease of the dimesion from $D_\perp^{(\omega)} \simeq 2.3$ to $D_\perp^{(\omega)} \simeq 1.5$, indicating fragmentation of the vorticity

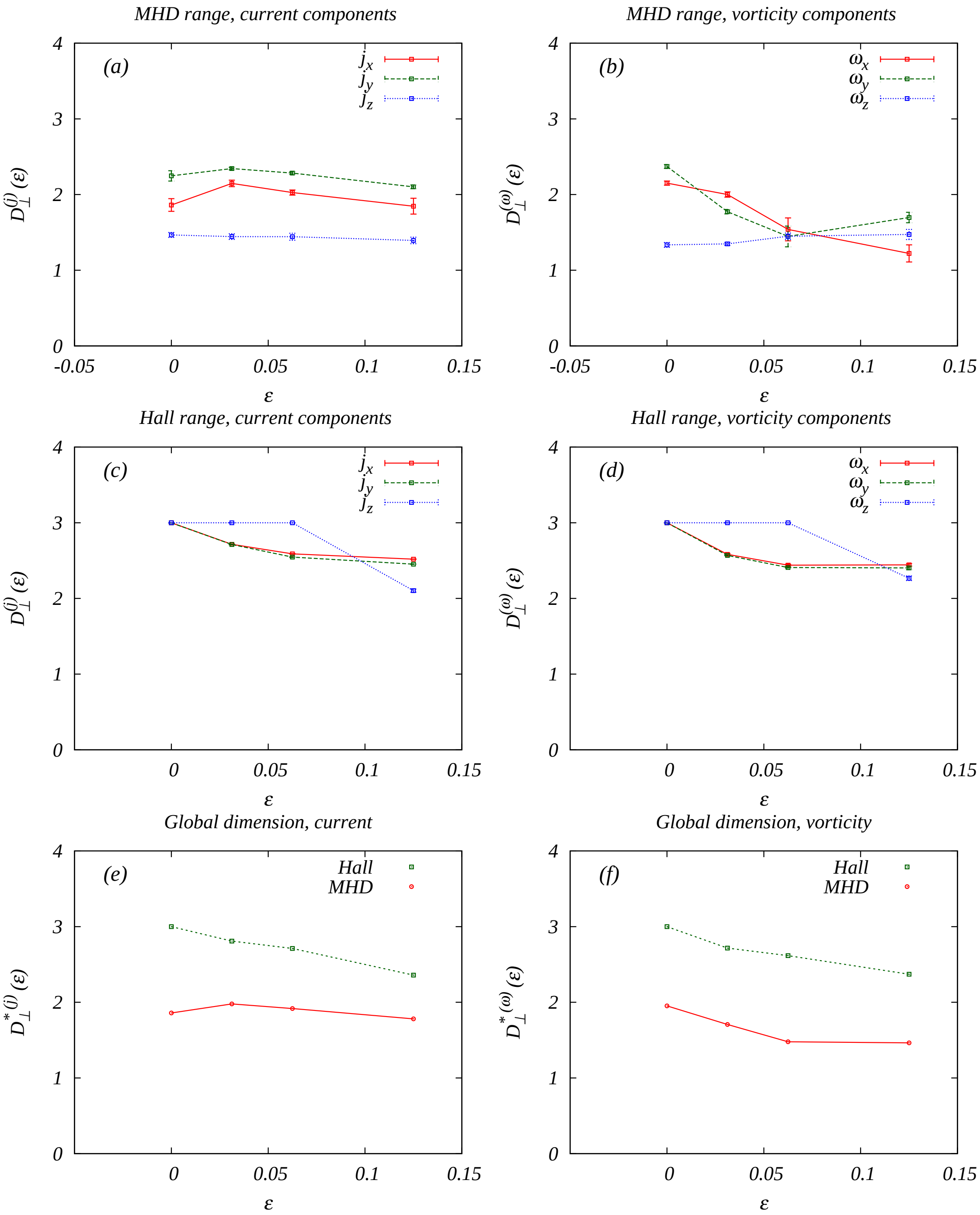

Figure 3.10: The fractal dimension $D_\perp$ estimated through equation 2.4, for the three components of current (a for the MHD range, c for the Hall range) and vorticity (b for the MHD range, d for the Hall range), labeled with different colors and line style (see inset). The indicators $D_\perp^\star$ (see text) are also plotted for the two fields (panels e and f, black lines).

sheets. The "global" fractal dimensions $D_\perp^\star$ are shown in Figure 3.10, panel e (for the current) and panel f (for the vorticity), for both the MHD and Hall ranges. For the current in the MHD range, the structures fractal dimension is roughly constant for all values of the Hall effect. Vorticity, on the contrary, shows a more evident decrease of the "global" fractal dimension with ε, from $D_\perp^{\star(\omega)} \simeq 2.3$ to $D_\perp^{\star(\omega)} \simeq 1.5$. This result shows that magnetic field and velocity are decoupled in the MHD range, so that the their structures have different fractal properties.

We now turn our attention to the range of scales smaller than the ion skin depth, where the Hall term becomes relevant when ε becomes larger. Results here are very similar for both current and vorticity, suggesting that velocity and magnetic fields decouple only in the MHD range. If no Hall cascade is present ($\varepsilon = 0$), the small scale range is characterized by smooth fluctuations (for which we assume $D_\perp = 3$) for all components of the fields, as expected when dissipation is active and numerically well resolved. This is reflected in the absence of power law, or sign singularity, in the transition from the MHD range toward the constant partition function value for smooth fields ($\chi = 1 \rightarrow \kappa = 0 \rightarrow D = 3$) at small scales. As the Hall effect comes into play, the perpendicular components of current and vorticity start to develop a (although poorly defined) power law range, with cancellation exponents κ increasing with ε. The scaling of the partition function indicates the presence of strongly persistent structures, in the range of scales larger than the typical dissipative scales. In terms of fractal dimension (green and blue plots in Figure 3.10, panels c and d), a decrease is observed from $D_\perp = 3$ to $D_\perp \simeq 2.4$, indicating that the smooth fields in the MHD regime (Run 1) are developing toward more complex, broken structures (Runs 2, 3 and 4). On the other hand, for the parallel component of current and vorticity the sign singularity in the Hall range is only observed at $\varepsilon = 1/8$. At this value of the Hall parameter, the field is no longer smooth (as instead happens for dissipative range), but rather shows presence of quasi two-dimensional sign persistent structures (red plots in Figure 3.10, panels c and d). At these small scales, the "global" fractal dimension calculated for the current and the vorticity steadily decreases from $D_\perp^\star = 3$ to $D_\perp^\star \simeq 2.3$ as the Hall term coefficient increases, confirming once more that the turbulent stuctures are being fragmented by the nonlinear Hall cascade.

Finally, we quickly review the results obtained for the scaling in the parallel direction. Figure 3.11 shows one example of partition functions of the current j_x as a function of the parallel scale, $\chi(l_\parallel)$, and for $l_\perp/2\pi = 0.002$.

As evident, the power law range is severely reduced because of the lower

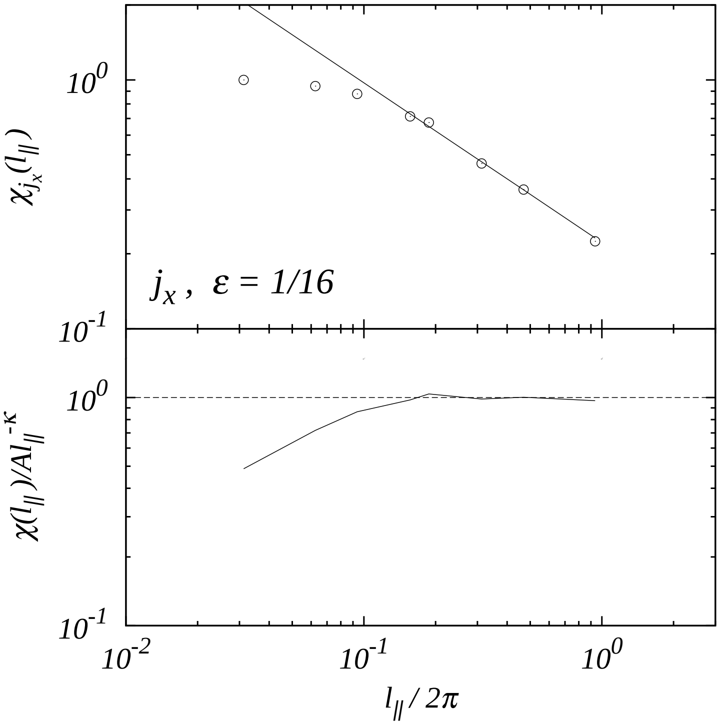

Figure 3.11: The partition function $\chi(l_\|)$, for j_x at $\varepsilon = 1/16$, and for $l_\perp/2\pi = 0.002$. A power law fit is superimposed. The bottom part of the plot shows the compensated partition function $\chi(l_\|)/A(l_\|/2\pi)^{-\kappa}$.

resolution of the numerical simulations in that direction. However, we have fitted the partition functions with the usual power law, obtaining the cancellation exponents κ and, therefore, the fractal dimensions D. These are shown in Figure 3.12 as a function of the Hall parameter. As expected from the RHMHD model, for both fields the component parallel to the magnetic field has almost constant $D_\| \simeq 2.2$ (see the red plots in panels a and b of Figure 3.12). On the contrary, for the two components on the perpendicular plane, $D_\|$ increases with ε from very small values ($D_\| \simeq 0.8$) to about $D_\| \simeq 1.9$ (green and blue plots in panels a and b of Figure 3.12), similarly to what is observed for the perpendicular partition functions. The "global" fractal dimension increases from $D^\star_\| = 1.3$ to $D^\star_\| = 2$.

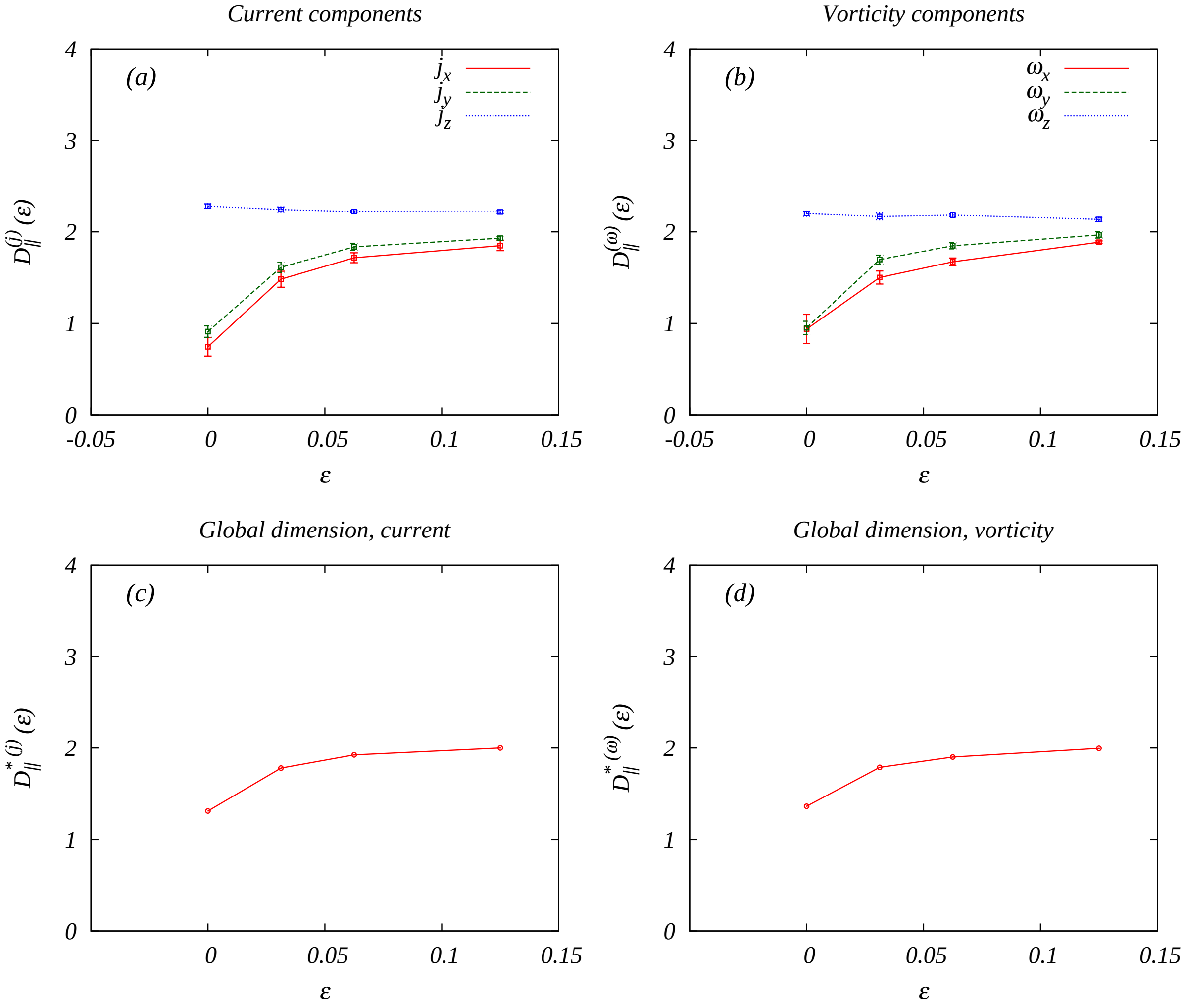

Figure 3.12: The fractal dimension D of the parallel partition function, for the three components of current (left panels) and vorticity (right panels). The overall indicators $D_\parallel^\star$ are also plotted for the two fields (bottom panels).

3.2 Conclusions

In this Chapter, a set of simulations of a RHMHD flow realized with different values of the Hall parameter ϵ, was analyzed by using the sing-singular measure. Scaling of the partition function was observed in two distinct ranges of scales, corresponding to the MHD and Hall MHD ranges. This is interpreted as the presence of an active nonlinear turbulent cascade generating structures (i.e. parts of the fields with persistent sign) on all scales. The cancellation exponents, mesaured by fitting the partition functions with power laws, indicate the degree of cancellation occurring between structures of opposite sign, and are related to the gross fractal dimension of the typical turbulent structures in the flow. In the MHD range, current structures are only weakly sensitive to the Hall effect, showing slightly decreasing fractal dimension in particular in the perpendicular current components. The vorticity structures have a more evident fragmentation, suggesting that velocity and magnetic field may have decoupled dynamics in this range. In the Hall range, current and vorticity have similar behaviour, showing increasingly unraveled structures. The nonlinear Hall term is thus responsible for disruption and unraveling of the MHD current sheets, and for the generation of smaller scale structures.

The results obtained here, together with previous analysis [79, 89], provide a comprehensive approach that help answering the basic question: do the current sheets get wider or narrower with the Hall effect? We can conclude that the Hall term has dual effects on the current sheets at different scales. On one hand, it increases the “macroscale” of the sheets by proportionally increasing their characteristic size. On the other hand, it causes these structures to unravel, which corresponds to generating microstructures on smaller scales. The decrease of the fractal dimension is a manifestation of the emerging microscales, while the widening of the macroscale of the sheet produces an increase of the filling factor of these microstructures, and the subsequent reduction of the observed intermittency [89].

These results may settle both the numerical and observational debate about the widening *vs* narrowing of the current sheets, which was probably due the extremely complex nature of the structures. Therefore, more comprehensive analysis, based on multiple approach to the same set of data (global magnitudes, characteristic times, energy cascade, intermittency, geometrical and fractal properties) is desirable in order to fully understand the effect of the Hall term on the flow dynamics, and in particular on the fractal characteristics of the current sheets. This work, along with Refs. [79, 89], may be an example of such comprehensive approach.

Chapter 4

Topological properties in hybrid Vlasov-Maxwell system

4.1 Two-dimensional hybrid Vlasov-Maxwell system

4.1.1 Equations and numerical simulation

The MHD and Hall-MHD approximations allow the study of plasma dynamics, and in particular of turbulence, only when phenomena occurring at low frequency and large scale (with respect to the appropriate plasma proper scales) are concerned. However, many interesting phenomena, including dissipative and dispersive processes, involve particles interaction and particle-wave resonances. For those processes, it is necessary to use a more detailed approach, able to capture the fast, small scale dynamics of plasmas. The Vlasov-Maxwell system is able to describe collisionless plasma dynamics, capturing most of the kinetic processes characterizing the small scale dynamics.

In this work we will make use of the results of a numerical simulation [96] that solves the dimensionless hybrid Vlasov-Maxwell equations:

$$\frac{\partial f}{\partial t} + \boldsymbol{\nabla} \cdot (\boldsymbol{v} f) + \boldsymbol{\nabla}_v \cdot [(\boldsymbol{E} + \boldsymbol{v} \times \boldsymbol{B}) f] = 0 \ ,$$

$$\frac{\partial \boldsymbol{B}}{\partial t} = -\boldsymbol{\nabla} \times \boldsymbol{E} \ ,$$

$$\boldsymbol{E} = -\boldsymbol{u} \times \boldsymbol{B} + \frac{\boldsymbol{j} \times \boldsymbol{B}}{n} - \frac{\boldsymbol{\nabla} P_e}{n} + \eta \boldsymbol{j} \ .$$

The ion distribution function is $f(\boldsymbol{x}, \boldsymbol{v}) \equiv f(x, y, v_x, v_y, v_z)$, $\boldsymbol{E}$ is the electric field, $\boldsymbol{B} = \boldsymbol{b} + B_0 \hat{\boldsymbol{e}}_z$ is the total magnetic field and $\boldsymbol{j} = \boldsymbol{\nabla} \times \boldsymbol{b}$ is the total current density. The ion bulk velocity $\boldsymbol{v}$ and density n are obtained as the moments of the velocity distribution function of f. The pressure is assumed to be isothermal. To ensure high Reynolds numbers the resistivity is fixed to $\eta \sim 10^{-2}$ for all Runs of the simulation. In the initial condition, the Maxwellian plasma is perturbed by a spectrum of Fourier modes. Energy is injected, with random phases, in the range $2 \leq m \leq 6$ where $m = (L/2\pi)k$ and $L = 20 \times 2\pi \times \rho_{ii}$. Periodic boundary conditions are imposed and the spatial resolution is 512^2 grid points. The ion plasma β is $\beta = v_{ti}^2/V_A^2$. Six values of the ion plasma β parameter were considered, $\beta = 0.25,\ 0.5,\ 1.0,\ 1.5,\ 2.0,\ 5.0$. Data from simulations with such values of β will be labeled Run 1, 2, 3, 4, 5 and 6, respectively.

Figures 4.2, 4.3 and 4.4 show some examples of the total current density components. The left panels show the components j_x while the right panels the components j_z for all six Runs taken at the time at which the turbulent activity is maximum, $t = 50\Omega_{ci}^{-1}$ [98]. In these Figures one can see that the turbulence arises through the appearance of coherent structures, resulting in a sea of vortices, islands and current sheets. In between islands, j_z becomes very intense, this being the typical signature of the intermittent nature of the magnetic field [96, 99]. From a qualitative analysis, the size of these current sheets is of the order of a few ρ_{ii}. Figure 4.1 shows the total energy spectrum $E(k)$, integrated on of radius k. The ion skin depth wave number is indicated. The large scale part of the spectrum is compatible with the typical Kolmogorov scaling $k^{-5/3}$. The Alfvénic correlation between the magnetic and the velocity field, typical of magnetohydrodynamic turbulence, is broken at $k\rho_{ii} \sim 1$ [100, 101]. Same result is obtained for all Runs (not shown).

4.1.2 Cancellation analysis

The simulations described in previous Section revealed the presence of coherent structures in the flow. This suggests that cancellation analysis can be used in order to quantitatively characterize the structures and their temporal evolution. Moreover, the parametric dependence on the plasma β can be described quantiativeley, providing insights on the dynamical processes occurring in Vlasov plasmas.

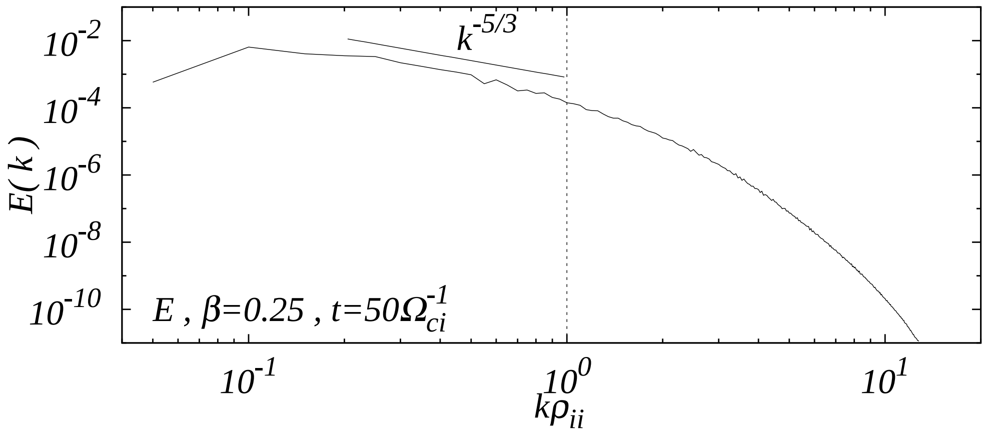

Figure 4.1: The total energy spectrum of the Vlasov-Maxwell numerical simulation for one snapshot at $t = 50\Omega_{ci}^{-1}$. The Kolmogorov expectation $k^{-5/3}$ (gray dot-dashed) is reported as a reference, while the vertical dashed line represents the ion skin depth wave number.

For our analysis we have considered, for each of the six different β values Runs, 50 time snapshots of dimensionless hybrid Vlasov-Maxwell equations. The fields analyzed here are the three components of the total current density **j** already shown in Figures 4.2, 4.3 and 4.4. To estimate the partition functions, we divided the simulation domain of size $L^2 = (20 \times 2\pi \times \rho_{ii})^2$ in boxes of variable size $l_x \times l_y$, with $l_x = l_y = l$.

Figures 4.5, 4.6, 4.7 and 4.8 shows the signed measure maps for two values of β, and for four different partition box sizes. It is evident that the coarse graining of the set partition leads to cancellations at larger scales, so that small scale structures (the current filaments clearly evident at small scale) gradually disappear. Similar behavior is seen for all fields components, and for any value of the plasma β parameter (not shown). Note, that at $t = 50\Omega_{ci}^{-1}$ the turbulence is manifested by the presence of filaments of current (Figure 4.5-4.7, right panels), while at shorter times ($t = 10\Omega_{ci}^{-1}$) the turbulence is not yet active (current filaments are absent, see left panels). From the signed measures, partition functions (eq. 2.2) have been computed for all components of the current **j** as a function of the scale parameter l.

Figures 4.9 and 4.10 show examples of the partition functions of the per-

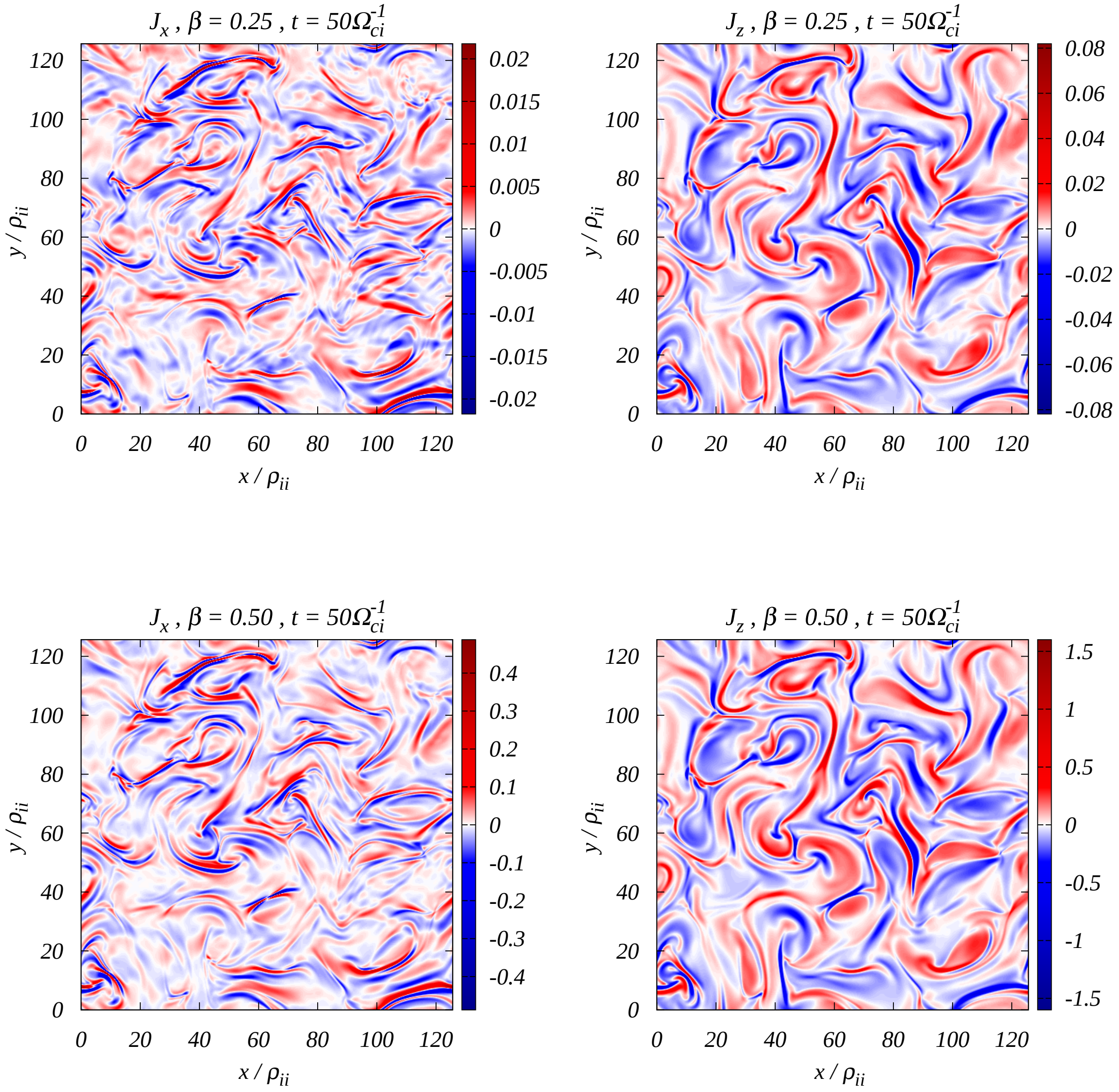

Figure 4.2: Left panels: perpendicular current component j_x in the perpendicular plane x-y, for the snapshots and for $\beta = 0.25$ (top), $\beta = 0.50$ (bottom). Right panels: parallel current component j_z in the perpendicular plane x-y.

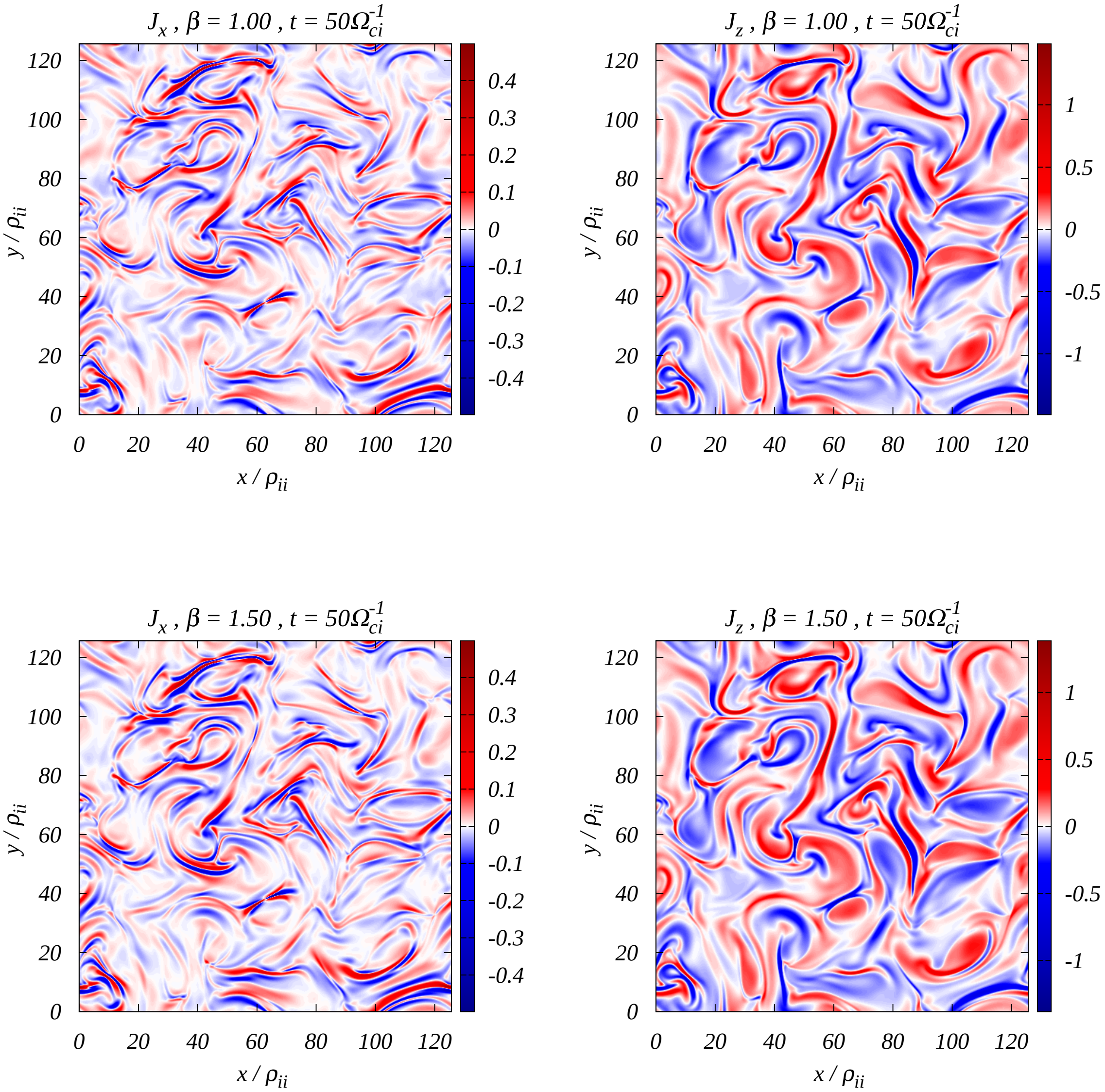

Figure 4.3: Left panels: perpendicular current component j_x in the perpendicular plane x-y, for the snapshots and for $\beta = 1.00$ (top), $\beta = 1.50$ (bottom). Right panels: parallel current component j_z in the perpendicular plane x-y.

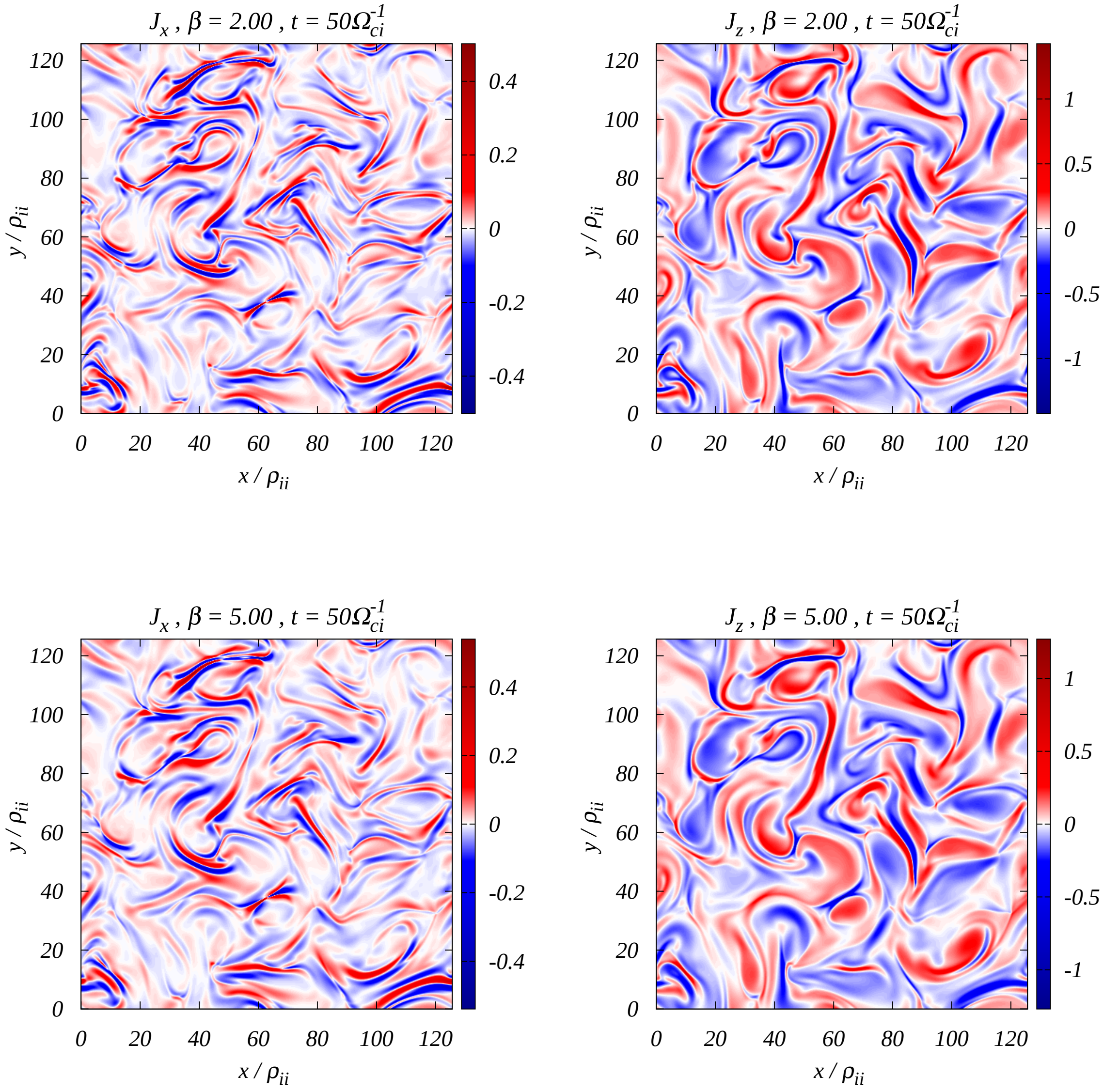

Figure 4.4: Left panels: perpendicular current component j_x in the perpendicular plane x-y, for the snapshots and for $\beta = 2.00$ (top), $\beta = 5.00$ (bottom). Right panels: parallel current component j_z in the perpendicular plane x-y.

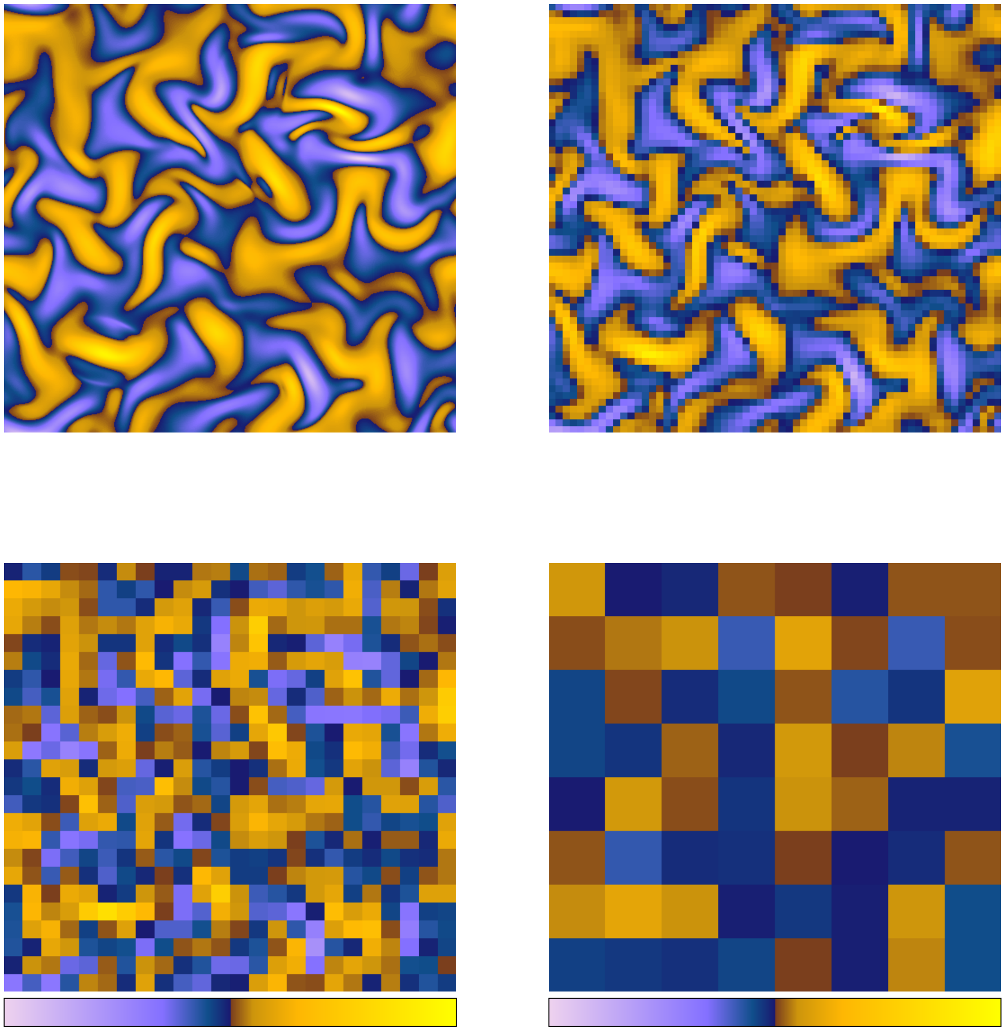

Figure 4.5: The signed measure μ as estimated for j_z in the plane x-y, for Run 1 ($\beta = 0.25$ at $t = 10\Omega_{ci}^{-1}$), for four different partition box sizes (from top to bottom, $l/\rho_{ii} = 0.039$, 0.312, 0.820 and 2.461). The color scale is arbitrary.

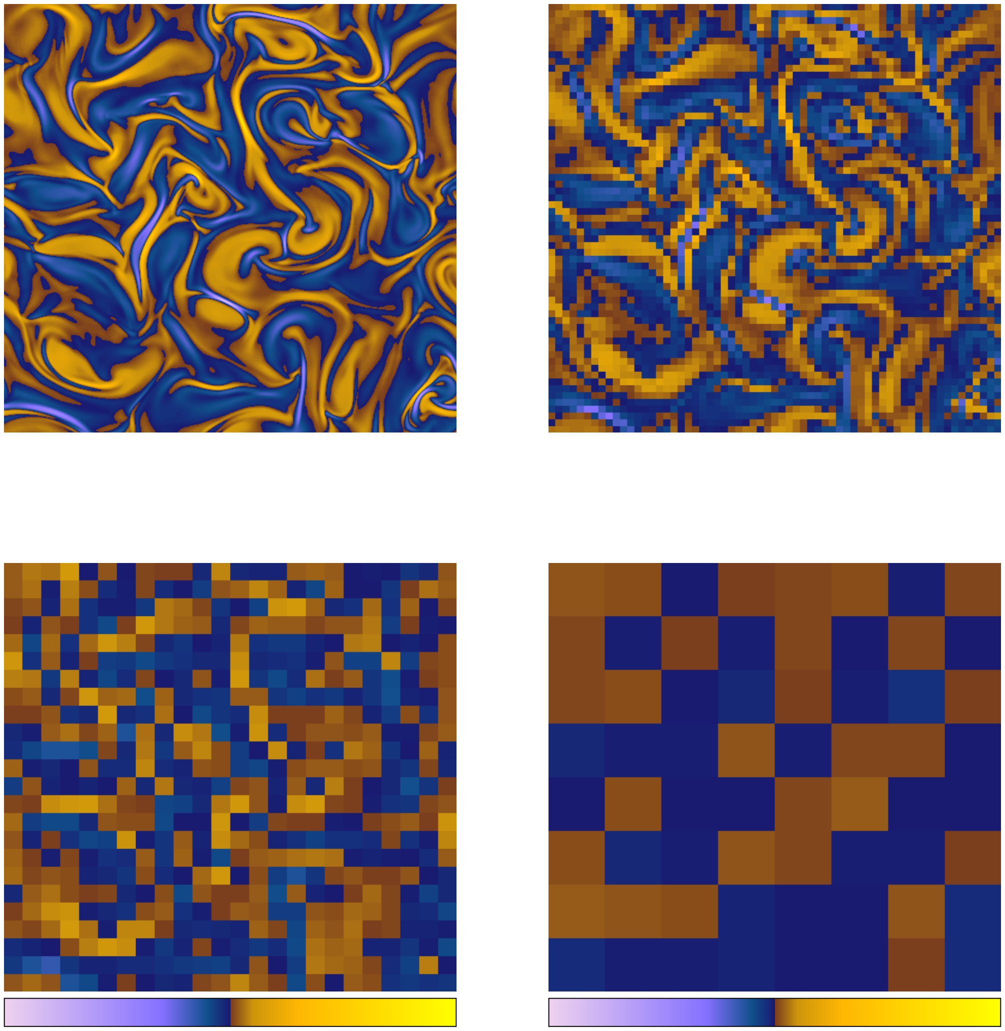

Figure 4.6: The signed measure μ as estimated for j_z in the plane x-y, for Run 1 ($\beta = 0.25$ at $t = 50\Omega_{ci}^{-1}$), for four different partition box sizes (from top to bottom, $l/\rho_{ii} = 0.039$, 0.312, 0.820 and 2.461). The color scale is arbitrary.

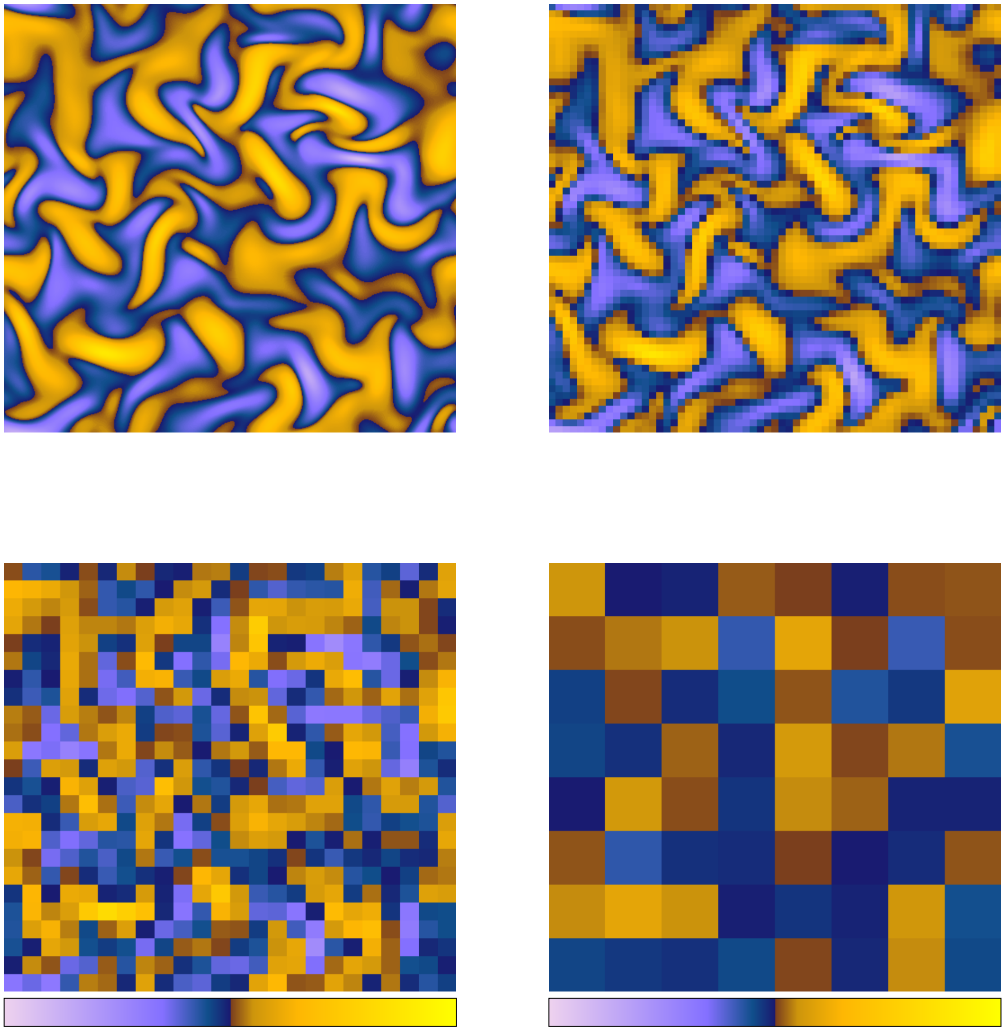

Figure 4.7: The signed measure μ as estimated for j_z in the plane x-y, for Run 6 ($\beta = 5.00$ at $t = 10\Omega_{ci}^{-1}$), for four different partition box sizes (from top to bottom, l/ρ_{ii} = 0.039, 0.312, 0.820 and 2.461). The color scale is arbitrary.

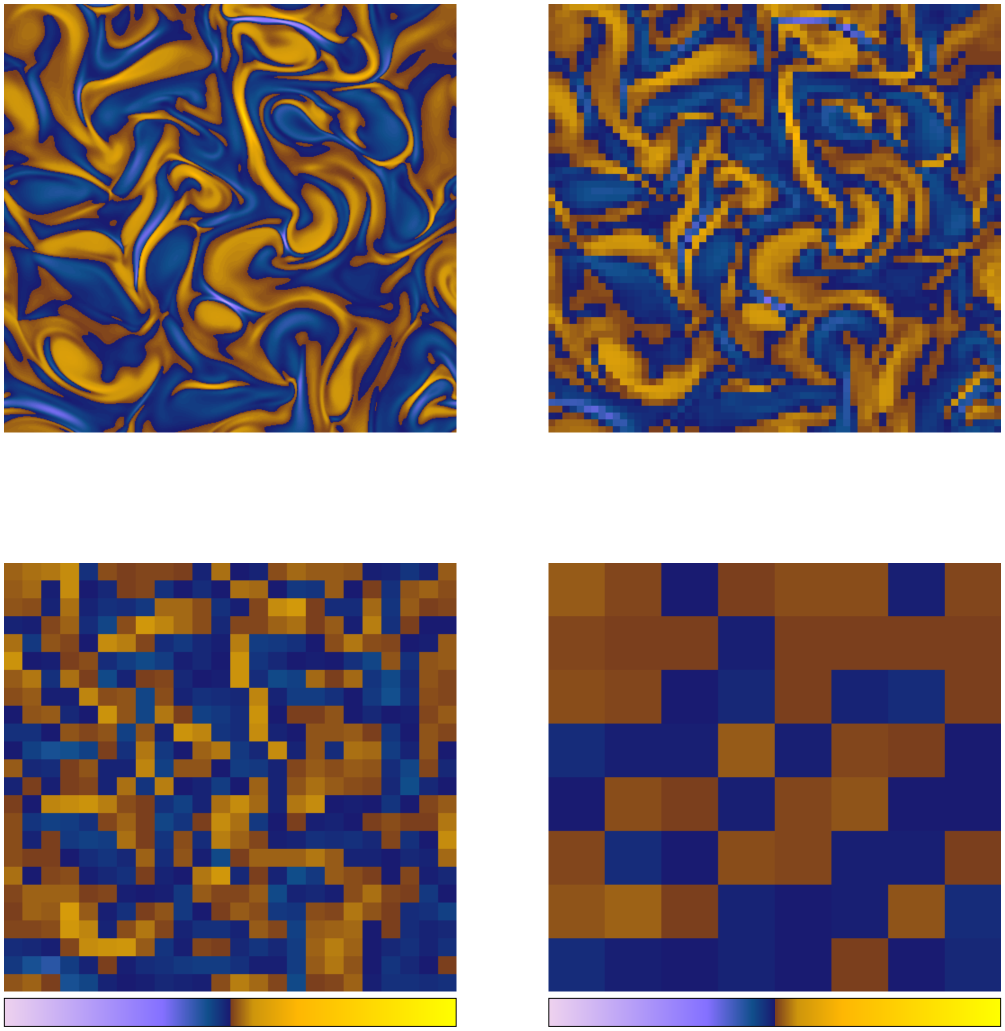

Figure 4.8: The signed measure μ as estimated for j_z in the plane x-y, for Run 6 ($\beta = 5.00$ at $t = 50\Omega_{ci}^{-1}$), for four different partition box sizes (from top to bottom, $l/\rho_{ii} = 0.039$, 0.312, 0.820 and 2.461). The color scale is arbitrary.

pendicular compentent j_x and parallel j_z of the current density respectively, for two different values of β and for three different times (see each Figure). When appropriate, power law fits $\chi(l) \sim l^{-\kappa}$ have been performed through a least square method. The fitting curves are displayed in the Figures. For a visual test, the partition functions have been compensated by dividing them by the fitted power law $l^{-\kappa}$, and represented in the bottom panels of each Figure. Scaling ranges are seen as flat regions in the compensated plots. Compensated plots and fitting power laws have been represented as full lines for the fluid range, and with dahsed lines for the kinetic range.

As can be seen in all panels of Figures 4.9 and 4.10, the partition functions suggest the presence of power law scaling, and therefore sign singularity, in a range corresponding to the inertial range of the energy spectra (cf. Figure 4.1). The same results are obtained for all the Runs (not shown). This holds for all fields and β parameters, and is the signature of the MHD turbulent cascade among structures of different size [44]. A second power law range emerges at small scales. This suggests that a secondary sign singularity is present, with fragmentation of dissipative structures along the scales presumably due to the nonlinear kinetic processes. The small scale power law is observed for all the current components and in all Runs. Figures 4.11 and 4.12 show the cancellation exponents *vs* time, obtained from the small scale power law fit (red circles) and for the large scale fit (blue diamond). In green the level of turbulent activity is represented by the average out-of-plane squared current density $\langle j_z^2 \rangle$ [98]. The left panels show κ for the j_x component, while right panels the j_z component of the current density for different values of the plasma β (Run $1, 2, 3, 4, 5$ and 6 from top to bottom respectively). The first feature to be noticed for the j_x component is the widely oscillating behaviour of the cancellation exponent at the early stage of the simulation Runs, namely for $t < 17\Omega_{ci}^{-1}$, especially evident for small values of β. This oscillation is due to the unstable and sporadic character of the structures, which are not well formed yet, presumably because the dynamics is still dominated by the linear (Alfvénic) perpendicular evolution. Indeed, as pointed out in Ref. [97] by observation of the average out-of-plane squared current density $\langle j_z^2 \rangle$, turbulent cascade is not yet developed for $t < 35\Omega_{ci}^{-1}$. This means that nolinear interaction are still slowly building up structures on smaller and smaller scales. The cancellation exponents become more stable after $t = 17\omega_{ci}^{-1}$, after a sharp transition visible in the plots. This suggests that the first structures hierarchies are formed well in advance with respect to the peak of squared current density. Wether the turbulence can be considered

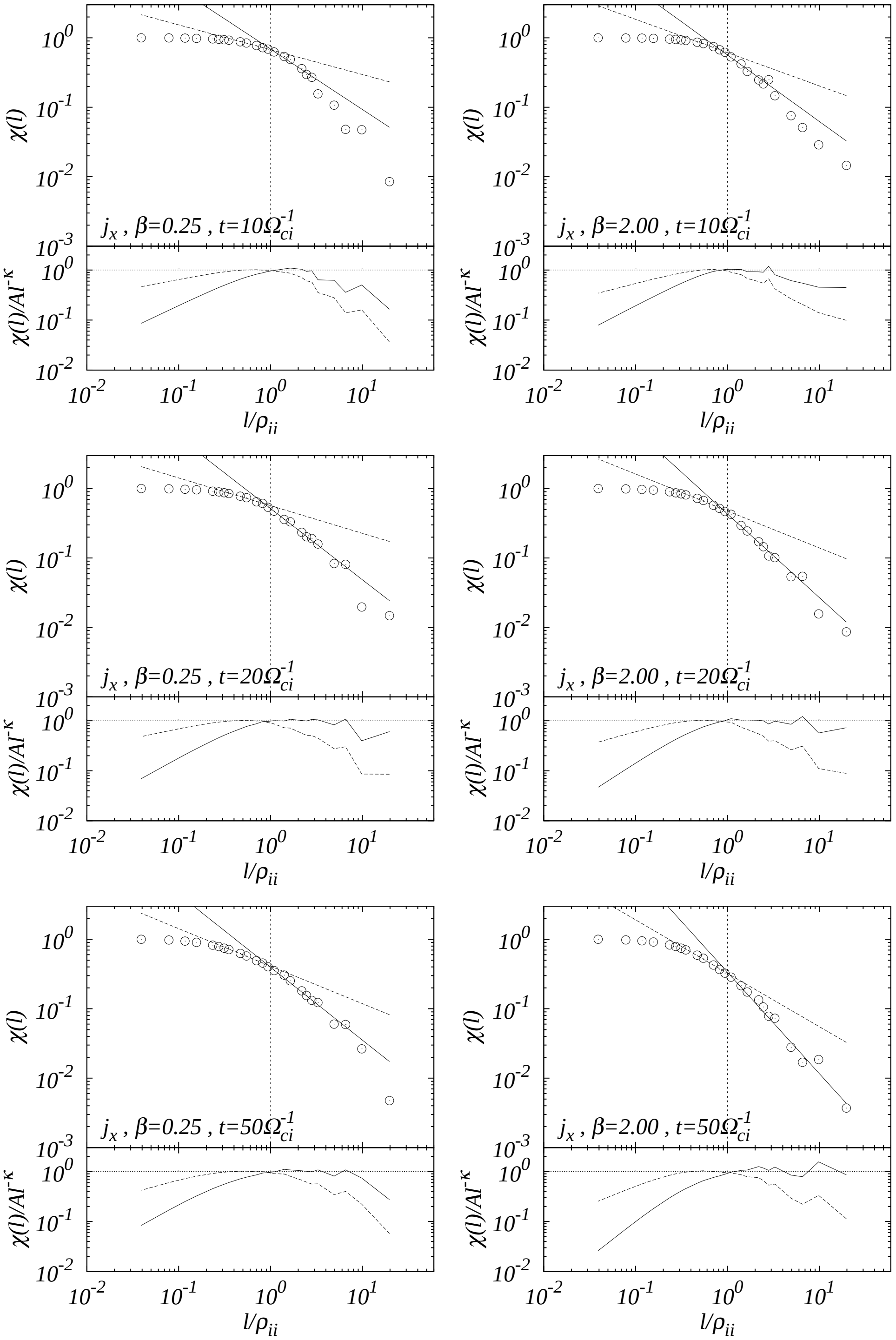

Figure 4.9: The partition function $\chi(l)$ vs. l/ρ_{ii} for component j_x of the current density for Run 1 (left panel) Run 5 (right panel), for 3 different time (see each Figure). Power law fits are superimposed. The ion skin depth is indicated (dashed line). The bottom part of each plot shows the compensated partition function $\chi(l)/A(l/\rho_{ii})^{-\kappa}$.

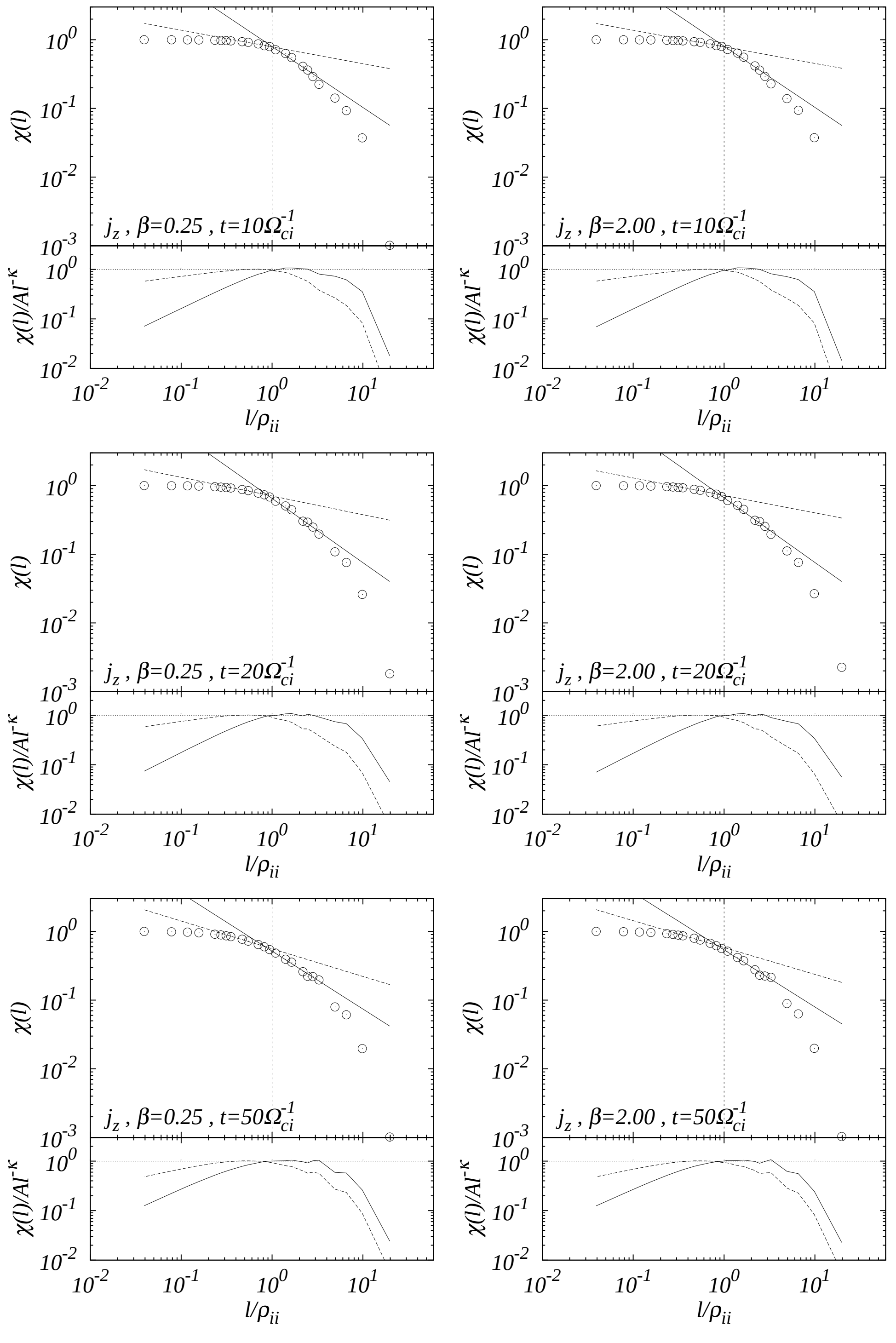

Figure 4.10: The partition function $\chi(l)$ vs. l/ρ_{ii} for component j_z of the current density for Run 1 (left panel) Run 5 (right panel), for 3 different time (see each Figure). Power law fits are superimposed. The ion skin depth is indicated (dashed line). The bottom part of each plot shows the compensated partition function $\chi(l)/A(l/\rho_{ii})^{-\kappa}$.

fully developed at $t = 17\omega_{ci}^{-1}$ or at $t = 35\omega_{ci}^{-1}$ is still not clear. However, the topology of the current field seems to reach a relative stability at early times. This process is less evident at high β, where the transition to turbulence is smoother. After turbulence is fully developed, the cancellation exponent of the j_x component increases more or less steadily for all β, the trend being less evident for larger values of the plasma parameter. This behaviour is a clear indication of the fact that the nonlinear interactions are active and create smaller and smaller structures during the whole Run, making the field complexity increase with time. In the large scale range, the cancellation exponents for the components perpendicular to the external field j_x and j_y are generally found to be $\kappa > d/2$ (we remind that in this simulation $d = 2$). This indicates the presence of sign-antipersistent structures, or alternation of positive-negative structures, as can be seen in the left panels of Fig.s 4.2-4.4 where pairs of positive and negative structures are prevalent. Cancellation exponent is therefore sensitive to the presence of pairs of structures. On the contrary, in the small scale range we found mostly $\kappa < d/2$, which indicates the presence of structures with strong sign-persistence. This occurs because the structure size is large with respect to the scale, so that structures are seen as smooth, and the structure pairs are well resolved.

For the parallel component j_z, a different behavior is observed. The snapshots prior to transition to turbulence are not characterized by unstable structures as for the perpendicular components, but instead show a steady, fast increase of κ, which indicates a regular set-up of the structures. After the onset of fully developed turbulence at $t \simeq 17\Omega_{ci}^{-1}$, the cancellation exponent saturates and then weaklydecreases for the fluid range of scale for $t > 40\Omega_{ci}^{-1}$, indicating that the structures have reached their typical shape, and their complexity does not increase with time (unlike for the perpendicular components). The values of the cancellation exponents are $\kappa \simeq 1$, indicating very irregular, nearly decorrelated fluctuations. However, small scale structures have opposite behaviour: their complexity increases with time after the transition to turbulence, as for the parallel components of the current. A saturation value $\kappa \simeq 0.4$ is reached at large times $t > 40\Omega_{ci}^{-1}$ for small values of plasma β, while the saturation value is $\kappa \simeq 0.3$ for large β. This corresponds to "fat" current filaments, characterized by a fractal dimension $D \simeq 1.2$ or $D \simeq 1.4$ at small and large β, respectively.

Figures 4.13 show the cancellation exponents, obtained for the component j_x (left panels) and j_z (right panels), *vs* plasma β for five times (different lines in the plots), and for small (top panels) and large (bottom panels) scale

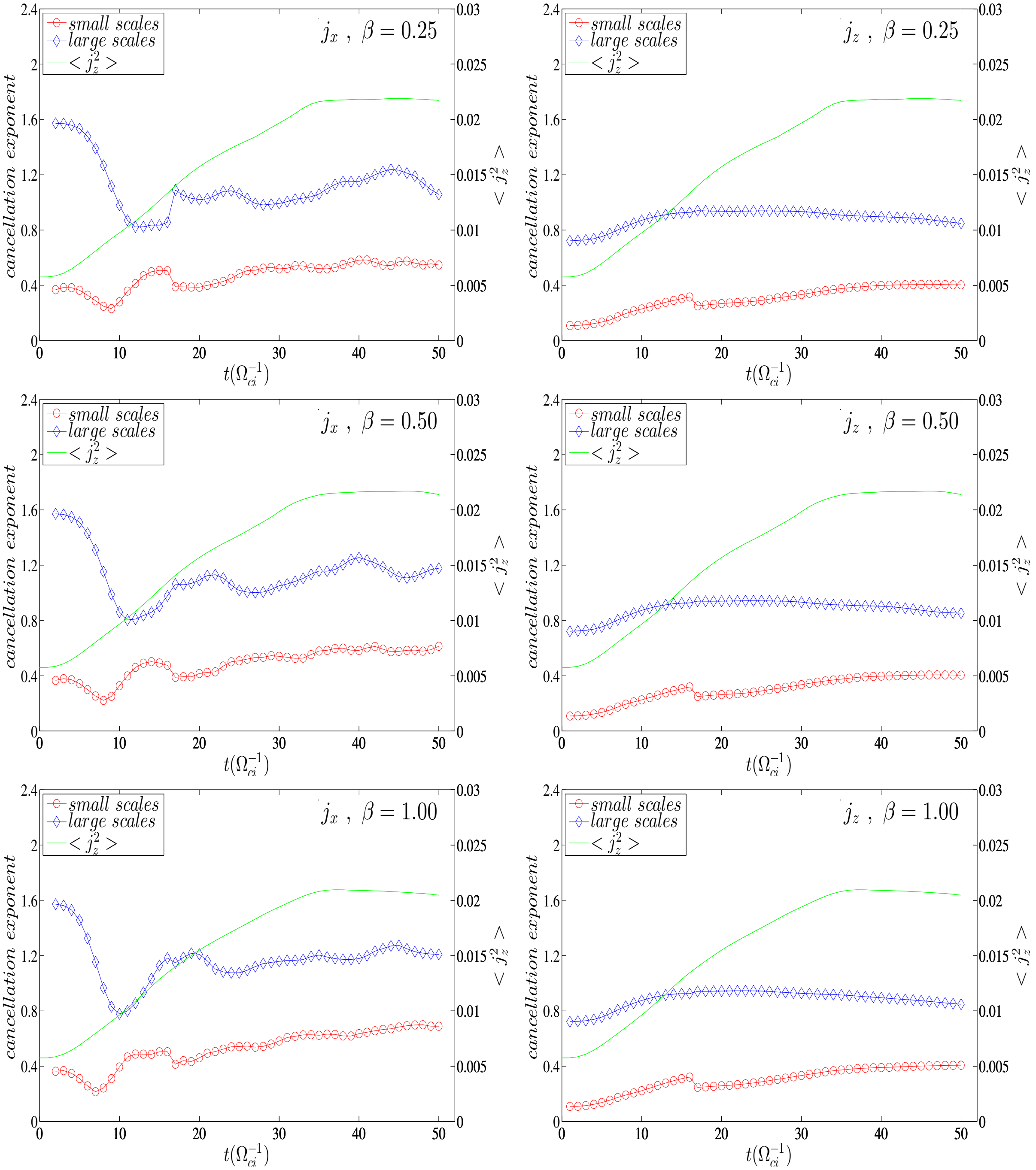

Figure 4.11: Cancellation exponent of component j_x (left panels) and components j_z (right panels) of current density *vs* time for Run $1, 2$ and 3 (from top to bottom). The red circles are the cancellation exponents compute for small scales while blue diamonds compute for large scale. In green the level of turbulent activity is represented by the average out-of-plane squared current density $\langle j_z^2 \rangle$.

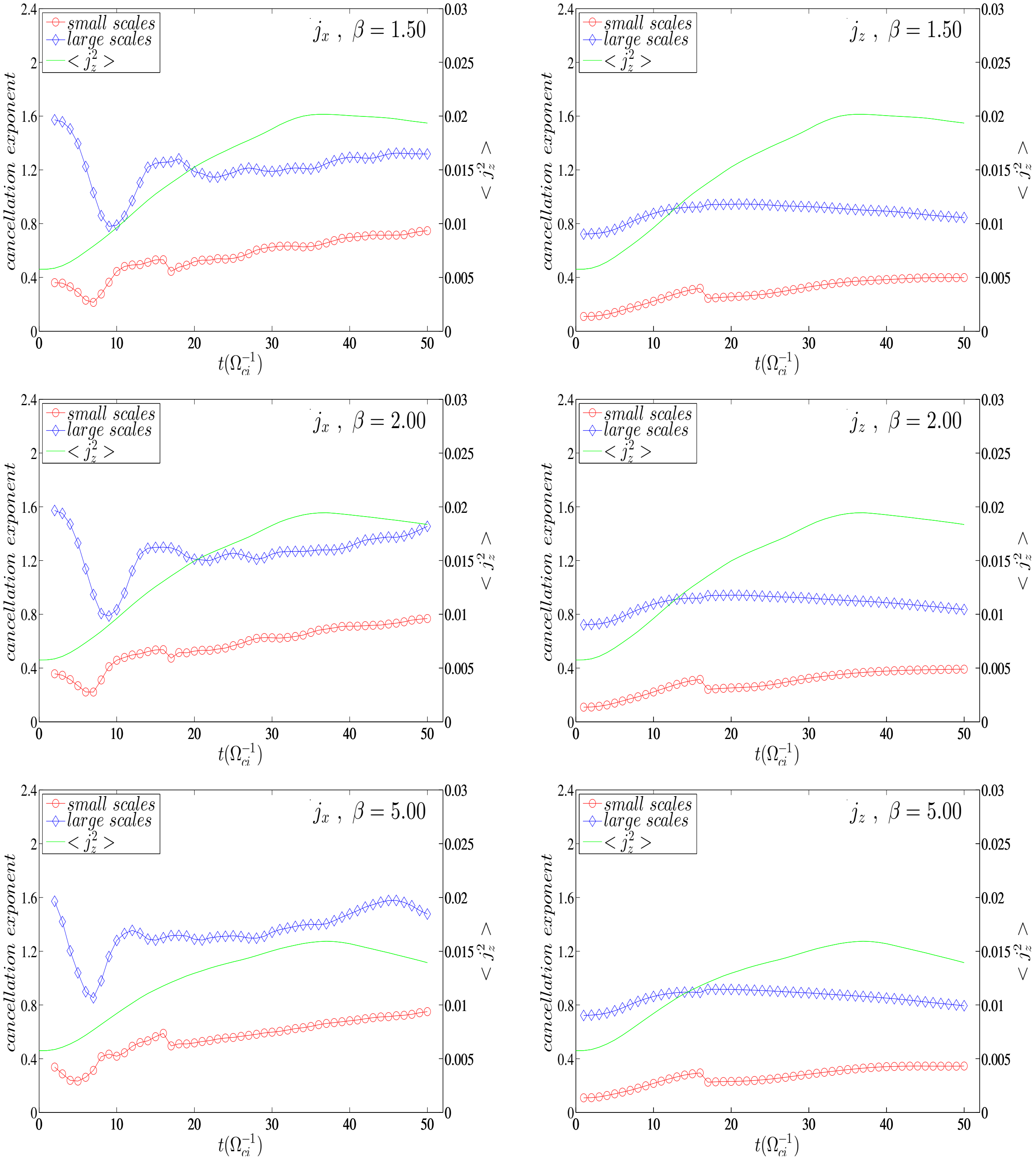

Figure 4.12: Cancellation exponent of component j_x (left panels) and components j_z (right panels) of current density *vs* time for Run $4, 5$ and 6 (from top to bottom). The red circles are the cancellation exponents compute for small scales while blue diamonds compute for large scale. In green the level of turbulent activity is represented by the average out-of-plane squared current density $\langle j_z^2 \rangle$.

ranges. The cancellation exponent of the x compenent of current density

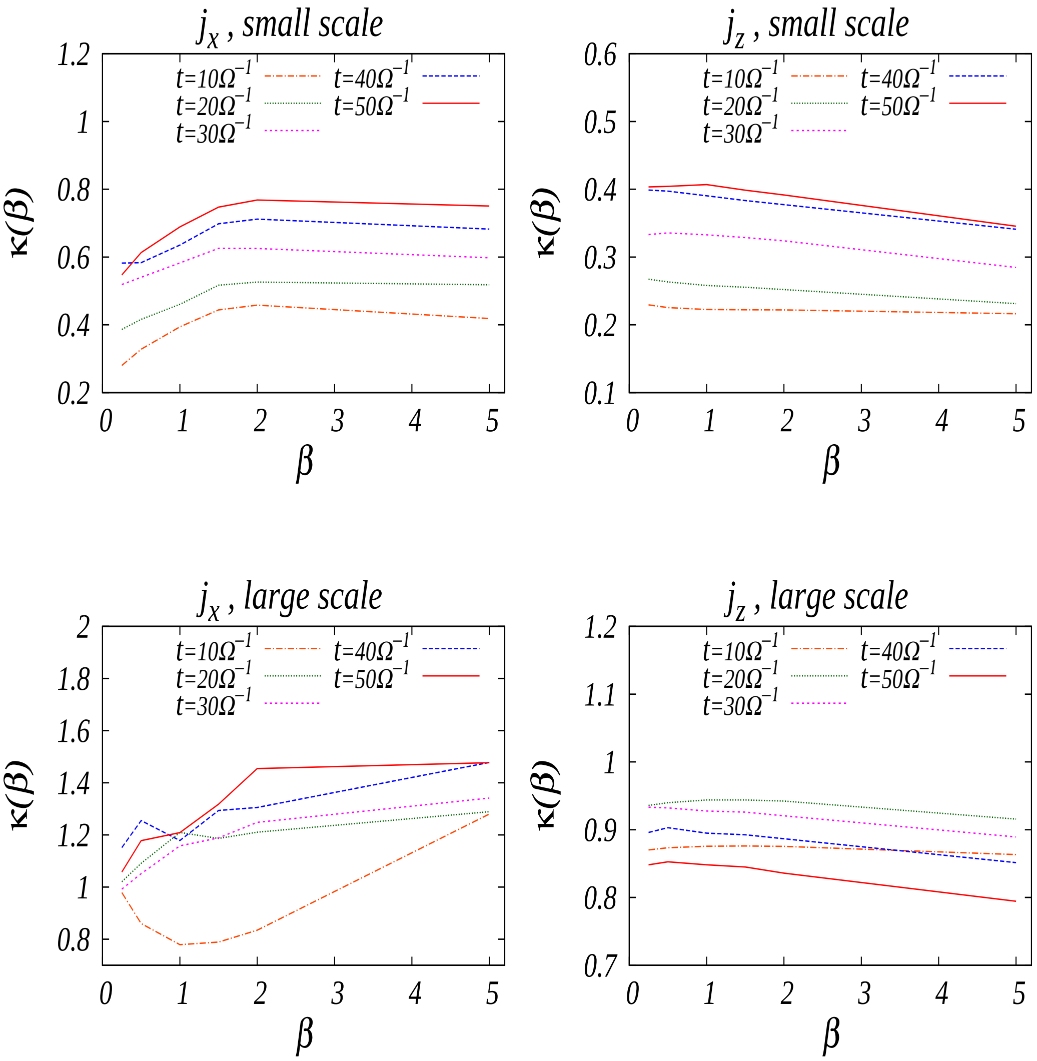

Figure 4.13: Cancellation exponent of component j_x (left panels) and components j_z (right panels) of current density *vs* beta of plasma for five time.

shows a tendency to increase for $\beta < 2$, for both large and small scale ranges. For $\beta > 2$ a saturation is observed, especially at long times. This suggests that differences in the structure complexity only occurs for β across unity, and no further complexity is introduced by incerasing the plasma β. For the z component, cancellation exponents show a weak decrease with β for all times and for both small and large scale ranges (except for the large scale case at early times, where the exponents are roughly constant). As already observed, snapshots at larger times have larger κ.

4.1.3 Conclusions

In this Chapter, a set of simulations of dimensionless hybrid Vlasov-Maxwell equations, realized for a set of different values of plasma β parameter, was analyzed by using the the sing-singular measure. The presence of power law scaling of the partition function was observed in two distinct ranges of scales, corresponding to the fluid and kinetic ranges of the plasma dynamics. This can be interpreted as the presence of an active nonlinear turbulent cascade generating structures (i.e. parts of the fields with persistent or anti-persistent sign) on all scales. The cancellation exponents, obtained from the slope of the partition functions, indicate the degree of cancellation occurring between structures of opposite sign, giving information on the complexity of the structures. This is generally related to the gross fractal dimension of the typical turbulent structures in the flow. The topological properties of the structures is different for parallel and perpendicular components of the current. For the perpendicular components, structures are strongly sign-persistent in the small scale range, and anti-persistent (alternation of positive and negative structures, occurring in closeby pairs) at larger scales.

The time evolution of the numerical simulation is well captured by the cancellation analysis. In particular, the transition to turbulence produces several effects on the different components. A sharp transition of the structure complexity is always visible in advance with respect to the time when fully developed turbulence was previously observed to set in [97]. For some current components, the cancellation exponent shows wide oscillations before turbulence sets in, describing the unstable presence of fluctuations. For other components, the structure complexity steadily builds up in this phase, as shown by the regular increase of the cancellation exponent. After the transition to turbulence, the perpendicular components continue to develop small scale complexity through nonlinear interactions, while the parallel component rapidly reaches a saturation, and often a slow decrease, of the cancellation exponent, indicating that parallel currents do not develop smaller scale structures as the time increases.

Finally, the β dependence of the field complexity was also analyzed from the different Runs. The cancellation exponent κ, for the perpendicular components, increases with β, then saturates or slowly deacreases (at small scales) or increases (at large scales), for all times (except very short times). For the parallel component, structures are strongly sign-persistent at small scales, and weakly persistent (in fact, nearly decorrelated fluctuations are observed) at large scales. Moreover, it increases with time at small scales, and decreases with time at large scales.

The application of cancellation analysis has thus provided the quantitative evaluation of the field complexity, and has shown excellent sensitivity to time evolution features and to parametric variations. Moreover, it has been able to capture the subtle difference between single-layerd and double-layered structures observed for the different current components.

Chapter 5

Cancellation analysis of magnetic activity in solar active regions

5.1 Introduction: photospheric active regions

Most solar phenomena are direct consequence of the dynamic magnetic fields, continuously emerging in the solar photosphere (the lower layer of the solar atmosphere, with depth of about 100 km) from the solar interior, and of their interaction with convectively-driven plasma flows. At photospheric level, the most evident aspect of the magnetic activity is the presence of *active regions (ARs)* (Figures 5.1), which are more or less extended and concentrated magnetic field areas. An active region often appears at photospheric level like a structure with regions of opposite polarities, including pores and sunspots if the emerging magnetic field is sufficient [104]. Sunspots are the most striking phenomenon of solar magnetism. In most cases, they have a shape circular or nearly circular shape, with typical diameters of the order of 30000 Km, temperature of about 4000 K, and size dependent lifetime of the order of weeks.

Many interesting phenomena that characterize the active regions are explosive, such as *coronal mass ejections CMEs*, accelerated particles and *flares*. The latter are spectacular phenomena in which a large amount of energy is released in a short time. These events are clearly visible in soft and hard X-ray emission, and the conversion of magnetic energy into heat effects is also visible as extreme ultra-violet (EUV) radiation. It is now evident that these phenomena have impact on Earth, in the form of geomagnetic disturbances, communication perturbations and satellite damages [103, 102].

One of the main goals in solar physics is the observations of magnetic field variations in ARs as a signature of flares. Cancellation analysis has shown promising ability in identifying subtle structural changes in active regions magnetic fields, which have been interpreted as flare precursors. In this thesis we analyze two active regions in order to better understand the relationship between magnetic structure variations and flares.

5.2 Ground based solar observations: NOAA 10019

5.2.1 Observation

In this section we want to study graund-based observation of photospheric magnetic field to characterize the topological proprerties of the current, and their relationship with flaring activity. Observations were performed between 3 July and 6 July 2002 by exploiting the spectro-polarimetric mode of the THEMIS telescope ($http://www.themis.iac.es$), using the photospheric Fe I 630.2 nm spectral line (cf. [109] for details about measurements). The observed Active Region was located around $W39 - S17$ on the first day of observation, and reached $E08 - S17$ on the last day. The region was scanned with step of $0.5''$ (the size of the spectrograph entrance slits width). Seeing conditions limited the spatial resolution to about $1''$. The spatial sampling along the slit is $0.5''$/pixel and the spectral sampling 22 $m\mathring{A}$/pixel. The size of the field covered by the magnetogram was not constant, and varied from $80'' \times 50''$ to $100'' \times 70''$. The four Stokes parameters I, V, Q, U were measured using an exposure time of 300 $m$sec for all wavelengths. The so-called 2×1 $THEMIS$ spectro-polarimetric configuration was used: the two beams with orthogonal polarization exiting the analyzer are directed into one single camera. The field of view covered by the entrance slits of the spectrograph was $1'$. Beam inversion was performed for the linear polarization Q: the top part of the camera received sequentially $I + Q$, $I - Q$, $I + U$ and $I - V$, while the bottom part recorded $I - Q$, $I + Q$, $I - U$, $I + V$. This observing strategy allows to reduce the impact of the seeing due to the time delay between to successive polarimetric measurements (1 s) [110]. The final error of the measurements is $S/I_c = 10^{-3}$, where S stands for one of the Q, U or V Stokes parameters, and I_c stands for the intensity of the continuum in quiet Sun regions. To derive the magnetic field strength, inclination and azimuth, the SIR (Stokes Inversion based on Response function) was used. A one component atmosphere was chosen with a magnetic filling factor equal to 1.

To get a quantitative measure of the scaling properties of the current density inside the active region in relation to the flaring activity, we used a time series of fifteen measurements of the vector magnetic field in $NOAA$ 10019. The time series starts on 3 July at 08:06 (in Universal Time, UT), and ends on 6 July at 11:39 UT. Dataset for each of the four days include six, three, two and four snapshots of the active region, respectively. In Figure 5.1, we display four examples of maps of vertical magnetic field B_z for the AR 10019, one for each of the four days of observation. For each magnetogram, the day,

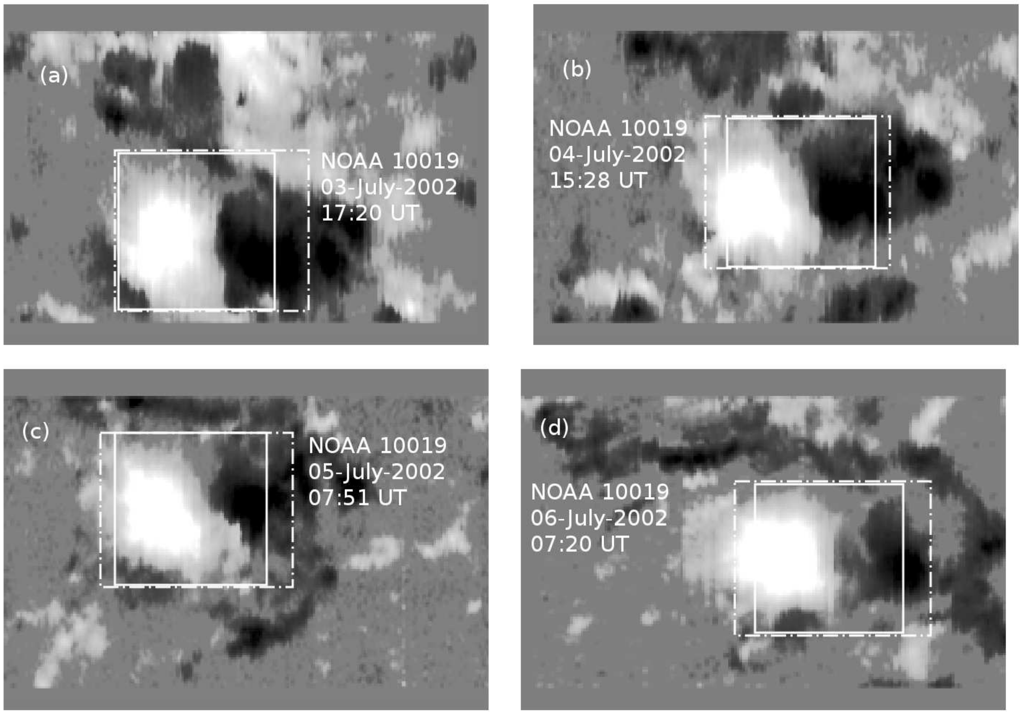

Figure 5.1: Maps of vertical magnetic field B_z for the AR 10019 as measured on 3 July (a) 4 July (b), 5 July (c), and 6 July (d) 2002. Time of each snapshot is indicated in the legend. Dot-dashed boxes indicate the box $Q_{max}(L_{max})$ of size L_{max} and the thin-line the box $Q(L)$ of size L (see text for explaination).

hour (in Universal Time) and the dimension L of the box $Q(L)$ used for the estimation of the cancellation exponents (see below) are indicated.

Finally, using the two-dimensional measurements of the photospheric vector magnetic field $\mathbf{B}(x, y)$ on the solar surface, it was possible to estimate the vertical component z of the current density $J_z(x, y) = (\nabla \times \mathbf{B})_z$, where (x, y) are the cartesian coordinates on the surface of the sun. This can be done by computing, for each pixel of area s, the line integral of the transverse (i.e. perpendicular to the line of sight) magnetic field $\mathbf{B}_\perp(x, y)$ over a closed contour G [46], $4\pi j_z/c = (\nabla \times \mathbf{B})_z = s^{-1} \oint_G \mathbf{B}_\perp \cdot d\mathbf{r}$. Integration along each side of G was performed using Simpson's rule. Figure 5.2 shows the line of sight current density for the same snapshots as in Figure 5.1.

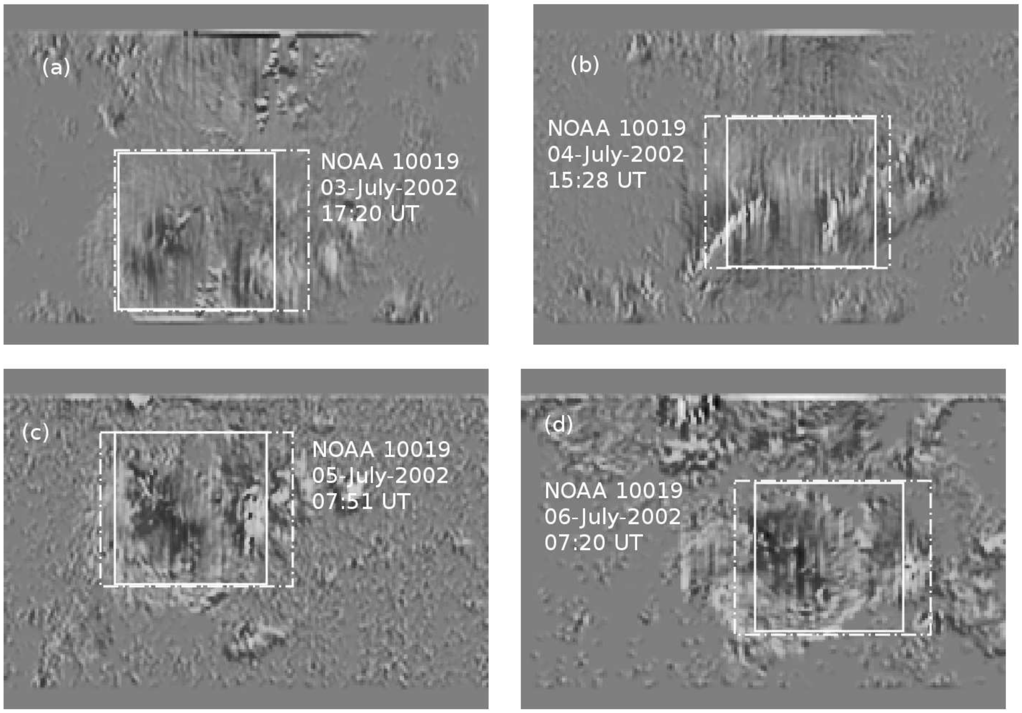

Figure 5.2: Maps of vertical component of the current density J_z for the AR 10019 as measured on 3 July (a) 4 July (b), 5 July (c), and 6 July (d) 2002. Time of each snapshot is indicated in the legend. Dot-dashed boxes indicate the box $Q_{max}(L_{max})$ of size L_{max} and the thin-line the box $Q(L)$ of size L (see text for explaination).

5.2.2 Time evolution and flaring activity

X-ray observation of the active region NOAA 10019 analyzed here shows periods of low and enhanced flaring activity. During the observations, the active region produced eight C-class flares whose list, as extracted from GOES X-ray flux database is given in Table 5.2.2. Figure 5.3 shows the X-ray flux for the flares listed in the Table (vertical bars, right vertical axis), measured in active region NOAA 10019 during the time of observation. The time axis is set so that $t = 0$ at 00:00 UT on 3 July 2002, the first day of observation. In the same plot, we display the time evolution of the fractal dimension of current structures D (symbols and dashed line, left vertical axis), as calculated from the fitting parameter κ through relation (2.4). During the first part of the observation, the fractal dimension remained roughly steady, with $D \simeq 1$, which indicates presence of current filaments. However, a sudden increase to about $D = 1.24$ is clearly present near the end of the observation, between t_1 = 08:20 UT and t_2 = 09:19 UT, both on 6 July. This increase occurs in correspondence with a large flare (C-class, with flux above $10^{-6}\ W/m^2$) recorded at t_F = 09:27 UT on the same day. This observation, similar to previous results [46, 48, 49], suggests that the magnetic field structures could be smoothed by dissipative effects which anticipate the flare explosion.

t(h)	7.95	8.80	11.72	28.58	40.35	41.68	63.83	81.45
class	C3.4	C1.1	C7.3	C4.5	C3.4	C2.4	C6.3	C6.0

Table 5.1: Row 1: the start time of flares occurring since = 0.00 = 00:00 UT on 3 July 2002 and for the whole observation period. Row 2: the class of flare (full disk emission from GOES X-ray database).

The sharp jump observed in the fractal dimension was $\Delta D_{12} = |D(t_2) - D(t_1)| = 0.19$. This value represents a significant 18% variation relative to the mean dimension $\langle D \rangle = 1.08$, and a nontrivial 9.5 factor in units of standard deviation $\sigma_D = 0.02$. Both the average and the standard deviation were computed over the whole observation time.

In order to test for reliability of the observed change of fractal dimension, we compare the relative change in D with the possible influence of seeing on the data, which could be responsible for the smoothing of the field. To evaluate the effect of image distortion on the slope of the sign-singularity spectrum, a simple technique to reproduce synthetic seeing variation has been

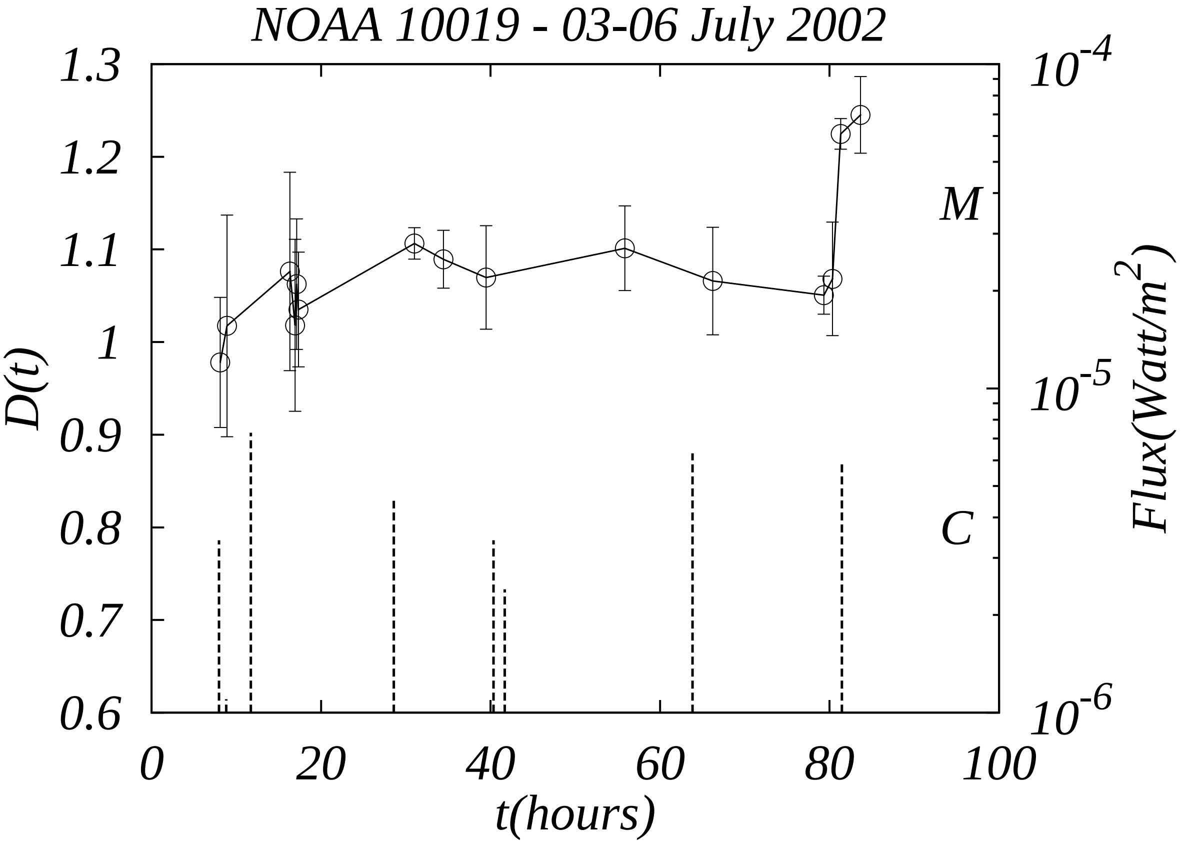

Figure 5.3: Fractal dimension of the photosperic current density structures *D versus* time. (symbols connected by solid line, left vertical axis). The vertical lines show the X-ray class of flares (right vertical axis).

used [46]. All components of each magnetic field vector within each magnetogram have been smoothed over $n \times n$ pixels areas, with $n = \{3, 5\}$, before computing the current density and performing the cancellation analysis. In the left panel of Figure 5.4 we show one example of the scaling behavior of the partition function $\chi(l)$ for the three samples, namely unsmoothed (1×1, circles), smoothed on 3×3 pixels area (diamonds) and smoothed on 5×5 pixels area (triangles). The example shown here refers to the snapshot taken at 17:20 UT on 3 July 2002. For the smoothed fields, the partition functions saturate at small scales at increasingly large scale, indicating that at these scales the measure becomes smooth, so that no sign singularity is present. This is the main effect of the smoothing [46]. Note that the partition function of the unsmoothed field does not saturate, probably because elementary flux tube are smaller than the instrumental resolution [44]. In the intermediatate region of scales, the cancellation exponent is found to slightly decrease with the smoothing. The right panel of Figure 5.4 resumes the dependence of cancellation exponent on image quality for the case presented in the left panel of the same figure. The relative variation of the scaling exponent in this case is less than 10%. Figure 5.5 shows the time dependence of dimensions D for the three series. While the general effect of the smoothing is the evident increase in fractal dimension, the main features of the time dependence, and in particular the sharp jump observed on the last day, are not

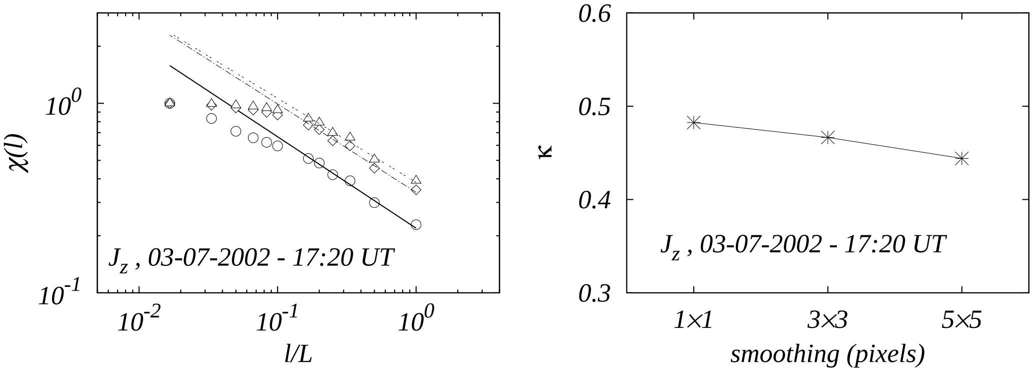

Figure 5.4: Left panel: the partition functions $log\ \chi(l)\ vs\ log\ (l/L)$ for the current density j_z calculated for unsmoothed (1×1, circles) and smoothed (3×3, diamonds, and 5×5, triangles). This example refers to the snapshot taken on 3 July 2002 at 17:20 UT. Right panel: cancellation exponents κ for the three cases shown in left panel.

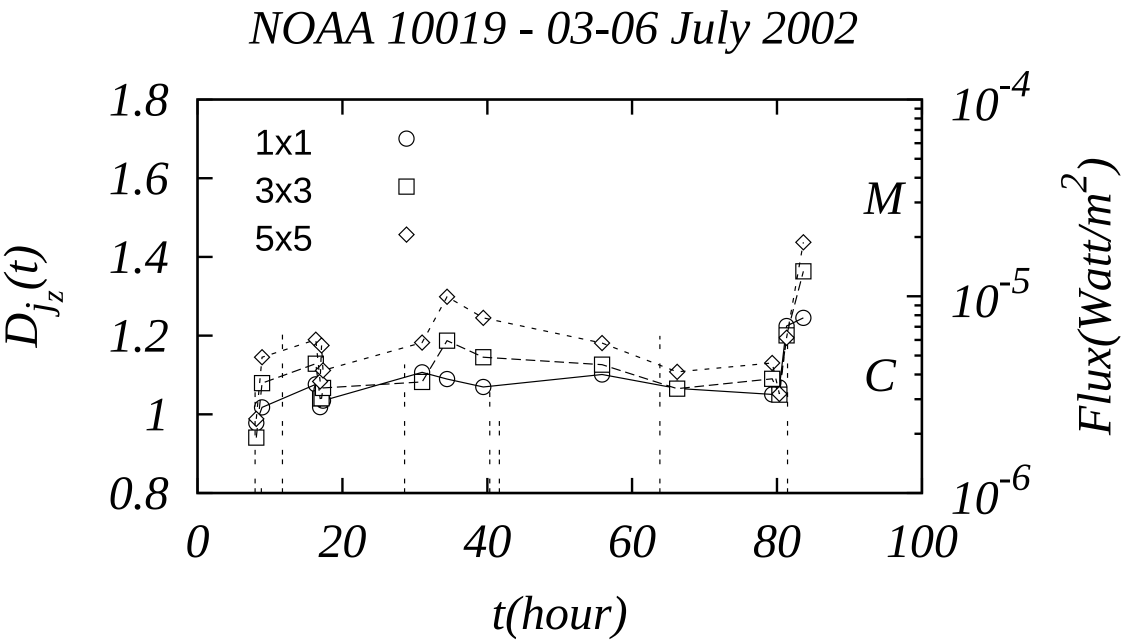

Figure 5.5: Fractal dimension *versus* time for the three datasets, obtained using the unsmoothed data (1×1) and the two synthetic datasets with smoothing (see legend). The vertical lines show the X-ray class of flares (right vertical axis).

lost, resulting in a 25% increase of D in both smoothed cases. Finally, the mean dimension increase ΔD_{Sn} due to the $n \times n$ smoothing was evaluated by averaging the differences $|D_{n\times n} - D_{1\times 1}|$ over the whole time window, obtaining $\Delta D_{S3} = 0.04$ and $\Delta D_{S5} = 0.09$. Therefore, the observed jump is significatively larger than the smoothing effect, $\Delta D_{12} > \Delta D_{Sn}$, confirming the goodness of the observation. Therefore, we can conclude that the observed change of fractal dimension observed in correspondence with the flare on 6 July 2002 is nontrivial, being sufficiently larger than the typical seeing smoothing.

Incidentally, it is worth noticing that a few similar flares have occurred during the time span of our observation. However, no clear observation of changes in the cancellation exponent was possible, as such flares were unfortunately not synchronized with regularly sampled magnetograms in the time series.

5.3 Space based solar observations: NOAA 11158

5.3.1 Observation

In contrast to the observations made from ground based telescopes, which are only possible during the daytime, and under favourable weather conditions, today modern space missions allow to conduct observations of the Sun with unprecedented spatial resolution, high temporal cadence and full time coverage. In this section, we will study the temporal evolution of the cancellation exponent obtained from high-resolution photospheric magnetograms of active region NOAA 11158. The evolution of AR 11158 is mainly characterized by two large bipoles emerging in close proximity, and by strong shearing motion between the central sunspot clusters [113] [114]. This very active AR produced one X-class, five M-class and fifty-six C-class flares in the time span from 2011 February 9 to 21.

The observations used here were performed by the *Helioseismic and Magnetic Imager* (HMI) instrument, that is part of the NASA space mission *Solar Dynamics Observatory* (SDO) ($http : //sdo.gsfc.nasa.gov$), which was launched on 11 February 2010 and is still actively colleting data. The instrument is designed to measure the Doppler shift, intensity and vector magnetic field at the solar photosphere using the 6173 $\mathring{A}$ Fe I absorption line of full solar disk, with the spatial resolution of $0.5''$/pixel, and with temporal cadence of 12 minutes. The instrument consists of a front-window filter, a telescope, a set of waveplates for polarimetry, an image-stabilization system, a blocking filter, a five-stage Lyot filter with one tunable element, two wide-field tunable Michelson interferometers, a pair of 4096^2 pixel cameras with independent shutters, and associated electronics. Each camera takes a full-disk image roughly every 3.75 seconds giving an overall cadence of 45 seconds for the Doppler, intensity, and line-of-sight magnetic field measurements, and a slower cadence for the full vector magnetic field. Details on the data reduction, and on the corrections performed on the database (180° ambiguity; absolute scale Doppler shift; disk center re-projection; Mercator Cartesian de-projection; flux distortion re-projection) can be found in Ref. [115].

The data analyzed here refer to the period of about seven day spanning from 2011 February 10 at 14:24 UT, to February 16 at 23:36 UT. This time interval covers the active region from its emergence through its flaring phase. Over the seven day period observed, the AR hosted six major flares as it passed the central meridian: an $X2.2$ flare, with a peak $GOES$ soft $X-ray$ flux on February 15 at 01:56 UT, leading to a pronounced halo CME, 3 M-class larger than of 1.2, $M6.6$ (13 Feb at 17:38 UT), $M2.2$ (14 Feb 17:26 UT), $M1.6$ (16 Feb 14:25 UT), 2 M-class smaller than of 1.2, $M1.0$ (16 Feb 01:32 UT), $M1.1$ (16 Feb 07:35 UT) and over 20 C-class flares.

Figure 5.6 shows a two-dimensional reconstructed image of one snapshot of the the currente helicity hc_z, calculated for the active region at the starting time of the $X2.2$ flare. The presence of positive and negative structures on all scales is cleary visible, indicating the pertinency of cancellation analysis for this dataset.

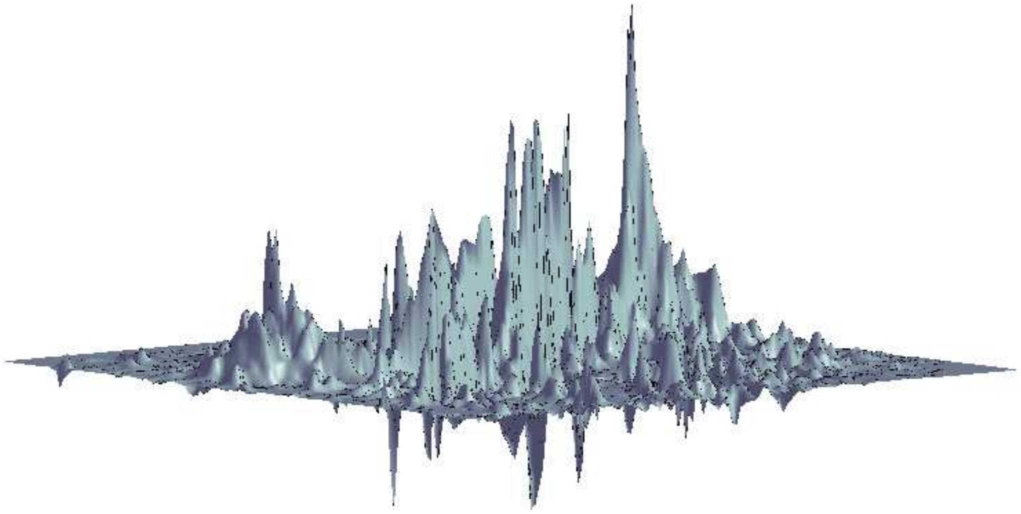

Figure 5.6: The current helicity hc_z determined for the active region NOAA 11158 on 2011-February-15 01:36 UT. The presence of positive and negative structures on all scales is cleary visible.

5.3.2 Data processing and cancellation analysis

The panels in Figure 5.7 show some examples of the maps of vertical magnetic fields B_z for three different times, in three different conditions. Panel *a* presents the active region NOAA 11158 in its emerging phase (2011 February 10 10:24 UT). In panel *b* the magnetic field is shown in the central phase of the AR lifetime, and in particular at the starting time of the largest $X2.2$ flare. In panel *c* the active region is shown at some time after the largest X2.2 flare: in this phase, the magetic structure have developed to a finer and more complex state. As done before for the THEMIS data, from the vector magnetic field, the vertical component of the current and the reduced current helicity were estimated as described in previous section.

In order to capture the main features of the magnetic field structures, for each magnetogram we select a reduced area $Q_{max}(L_{max}) = 150 \times 120$, corresponding to 75 *arcsec* in solar photosphere, centered in the position where the flare $X2.2$ and most of the flaring activity was located (Fig. 5.7 panel *b* small dotted-dashed box). In fact, the evident separatrix between the positive and negative polarity regions of the central part of the AR was solicited by most of the large flares occurred in NOAA 11158. This is therefore the region where most of the magnetic changes can be expected. Limiting the analysis to the subset $Q_{max}(L_{max})$ allows to reduce the effects of low magnetic field background on the partition function [46, 48, 49]. As already done for the ground based magnetograms described in previous section, the partition functions have been estimated for $N = 10$ positions of a slightly smaller box $Q(L) = 120 \times 120$ pixels, in order to fully span the entire area $Q_{max}(L_{max})$. From the average partition functions, the cancellation exponents κ were finally calculated through a power law fit [111, 112]. Panels of Figure 5.7 indicate, along with the area $Q_{max}(L_{max})$ (as dashed boxes), also the reduced boxes $Q(L)$ (as thin line boxes), corresponding to 60 *arcsec* in solar photosphere.

In left panels of Figures 5.8 and 5.9 we show the maps of vertical current density $j_z(x, y) = (\boldsymbol{\nabla} \times \boldsymbol{B}_\perp) \cdot \hat{e}_z$ and reduced current helicity $hc_z(x, y) = B_z(x, y) j_z(x, y)$, that, as we have already discussed, represents a measure of the non-potential magnetic energy available in the Active Region. In the right panels we show the corresponding averaged partition function for three different times, as in previous figure, namely corresponding to the emerging phase (panels *a*-*b*), to the maximum of flare activity (panels *c*-*d*), and to the later phase with enhanced complexity (panels *e*-*f*). When appropri-

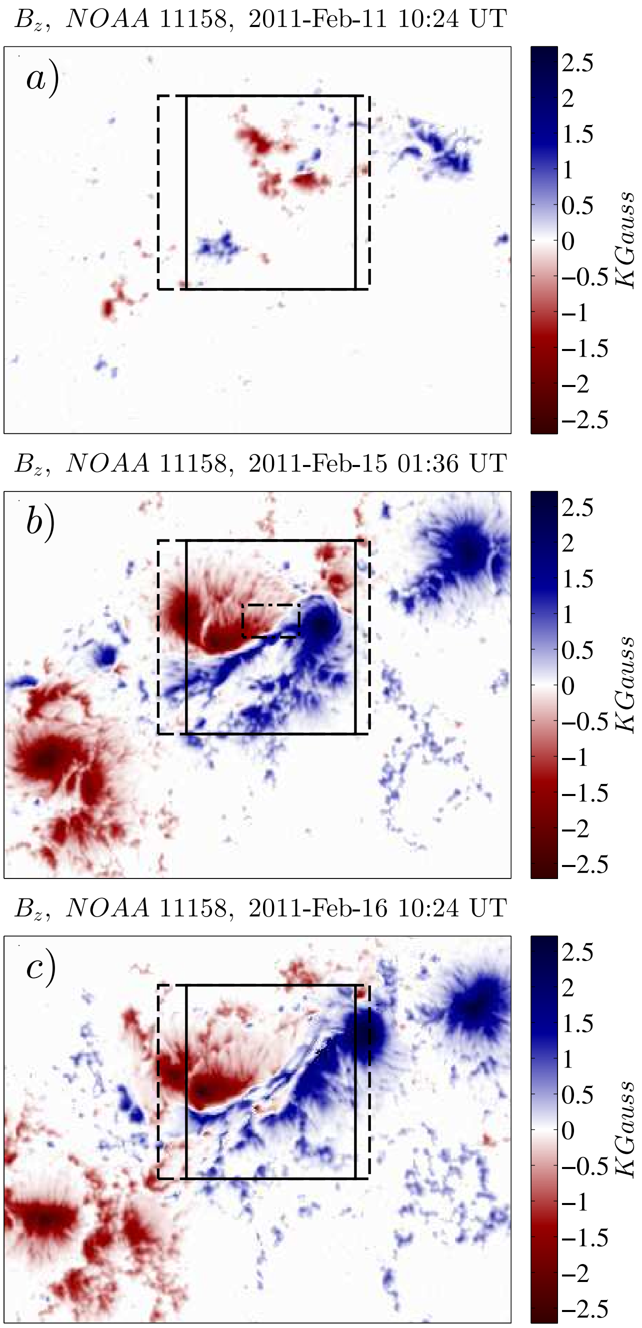
B_z, $NOAA$ 11158, 2011-Feb-11 10:24 UT

B_z, $NOAA$ 11158, 2011-Feb-15 01:36 UT

B_z, $NOAA$ 11158, 2011-Feb-16 10:24 UT

Figure 5.7: Maps of vertical magnetic fields B_z for 3 times (see the panels). Dashed-line boxes indicate the area $Q_{max}(L_{max}) = 150 \times 120$ pixels (corresponding a 75×60 *arcsec* on the solar photosphere) where, for $N = 10$ position of box $Q(L) = 120 \times 120$ (thin-line), the calculations were done. The choice of the area $Q_{max}(L_{max})$ was made according on the location of the flare X-class (small dotted-dashed boxes b). In the panel a the AR is in the phase of birth, while in panels $b - c$ the AR is more structured: panel b is taken at the start time of the flare $X2.2$, and c was taken while the AR was approaching the solar limb.

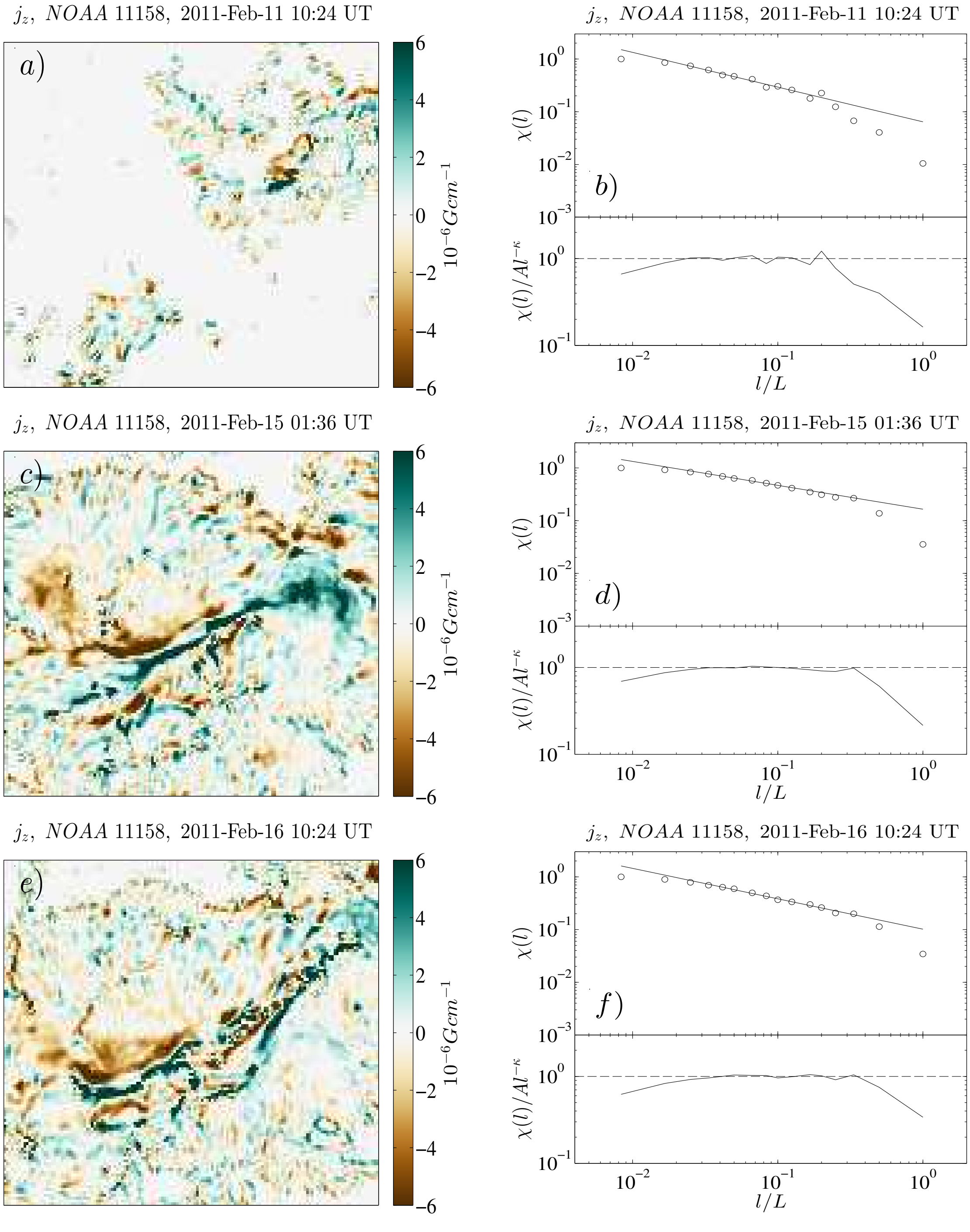
j_z, *NOAA* 11158, 2011-Feb-11 10:24 UT

j_z, *NOAA* 11158, 2011-Feb-15 01:36 UT

j_z, *NOAA* 11158, 2011-Feb-16 10:24 UT

Figure 5.8: Left panels show the maps of vertical current density j_z for the AR 11158 for 3 times (see the panels). Right top panels show the averaged partition function and the power law fits $\chi(l) = A(l/L)^{-\kappa}$ are superimposed. Finally, the bottom part of each right plot shows the compensated partition function $\chi(l)/A(l/L)^{-\kappa}$.

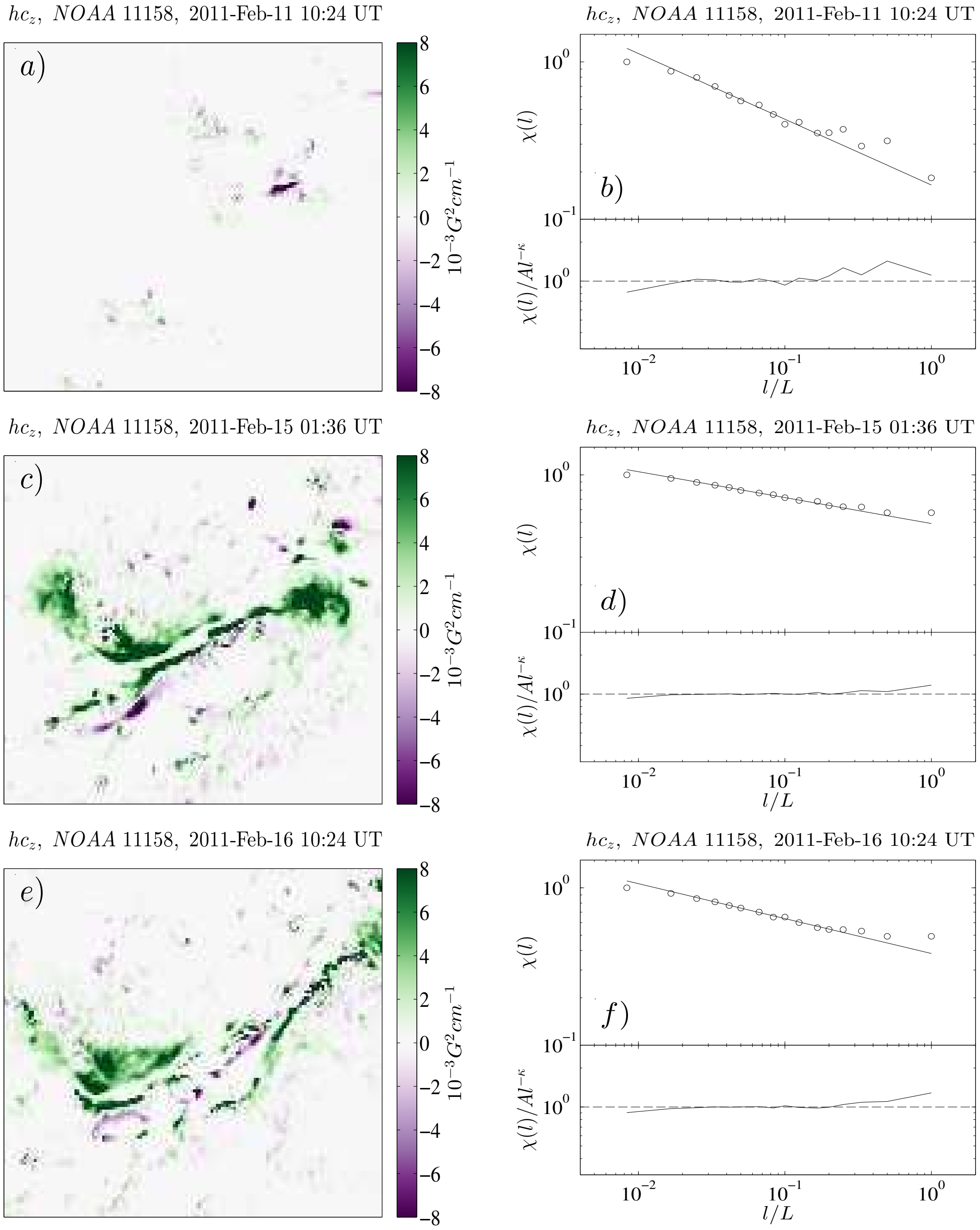

Figure 5.9: Left panels show the maps of vertical current density hc_z for the AR 11158 for 3 times (see the panels). Right top panels show the averaged partition function and the power law fits $\chi(l) = A(l/L)^{-\kappa}$ are superimposed. Finally, the bottom part of each plot right shows the compensated partition function $\chi(l)/A(l/L)^{-\kappa}$.

ate, power law fits $\chi(l) \sim l^{-\kappa}$ have been performed through a least square method. The fitting curves are superposed to the partition functions, showing the extremely good quality of the scaling, which extends to almost two decades. This power law range extension is outstandingly better than all other datasets studied in this thesis, which confirms the good quality of SDO data. For a more convincing visual test, the partition functions have been compensated by dividing them by the fitted power law $l^{-\kappa}$, and represented in the bottom panels of each Figure. Scaling ranges are seen as flat regions in the compensated plots. It is important to emphasize that all the partition functions tend to a constant value ($\chi = 1$) at small scales, which means that the instrument provides good resolution of the small scales. This is similar to what is observed in the 2D MHD numerical simulations [44]. Thanks to the good spatial resolution and low noise level, partition functions show excellent scaling also for the current (which was not the case for the previous analysis of solar data). We can anticpate here that for the current density we found a stationary state typical cancellation exponent $\kappa \simeq 0.5$, indicating the presence of current filaments $D \simeq 1$; for the current helicity $\kappa \simeq 0.2$, indicating smoother structures than for the current density.

The good quality of cancellation analysis allows a detailed comparison of the magnetic complexity of the AR with its flaring activity. To this aim, we have chosen a viable indicator for the flaring activity. The best indicator for this purpose would be the X-ray flux, which accounts for emission from the hot plasma, heated by the dissipative processes occurring during flares. However, measurements of X-ray flux are mostly available for the whole solar disk, the available measurements lacking of spatial information. Since during the period considered here another active region was producing large flares, we decided to use instead the Extreme-UV emission, as recored by the fast SDO-AIA instrument, which measures emission in the $131\mathring{A}$ channel with high cadency of 12 minutes. This instrument provides also spatial resolution, so that it was possible to compute the total EUV emission from the relevant solar region, that is the area around AR 11158. Figure 5.10 shows the area where the EUV was computed. We therefore have built a time series of the EUV emission of AR 11158, that we have downsampled to the same resolution as the magnetograms, 12 minutes. Figure 5.11 shows, as blue dashed-line, the time evolution of the EUV emission during the study period. The first phase is characterized by low emission, and the EUV signal can be considered as the background signal for the AR. Then, between September 13 and 14, the AR starts flaring, and the flaring activity is present till the end of the

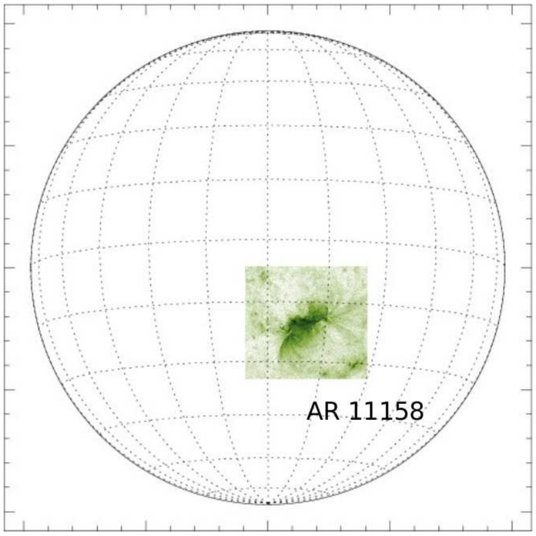

Figure 5.10: The Extreme-UV emission (SDO-AIA 131$\mathring{A}$ channel) integrated over AR 11158.

observation. Flares are clearly visible as peaks of the EUV signal. The main flares are labeled in the figure. It should be noticed that the AIA-SDO instrument is subject to saturation during the most intense events. This sets a limitation on the reliability of the actual values observed in the integration. For example, the flare of class $X2.2$ has a smaller peak than the previous M class flares. However, this problem only affects larger flares. Here we are mostly interested in the very occurrence of large flares, and their exact timing, their actual full intensity being irrelevant for our analysis.

Figure 5.11 also shows the temporal evolution of cancellation exponent (red line) for both the current (top panel) and the current helicity (bottom panel), as comparated to the EUV emission. In the initial phase, for $t \lesssim 13$, the cancellation exponent of the current density j_z shows large oscillations around $\kappa = 0.8$ ($D = 0.4$). For the current helicity hc_z, similar oscillations around to $\kappa = 0.5$ ($D = 1.0$) are observed, the structures being similar to filaments. This corresponds to the fact that the AR is still emerging, and the turbulent structures are in their forming phase. Incidentally, the oscillating, unstable behaviour of $\kappa(t)$ is analogous to the oscillations observed in Vlasov-Maxwell system, where oscillations where found to occur prior to the onset of fully developed turbulence (see Figures 4.11 and 4.12). Therefore, wide

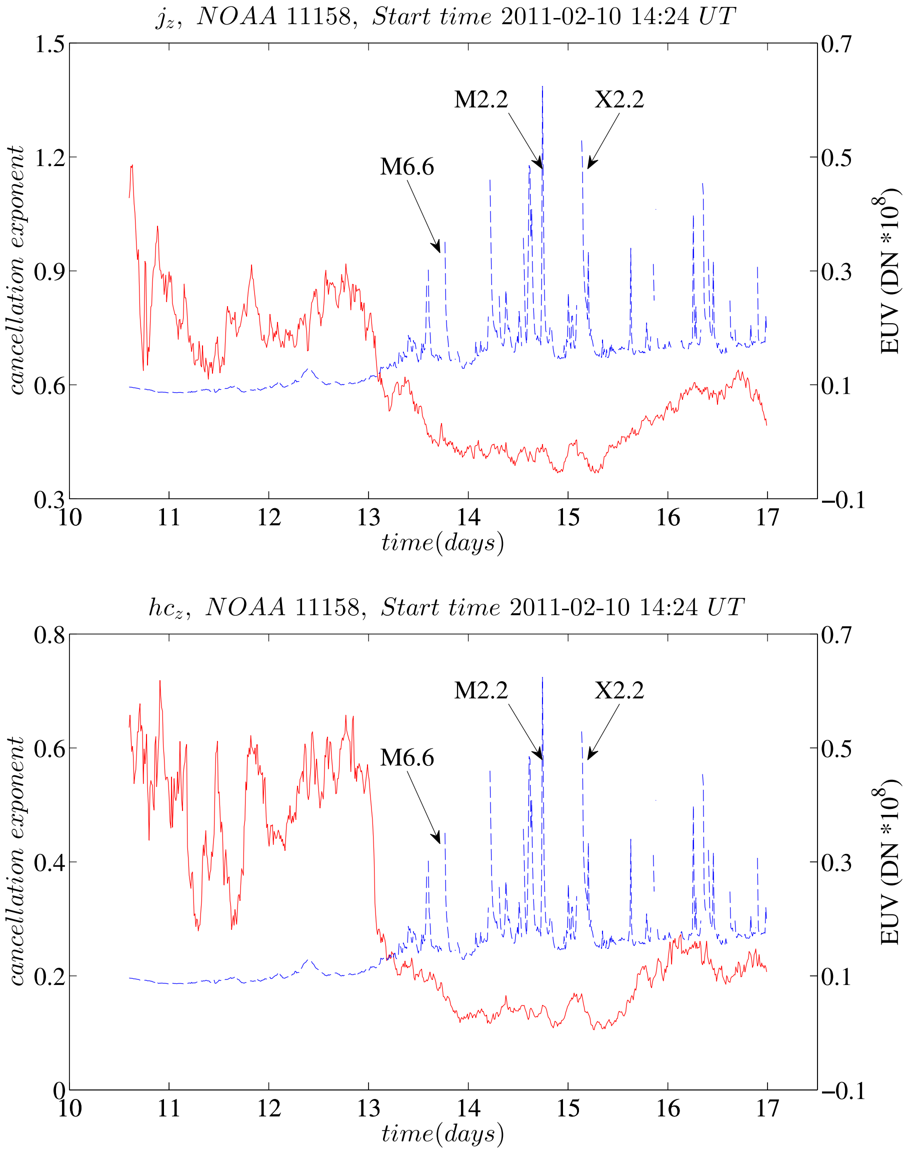

Figure 5.11: Top and bottom panels show the cancellation exponent for the current densisty and helicity respectively as a function of time exspressed in days (red line). The Extreme-UV emission (blue dashed-line) is superimposed.

oscillations of the cancellation exponents can reasonably be associated with emerging turbulence in the AR. This is also evident by looking at the time evolution of the magnetograms.

A confirmation is further provided by the observation of the magnetic flux emergence, depicted in Figure 5.12, and occurring at the same time (see the raising phase of the magnetic flux). Magnetic flux is estimated as integral of the magnetic field, over the whole AR, and separately for positive and negative polarity. In the second phase of the AR lifetime, when the field is settled and the AR is well stable ($13 \lesssim time \lesssim 16$), the cancellation exponent decreases abruptly. This is observed in correspondence with the main injection of magnetic flux, namely the full emersion of the AR, see Figure 5.12 [115]. The current cancellation exponent in this range is around $\kappa = 0.45$, indicating presence of current filaments, while for the current

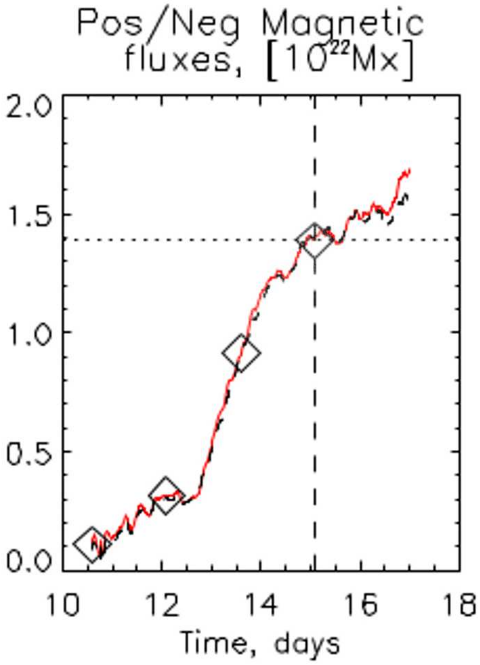

Figure 5.12: Magnetic fluxes computed for the whole active region. The red line is the positive magnetic flux and the black dashed line is the module of negative magnetic flux.

helicity $\kappa = 0.15$, in agreement with previous measurements of space based magnetograms [47].

During this period, there is the suggestion of some correspondence between the peaks of the EUV emission and those of the cancellation exponent, both for current density and helicity. In particular, for the $X2.2$ flare, this is clearly visibles for both fields, although a more defined peak is visible for the current helicity (compare Figure 5.11 top and bottom panels).

In this period of enhanced flaring state we found that the cancellation exponent starts increasing steadily about 4 to 12 hours before the solar flare peak, and reaches the maximum about 48 minuntes before the flare, before it decreases back to the starting value. This observation holds for both fields. Finally, in the last part of the observation, after late February 15, the average cancellation exponent increases again, showing the enhancement of the complexity of the AR. This behaviour seems to reflect the apperarence of thin filaments on the active region, whose origin is still unclear. We will not discuss last time span in this thesis, for which further studies will be needed.

In order to quantitatively evaluate the possible existence of correlation between the cancellation exponents κ and EUV emission, we have thus computed the *Spearman* and *Pearson* correlation coefficients, representing the measure of similarity between the two signals as a function of a shift or time shift applied to on of them. The main difference between the two coefficients is that Pearson correlation seeks only linear correlations, contrary to the Spearman correlation which also looks for non-linear correlations (which are likely to be present in this case, characterized by nonlinear dynamics), and is less sensitive to the presence of outliers. For this calculation, we have extracted the time series in the more stable, flaring period, from 13 February at 22:00 UT to 15 February at 12:00 UT, in order to exclude the uncorrelated emerging phase (no flares and large fluctuations of the cancellation exponent observed) and the increase of the cancellation exponent in the last part of the observation.

For each time lag, we have then evaluated the Pearson and Spearman correlation coefficients ρ_P and ρ_S, which are shown in Figure 5.13 versus the time lag (left panels). On right panels of the same figure, we show the scatter-plots of the cancellation exponents the current helicity, versus the Extreme-UV emission shifted by time-lags at which ρ has its maximum. For each scatter-plot, the maximum of the correlation coefficient ρ is indicated. The Pearson and Spearman correlations show a peaks of correlation for time-lags of 96 minutes and 84 minutes respectively, with coefficients $\rho_P = 0.49$,

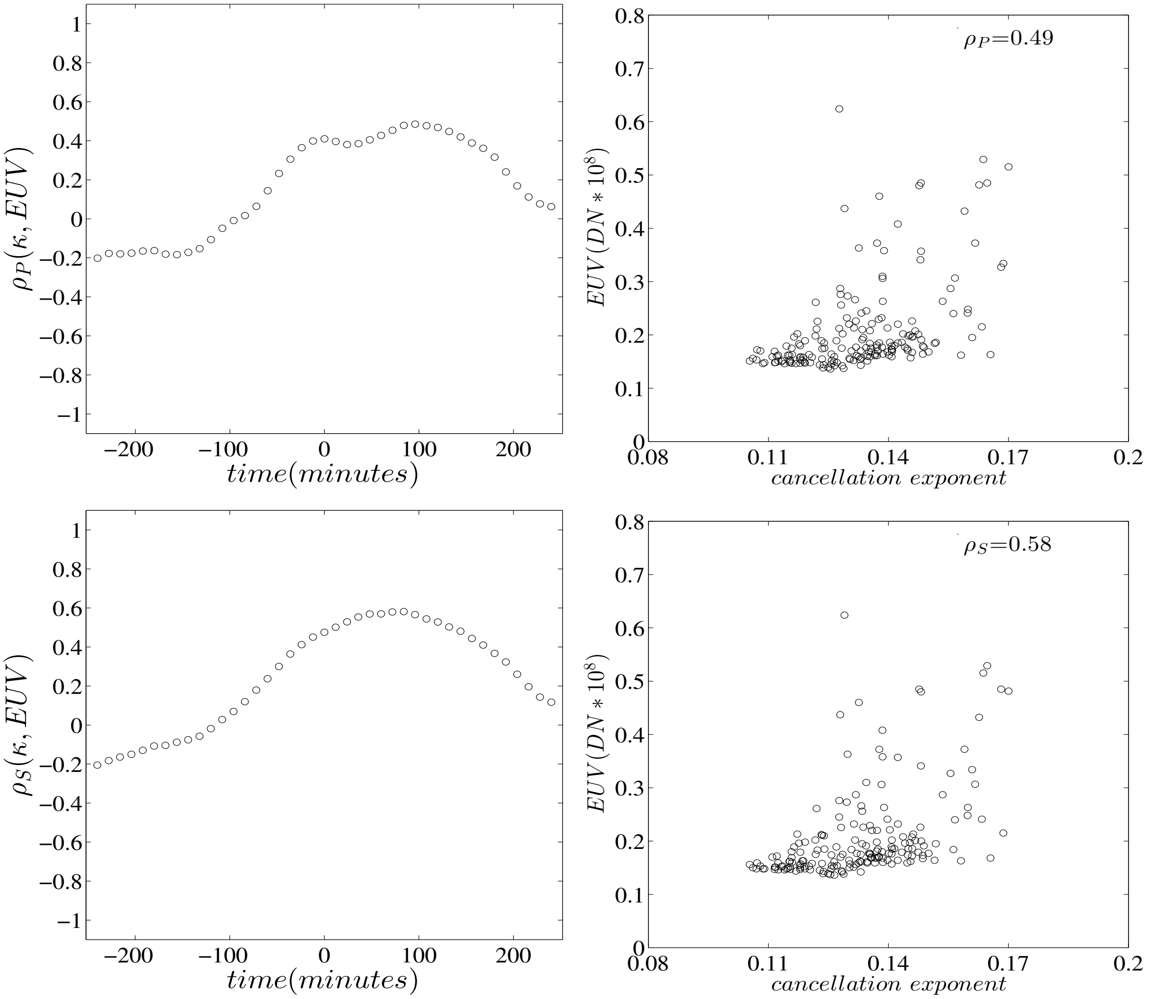

Figure 5.13: Left paneles: Correlation coefficients ρ_P and ρ_S *vs* time lags using *Pearson* (top) and *Spearman* (bottom) definitions. The right panels show the scatter-plot of cancellation exponents for hc_z shifted by the maximum correlation time-lags *vs* Extreme-UV emission. In each scatter plot, the correlation coefficient is indicated.

$\rho_S = 0.58$ indicating the presence of moderate, but significant correlation between the cancellation exponent and Extreme-UV emission. Similar result are obtained for the current density (not shown). Besides indicating the presence of nontrivial correlations, the scatter-plots suggest the presence of a threshold: only background EUV emission is observed for small $\kappa \lesssim 0.12$ (reduced field complexity), showing that higher complexity is needed for the AR to produce flares.

This analysis confirms the evidence of a modification of the structure of magnetic field, and in particular of the current density j_z and helicity hc_z, related with flare activity, and in particular that changes of the cancellation exponent κ are seen before the flares. The complexity of the magnetic field thus "anticipate" the eruption of a flare. This was not only confirmed by visual inspection of the time series, but its robusteness was also confirmed by statistical analysis of the correlation between the two fields.

5.3.3 Test on the quality of the analysis

In order to test the reliability of the results shown in previous subsection, we studied their stability with respect to different spatial and temporal data selection.

First, the whole analysis was repeated using different portions of the magnetograms, with the aim of checking the robustness of the results with respect to the choice of the spatial domain. Figure 5.14 top panel shows three different choices of the areas $Q_{max}(L_{max})$ where the signed measure was computed. Each area is centered on the location of the flare X2.2, is bounded by a box and labeled with letters. The area delimited by thin line, labeled A, encloses the entire active region (quadrupolar magnetic field) and a wide portion of background field. The area delimited by dashed line and labeled B includes only the quadrupolar structure. Finally, the area delimited by dot-dashed line, labeled C, is the area restricted to the flaring region, which we have already described in Section 5.3.2.

The bottom panel of figure 5.14 shows the three cancellation exponents κ_A (green dot-dashed line), κ_B (blue dashed line) and κ_C (red thin line) computed for the boxes labeled in top panel for the current helicity. The EUV radiation is also superimposed (grey line), and the 3 larger flares are indicated. It can be observed that the cancellation exponent becomes less sensitive to variations when increasing the box size where the signed measure is computed. $\kappa_A(t)$ and $\kappa_B(t)$ turn out to be more damped than the more

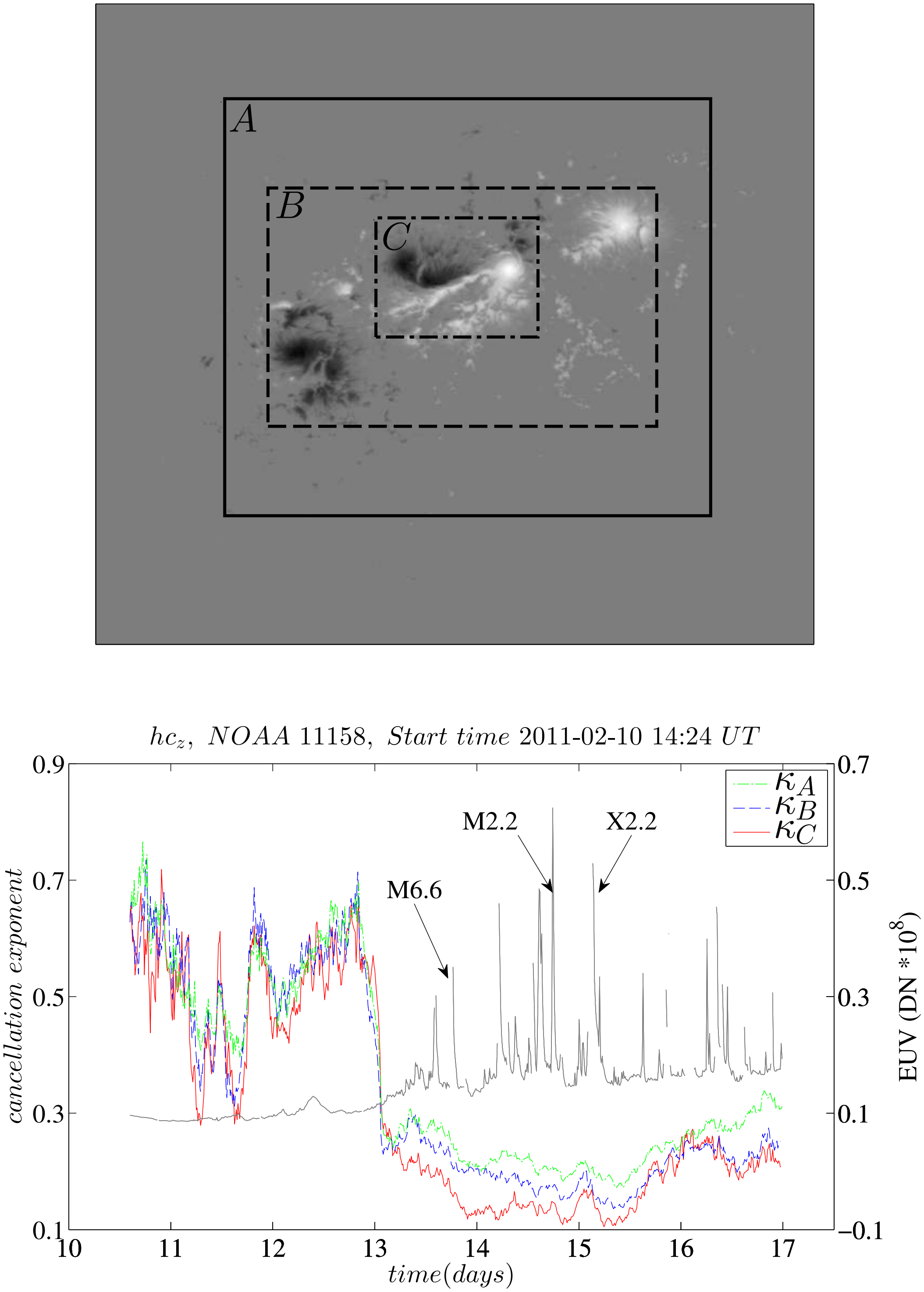

Figure 5.14: The top panel shows the Magnetic field B_z. The boxes labeled with A, B and C delimit the area where the signed measure is computed. The bottom panel shows the cancellation exponentd κ computed for the three boxes *vs* time. The extreme ultra-violet (EUV) radiation is superposed (grey line). The three larger flares are also indicated

detailed $\kappa_C(t)$. This is possibly due to the addition of the background magnetic field, and to the presence of the sign-definite polar regions at the right and left sides of the AR, which clearly contribute to reduce cancellations.

As already done for $\kappa_C(t)$ in section 5.3.2, we evaluate the possible of correlation of $\kappa_A(t)$ and $\kappa_B(t)$ with the EUV radiation, using the Spearman correlation, which we found more sensitive for the present case. Figures 5.15 shows the Spearman correlation computed for $\kappa_A(t)$ (left panel) and $\kappa_B(t)$(right panel). For $\kappa_A(t)$ we found a correlation coefficient $\rho_S = 0.51$ for time lag of 144 minutes, while for $\kappa_B(t)$ correlation coefficient is $\rho_S = 0.34$ for time lag of 192 minutes. The coefficient for $\kappa_A(t)$ is slightly smaller than the one obtained for the restricted area, but is still indicating significant correlations. $\kappa_B(t)$ correlation is weaker, probably because of the enhanced role of the two sign-defined structures at the sides of the AR. This test confirms that the results obtained in previous section are robust, and that despite the inclusion of portions of data with small magnetic field produces a modification of the cancellation properties, the main features related to flaring are stable.

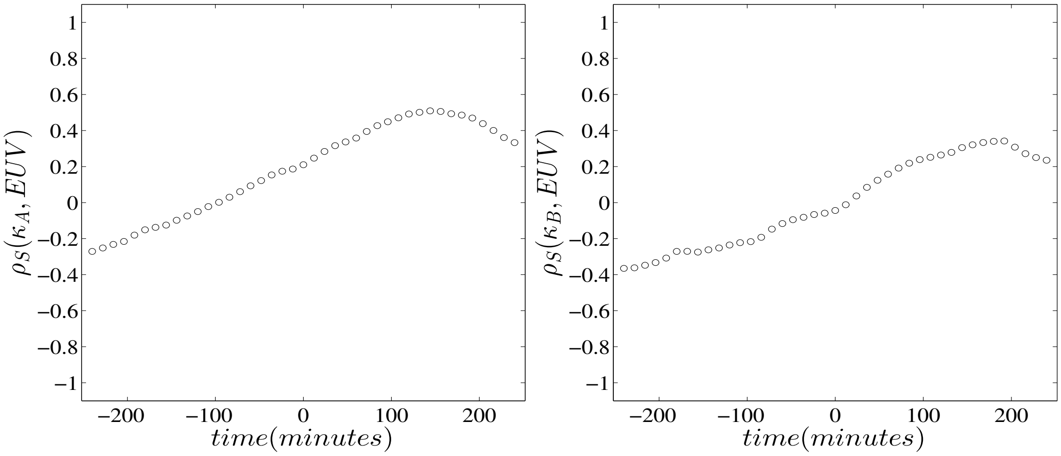

Figure 5.15: Correlation exponent (labeled ρ_S) *vs* time-lags using *Spearman* for the signal $\kappa_A(t)$ left panel and $\kappa_B(t)$ right panel and extreme ultra-violet (EUV) radiation. The cancelaltion exponents refer to for the current helicity.

Second, in order to test for the results robustness with respect to the time segment chosen for the analysis, we evaluate the correlations between $\kappa_C(t)$ and the EUV emission for a longer time interval, by including the final part of the observation. In figure 5.16 we show the Spearman correlation for the interval between $13 \leq time \leq 17$ (right panels), clearly indicating lower correlation ($\rho_S < 0.3$). This shows that the choice of temporal interval used for the analysis can be critical in order to evaluate correlations. In particular, the non-stationary, steady increase of the cancellation exponent in the last part of the time series is not associated with any similar increase in EUV emission. This evidences that cancellation exponent responds to flare emis-

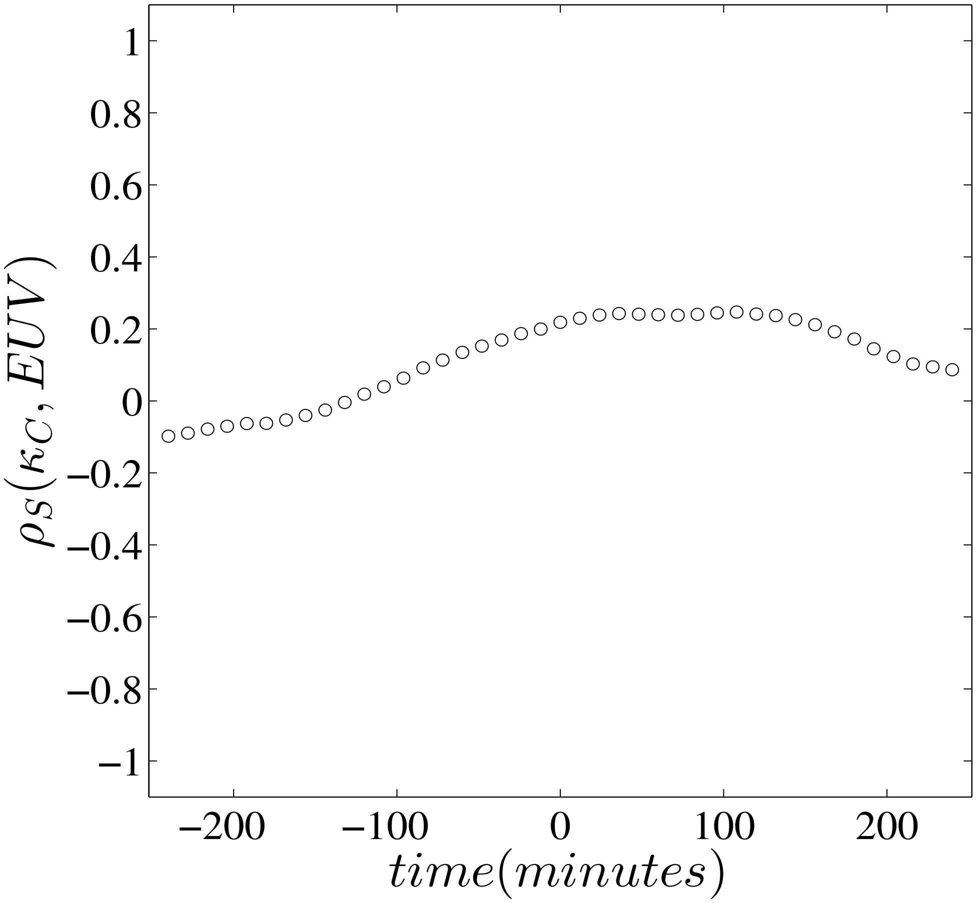

Figure 5.16: Spearman correlation between cancellation exponent $\kappa_C(t)$ and EUV emission (see Fig. 5.14) calculated for the whole temporal series shown in the left panel, and for interval between $13 \leq time \leq 17$, shown in the right panel.

sion through fluctuations rather to steady than absolute value modifications. For these reasons, we believe that our choice of time interval for performing for the analysis shown here was appropriate.

Finally, in order to compare the cancellation exponent with other magnetic signatures, we have calculated the Spearman correlation between the EUV emission and the positive and negative magnetic fluxes, as estimated for the vertical component of magnetic field B_z, as well as between the magnetic fluxes and cancellation exponent. Figure 5.17 shows the correlation function for both fluxes and the EUV emission. The smaller correlation coefficient obtained in this case ($\rho_S < 0.4$) confirms that the cancellation exponent of the current helicity is a better observable to highlight correaltions with flaring activity. Similar results were obtained for the correlation between both magnetic fluxes and cancellation exponent ($\rho_S < 0.3$ for both fluxes, not shown). This observation confirms that the spatial features of the magnetic field, as described through the current and current helicity, are necessary ingredient for the correct evaluation of the magnetic complexity of ARs, and their relationship with flares.

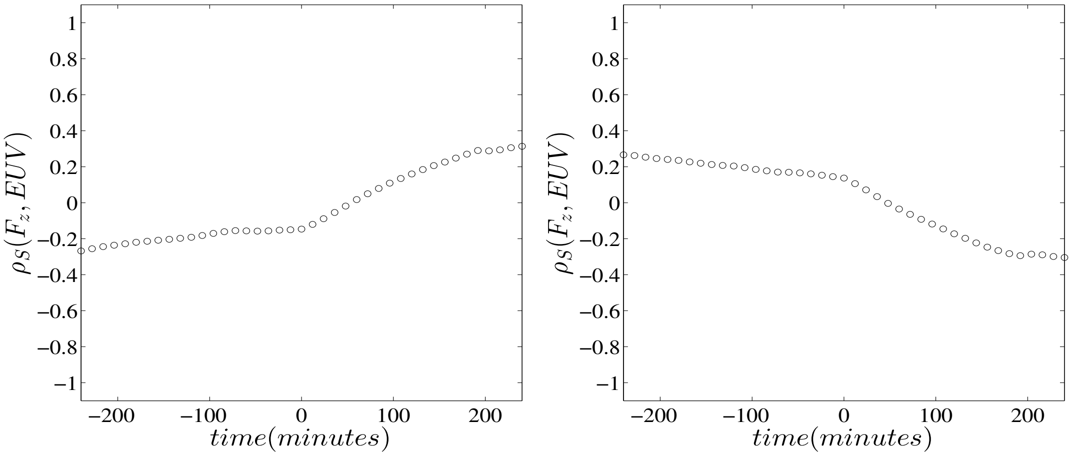

Figure 5.17: Spearman correlation of positive and negative magnetic flux and extreme ultra-violet, left and right panel respectively.

5.4 Conclusions

Cancellations analysis has been used to describe the topological properties of the typical current structures in solar photospheric active regions, and their temporal evolution in response to photospheric magnetic field dynamics, in two active regions, NOAA 10019 and NOAA 11158. The time evolution has been evaluated as the variation of the scaling index describing the cancellations of positive and negative current density, computed for the active region NOAA 10019, and for current density and current helicity for the NOAA 11158. Cancellation exponents provide the typical fractal dimension of the structures. The values found in this analysis can be associated with filaments $D \simeq 1$ for the current density, while smoother structures were found for the current helicity.

For NOAA 10019, comparison with flare related X-ray emission has revealed that in one instance the current structures changed their topological dimension abruptly in proximity of a C-class flare (see fig. 5.3). The dimension of the current structures increased by roughly 25% about one hour before the flare, showing that magnetic structures modifications anticipate the explosive events. This result is in agreement with previous observations.

The use of ground-based data shows that the cancellation analysis is a good technique, because sensitive to variations of the structures. However, the low temporal resolution of the magnetograms does not allow a more detailed understanding of the process. In order to get a better insight on topological changes of magnetic structures and their relationship with flare eruption, better quality data (high-resolution, possibly continuous, longer term observation of the magnetic vector prior to and after a flare) are necessary.

To this aim, the dynamical evolution of the photospheric magnetic fields complexity has been studied using high spatial and temporal resolution data for the AR 11158. We have shown that current density and current helicity own sign-singular scaling properties, indicating the presence of coherent structures (such as current filaments). The fractal dimension of the typical structures has been estimated. Furthermore, our observations confirms that magnetic fields change their topology one or two hours before large flares, and this can be revealed by the changes in the cancellation exponent, which thus represent a precursor. Finally, our analysis supports the presence of correlations between the cancellation exponent and the EUV emission of the AR. Also, it suggests that low complexity fields do not produce significant flares, which need high complexity.

It is worth noting that ground and space based data have different (opposite) behaviour, possibly due to the low space and time resolution of ground based measurements. This discrepancy deserves further attention and will be studied in future works.

Bibliography

[1] V. M. Canuto and J. Christensen-Dalsgaard, Annual Review of Fluid Mechanics, Vol. 30: 167-198.

[2] Brandenburg A. and Nordlund Å., Rep. Prog. Phys. **74** 046901 (2011)

[3] A. A. Schekochihin and S. C. Cowley, *Turbulence and magnetic fields in astrophysical plasmas*, in: Magnetohydrodynamics: Historical Evolution and Trends, S. Molokov, R. Moreau, and H. K. Moffatt, Eds. (Berlin: Springer, 2007), 85 [e-print astro-ph/0507686])

[4] Stix. M, *The Sun*, Springer; 2nd edition (2004).

[5] V. Carbone and R. Bruno, Astrophys. J. **488**, 482 (1997)

[6] Carmichael, H.: 1964, In: Hess, W.N. (ed.) AAS-NASA Symposium on the Physics of Solar Flares, NASA, Washington, 451.

[7] Sturrock, P.A.: 1968, In: IAU Symp. 35: Structure and Development of Solar Active Regions, 471

[8] Hirayama, T.: Solar Phys. 34, 323 (1974).

[9] Kopp, R.A., Pneuman, G.W.: 1976, Solar Phys. 50, 85.

[10] D. Longcope, C. Beveridge, J. Qiu, B. Ravindra, G. Barnes and S Dasso. Solar Phys 244: 4573 (2007)

[11] G. Consolini, V. Carbone, F. Berrilli et al., Astron. Astrophys. **344**, L33 (1999)

[12] Akhiezer, A. I., Akhiezer, A., Polovin, R. V., Sitenko, A. G., and Stepanov, K. N., 1975, *Plasma electrodynamics, Vol. 2 Linear Theory*, Pergamon, New York, (1975).

[13] E. Marsch et al., J. Geophys. Res. **87**, 52 (1982)

[14] E. Marsch, X. Z. Ao, and C.-Y. Tu, J.Geophys. Res. **109**, A04102 (2004).

[15] S. P. Gary, Theory of Space Plasma Microinstabilities (Cambridge University Press, Cambridge, 1993);

[16] P.Hellinger et al., Geophys. Res. Lett. **33**, L09101 (2006).

[17] V. Holloweg and P. A. Isenberg, J. Geophys. Res. **107**, 1147 (2002).

[18] A.P. Matthews, J. Comput. Phys. **112** 102116 (1994).

[19] Elsässer, W. M., The hydromagnetic equations, Phys. Rev., 79, 183, (1950).

[20] E. Siggia, J. Fluid Mech, **107** 375 (1981).

[21] W. T. Ashurts, A. R. Kerstein, R. M. Kerr and C. H. Gibson, Phys. Fluids, **30** 375 (1981).

[22] A. Vincent and M. Meneguzzi, J. Fluid Mech., **225**, 1 (1991).

[23] Z. S. She, E. Jackson, and S. A. Orszag, Nature, **344**, 226 (1990).

[24] D. Porter, A. Pouquet and P. Woodward, Phys. Rev. Lett., **68**, 3156 (1992).

[25] D. Biskamp and H. Welter, Phys. Fluids B, **1**, 1964 (1989).

[26] H. Politano, A. Pouquet and P. L. Sulem, Phys. Fluids B, **1**, 2330 (1989).

[27] D. Biskamp and W. C. Müller, Phys. Plasmas, **7**, 4889 (2000).

[28] A. Brandenburg, I. Procaccia and D. Segel, Phys. Plasmas, **2**, 1148 (1995).

[29] H. Politano, A. Pouquet and P. L. Sulem, Phys. Plasmas, **2**, 2931 (1995).

[30] E. Ott, Y. Du, K. R. Sreenivasan, A. Juneja and A. K. Suri, Phys. Rev. Lett., **69**, 2654 (1992).

[31] U. Frisch, *Turbulence: The legacy of A.N. Kolmogorov*, Cambridge Univ. Press, Cambridge, UK (1995).

[32] A. Brandenburg, I. Procaccia and D. Segel, Phys. Plasmas **2**, 1148 (1995).

[33] H. Politano, A. Pouquet and P. L. Sulem, Phys. Plasmas **2** (8), 2931 (1995).

[34] R. M. Kerr and A. Brandenburg, Phys. Rev. Lett. **83** 1155 (1999).

[35] D. Biskamp and H. Welter, Phys. Fluids B **1**, 1964 (1989).

[36] H. Karimabadi, V. Roytershteyn, M. Wan, W. H. Matthaeus, W. Daughton, P. Wu, M. Shay, B. Loring, J. Borovsky, E. Leonardis, S. C. Chapman and T. K. M. Nakamura. Phys. Plasmas, **20**, 012303 (2013)., Phys. Plasmas **20**, 012303 (2013)

[37] S. Donato, S. Servidio, P. Dmitruk, V. Carbone, M. A. Shay, and P. A. Cassak, Phys. Plasmas, **19**, 092307 (2012).

[38] P. Veltri, Plasma Phys. Cont. Fus. **41**, A787-A79 (1999).

[39] C. Salem, A. Mangeney, S.D. Bale, P. Veltri, Astrophys. J. **702**, 537-553 (2009).

[40] A. Greco, P. Chuychai, W. H. Matthaeus, S. Servidio, P. Dmitruk, Geophys. Res. Lett. **35**, L19111 (2008).

[41] D. Sundkvist, A. Retinò, A. Vaivads, S. D. Bale, Phis. Rev. Lett. **99**, 025004 (2007).

[42] S. I. Vainshtein, Y. Du, and K. R. Sreenivasan, Phys. Rev. E **49**, R2521 (2007).

[43] A. L. Bertozzi and A. B. Chhabra, Phys. Rev. E **49**, 4716 (1994).

[44] L. Sorriso-Valvo, V. Carbone, A. Noullez and H. Politano, A. Pouquet, P. Veltri, Phys. Plasmas, **9**, 89-95 (2002).

[45] Graham, J., P. D. Mininni, and A. Pouquet, Phys. Rev. E **72**, 045301(R) (2005).

[46] V. B. Yurchyshyn, V. I. Abramenko, and V. Carbone, Astrophys. J., **538**, 968 (2000).

[47] V. Yurchyshyn, V. Abramenko, and H. Watanabe, Hinode-3: The 3rd Hinode Science Meeting ASP Conference Series, Vol. 454, T. Sekii, T. Watanabe, and T. Sakurai eds, 2012 Astronomical Society of the Pacific.

[48] V. I. Abramenko, V. B. Yurchyshyn, and V. Carbone, Solar Phys. **178**, 35, (1998).

[49] L. Sorriso-Valvo, V. Carbone, P. Veltri, V. I. Abramenko, A. Noullez, H. Politano, A. Pouquet, V. B. Yurchyshyn, Planet. Space Sci. **52**, 937 943 (2004).

[50] P. D. Mininni, D. O. Gómez, and S. M. Mahajan, Astrophys. **J. 584**, 1120 (2003).

[51] F. Mozer, S. Bale, and T. D. Phan, Phys. Rev. Lett. **89**, 015002 (2002).

[52] D. Smith, S. Ghosh, P. Dmitruk, and W. H. Matthaeus, Geophys. Res. Lett. **31**, 02805, DOI: 10.1029/2003GL018689 (2004).

[53] L. F. Morales, S. Dasso, and D. O. Gómez, J. Geophys. Res. **110**, A04204, DOI: 10.1029/2004JA010675 (2005).

[54] M. Wardle, Mon. Not. R. Astron. Soc. **303**, 239 (1999).

[55] S. A. Balbus and C. Terquem, Astrophys. **J. 552**, 235 (2001).

[56] W. H. Matthaeus, P. Dmitruk, D. Smith, S. Ghosh, and S. Oungthon, Geophys. Res. Lett. **30**, 2104, DOI: 10.29/2003GL017949 (2003).

[57] P. D. Mininni, D. O. Gómez, and S. M. Mahajan, Astrophys. **J. 619**, 1019 (2005).

[58] S. Galtier, J. Plasma Phys. **72**, 721 (2006).

[59] P. Dmitruk and W. H. Matthaeus, Phys. Plasmas **13**, 2307 (2006).

[60] D. O. Gomez, S. M. Mahajan, and P. Dmitruk, Phys. Plasma **15**, 102303 (2008).

[61] L. N. Martin, P. Dmitruk, Phys. Plasma **17**, 112304 (2010).

[62] N. H. Bian and D. Tsiklauri, Phys. Plasma **16**, 064503 (2009).

[63] G. P. Zank and W. H. Matthaeus, J. Plasma Phys. **48**, 85 (1992).

[64] A. A. van Ballegooijen, Astrophys. J. **311**, 1001 (1986).

[65] D. W. Longcope, and R. N. Sudan, Astrophys. J. **437**, 491 (1994).

[66] D. L. Hendrix and G. van Hoven, Astrophys. J. **467**, 887 (1996).

[67] L. Milano, P. Dmitruk, C. H. Mandrini, D. O. Gómez, and P. Demoulin, Astrophys. J. **521**, 889 (1999).

[68] D. O. Gómez, and C. Ferro Fontán, Astrophys. J. **394**, 662 (1992).

[69] P. Dmitruk and D. O. Gómez, Astrophys. J. Lett. **527**, L63 (1999).

[70] G. Nigro, F. Malara, V. Carbone, P. Veltri, Phys. Rev. Lett **92**, 194501 (2004).

[71] G. Nigro, F. Malara, P. Veltri, Astrophys. J. **685**, 606 (2008).

[72] P. Dmitruk, D. O. Gómez, and W. H. Matthaeus, Phys. Plasmas **10**, 3584 (2003).

[73] S. Oughton, P. Dmitruk, and W. H. Matthaeus, Phys. Plasmas **11**, 2214 (2004).

[74] P. Dmitruk, W. H. Matthaeus, and S. Oughton, Phys. Plasmas **12**, 112304 (2005).

[75] P. Dmitruk and W. H. Matthaeus, Phys. Plasmas **13**, 042307 (2006).

[76] J. Birn and M. Hesse, J. Geophys. Res. **106**, 3737 (2001).

[77] Y. Ren, M. Yamada, S. Gerhardt, H. Ji, R. Kulsrud, and A. Kuritsyn, Phys. Rev. Lett. **95**, 55003 (2005).

[78] M. Shay, J. F. Drake, B. N. Rogers, and R. E. Denton, J. Geophys. Res. **106**, 3759 (2001).

[79] L. N. Martin, P. Dmitruk, and D. O. Gómez, Phys. Plasmas, **19**, 052305 (2012).

[80] P. D. Mininni, D. O. Gómez, and S. M. Mahajan, Astrophys. J. **567**, L81 (2002).

[81] P. D. Mininni, D. O. Gómez, and S. M. Mahajan, Astrophys. J. **584**, 1120 (2003).

[82] P. D. Mininni, D. O. Gómez, and S. M. Mahajan, Astrophys. J. **619**, 1019 (2005).

[83] P. D. Mininni, A. Alexakis and A. Pouquet, J. Plasma Phys. **73**, 377 (2007).

[84] D. O. Gómez, P. D. Mininni, and P. Dmitruk, Phys. Rev. E **82**, 036406 (2010).

[85] M. Yamada, Y. Ren, H. Ji, J. Breslau, S. Gerhardt, R. Kulsrud, and A. Kuritsyn, Phys. Plasmas, **13**, 052119 (2006).

[86] O. Alexandrova, V. Carbone, P. Veltri, and L. Sorriso-Valvo, Pl. and Space Sc. **55**, 2224 (2007).

[87] O. Alexandrova, V. Carbone, P. Veltri, and L. Sorriso-Valvo, Astrophys. J. **674**, 1153 (2008).

[88] K. H. Kiyani, S. C. Chapman, Yu. V. Khotyaintsev, and M. W. Dunlop and F. Sahraoui, Phys. Rev. Lett. **103**, 075006 (2010).

[89] P. Rodriguez Imazio, L. N. Martin, and P. D. Mininni, Phys. Plasma, “is tentatively scheduled for publication in the June, 2013

[90] M. Wan, S. Oughton, S. Servidio and W.H. Matthaeus, Phys. Plasmas **17**, 082308 (2010).

[91] H. R. Strauss, Phys. Fluids, **19**, 134 (1976).

[92] D. Montgomery, Phys. Scripta, **T2**, 83 (1982).

[93] D. O. Gómez, S. M. Mahajan, and P. Dmitruk, Phys. Plasmas, **15**, 102303 (2008).

[94] L. N. Martin, P. Dmitruk, and D. O. Gomez, Phys. Plasma **17**, 112304 (2010).

[95] S. Ghosh, M. Hossain, and W. H. Matthaeus, Phys. Commun. **74**, 18 (1993).

[96] S. Servidio, F. Valentini, F. Callifano, and P. Veltri, Phys. Rev. Lett **108**, 045001 (2012).

[97] D. Perrone0, F. Valentini, S. Servidio, S. Dalena , and P. Veltri, Astrophys. J. 62:99 (9pp), (2013).

[98] P. D. Mininni and A. Pouquet, Phys. Rev. E. **80**, 025401 (2009).

[99] R. Bruno and V. Carbone Living Rev. Solar Phys. **2**, 4 (2005).

[100] F. Valentini, P. Trávníček, F. Califano, P. Hellinger, A. Mangeney, J. Comput. Phys. **225**, 753 (2007); F. Valentini, F. Califano, and P. Veltri, Phys. Rev. Lett. **104**, 205002 (2010).

[101] S. D. Bale, P. J. Kellogg, F. S. Mozer, T. S. Horbury, and H. Reme, Phys. Rev. Lett. **94**, 215002 (2005); S. Servidio, V. Carbone, L. Primavera, P. Veltri, K. Stasiewicz, Planet. Space Sci. **55**, 2239 (2007).

[102] Manoharam, P., et al., ApJ 1180, 559 (2001)

[103] Dryer, M., et al., Solar Physics, 265, 204 (2001)

[104] C. Zwaan, Solar Physics, vol. 100, Oct. 1985, p. 397-414

[105] A. O. Benz, Living Rev. Solar Phys., **5**, 1 (2008)

[106] E. N. Parker. *Stimulated dissipation of magnetic discontinuities and the origin of solar flares*, Solar Phys. **111**, 297 (1987).

[107] E. Priest Solar Magnetohydrodynamic. D. Reidel Publishing Company, Dordrecht, (1982).

[108] M. J. Hagyard, B. A. Stark, P. Venkatakrishnan A Search for vecto magnetic field variations associated with M-class flares of 10 June 1991 in Ar 6659. Sol. Phys. **184**, 133 (1999).

[109] C. Briand and A. Vecchi, Astronomy & Astrophysics L33L36 (2003).

[110] A. Skumanich, B. W. Lites, V. Marti nez Pillet, & P. Seagraves, ApJS, 110, 357 (1997)

[111] J. K., Lawrence, A. A. Ruzmaikin and A. C. Cadavid. Astrophys. J. **472**, 805 (1993)

[112] V. I. Abramenko, V. B. Yurchyshyn, and V. Carbone, Astrophys. J. **538**, 968, (2000).

[113] C.J. Schrijver, G. Aulanier, A. M., Title, E. Pariat, & C. Delannée, ApJ, **736**, 102, (2011)

[114] X. Sun, J. Hoeksema, Y. Liu, et al., ApJ, **748**, 77, 2012

[115] Kazachenko, M.; Fisher G.H.; Welsch B.T.; Electric Fields, Poynting Fluxes and Helicity Fluxes in AR 11158, in prep.